# High Pressure X-ray and Raman Studies of the Selected Metal Hydrides

Thesis by

**Haijing Meng**

prepared under the supervision of

**prof. dr hab. Marek Tkacz**


within the framework of International PhD Studies at the
Institute of Physical Chemistry of the Polish Academy of Sciences
**High pressure laboratory**

Kasprzaka 44/52, 01-224 Warsaw



Warsaw, March 2019

# Acknowledgements

First and foremost, I would like to express my very great appreciation to the following people who play extremely essential roles during my doctoral study:

**Prof. Marek Tkacz,** who has provided the patient guidance throughout my PhD study and enlightened me with his rich scientific experience and deep wisdom;

**Dr Mikhail A. Kuzovnikov,** who helped me a lot in the experimental techniques and contributed his constructive discussion in the research.

**My parents and husband,** who gave numerous support physically and emotionally, making me who I am today;

**My son,** who filled my life with full of happiness and encouraged me a better version of myself;

Besides, I gracefully acknowledge my thesis committee, **Prof. Robert Nowakowski, Prof. Andrej Poniewierski, Prof. Janusz Jurczak, Prof. Jacek Waluk, Prof. Henryk Drulis and Prof. Henryk Figiel,** for generously offering their time and guidance through the whole process.

Heartfelt thanks go the other colleagues from the **High Pressure Laboratory** for your sincere support and great help. Specifically, I would like to express my sincere thanks to **Dr Taras Palasyuk** for his technical guidance at the beginning of my study.

Last but not least, I am profoundly grateful to thank all the colleagues from the Institute of Physical Chemistry Polish Academy of Sciences for making my life in Poland joyful.

# List of publications

## Publications directly related to the Thesis

1. H. Meng, M.A. Kuzovnikova, M. Tkacz, *Phase stability of some rare earth trihydrides under high pressure.* International Journal of Hydrogen Energy, 42 (2017): 29344-29349.

2. H. Meng, T. Palasyuk, V. Drozd, M. Tkacz, *Study of phase stability and isotope effect in dysprosium trihydride at high pressure*. Journal of Alloys and Compounds, 722(2017): 946-952.

3. M. A. Kuzovnikov, M. Tkacz, H. Meng, D. I. Kapustin, V. I. Kulakov, *High-pressure synthesis of tantalum dihydride.* Physical Review B, 96 (2017): 134120

4. M. A. Kuzovnikov, H. Meng, M. Tkacz, *Nonstoichiometric molybdenum hydride.* Journal of Alloys and Compounds. 694 (2017): 51-54.

## Other publications

5. Y. Fang, F. Du, Y. Xu, H. Meng, J. Huang, J. Yu, et al, *Enhanced cellular uptake and intracellular drug controlled release of VESylated gemcitabine prodrug nanocapsules.* Colloids and Surfaces B: Biointerfaces, 128 (2015): 357-362.

6. Y. Xu[1], H. Meng[1], F. Du, W. Lu, J. Yu, et al, *Preparation of intravenous injection nanoformulation of VESylated gemcitabine by co-assembly with TPGS and its anti-tumor activity in pancreatic tumor-bearing mice.* International journal of pharmaceutics, 495.2 (2015): 792-797.

7. F. Du, H. Meng, K. Xu, Y. Xu, P. Luo, J. Yu, et al, *CPT loaded nanoparticles based on beta-cyclodextrin-grafted poly (ethylene glycol)/poly (L-glutamic acid) diblock copolymer*

*and their inclusion complexes with CPT*. Colloids and Surfaces B: Biointerfaces. 113 (2014): 230-6.

8. H.Meng, K. Xu, Y. Xu, P. Luo, F Du, J. Yu,. *Nanocapsules based on mPEGylated artesunate prodrug and its cytotoxicity*. Colloids and Surfaces B: Biointerfaces. 115 (2014): 164-9.

# Contents

# List of symbols and abbreviations

| | |
|---|---|
| RE | rare-earth metals |
| $REH_3$ | Rare-earth trihydrides |
| TMs | transition metals |
| $MH_x$ | metal hydrides |
| hcp | close-packed hexagonal |
| dhcp | double close-packed hexagonal |
| fcc | face centered cubic |
| bcc | body centered cubic |
| c or a | lattice parameters |
| O sites | octahedral sites |
| T sites | tetrahedral sites |
| $O_v$ | H at the octahedron sites vibrates vertically to the c plane |
| $O_h$ | H at the octahedron sites vibrates horizontally to the c plane |
| $T_h$ | H at the tetrahedron sites vibrates horizontally to the c plane |
| $T_v$ | H at the tetrahedron sites vibrates vertically to the c plane |
| P | pressure |
| T | temperature |

| | |
|---|---|
| Tc | Critical temperature, the temperature at which a conductor becomes a superconductor |
| V | volume |
| U | internal energy |
| S | enthalpy |
| Q | heat |
| W | work |
| H | entropy |
| G | Gibbs free energy |
| F | Helmholtz free energy |
| $k_T$ | isothermal compressibility |
| $k_S$ | adiabatic compressibility |
| $C_v$ | the heat capacity at constant volume |
| $C_p$ | the heat capacity at constant pressure |
| $\gamma_{th}$ | thermal Grüneisen parameter |
| $\gamma_i$ | mode Grüneisen parameter |
| EOS | equation of state |
| B | bulk modulus |
| $B_T$ | bulk modulus at constant temperature |
| $B_S$ | bulk modulus at constant enthalpy |
| B' | the first derivative of B with respect to P |

| | |
|---|---|
| DAC | diamonds anvil cell |
| PTM | the pressure transmitting media |
| ADXRD | angle-dispersive X-ray diffraction |
| EDXRD | energy-dispersive X-ray diffraction |
| E | the energy of X-ray phonons (in KeV) |
| $\theta$ | the angle between the incident and diffracted beams |
| $\lambda$ | wavelength of beam |
| $\Delta\lambda$ | the shift of ruby R2 line ($\lambda$ = 694.2 nm) |
| $d_{hkl}$ | interplanar distance (in Å) |
| HP Ge | high purity germanium |
| CCD | the charged-coupled device |
| $\nu_0$ | the frequency of the incident beam |
| $\nu_m$ | the vibrational frequency of the excitations |
| h | planck constant |
| Å | angstrom, $10^{-10}$ m |
| GPa | gigapascal, $10^9$ Pa |
| MBar | megabar, $10^6$ Bar, ~$10^2$ GPa |
| KeV | kiloelectron volts |

# List of figures and tables

## Figures

## Tables

# Abstract

Metal hydrides, considered as promising hydrogen-storage material and potential high-temperature superconductors, have attracted increasing attention from researchers in the fields of physics and material sciences. The most efficient way to produce hydrides is the employment of high hydrogen pressure, which increases dramatically the chemical potential of hydrogen. The recent development of high-pressure diamond anvil cell (DAC) technique allowed a series of metal hydrides to be synthesized: $RhH_2$, $IrH_3$, $FeH_3$.

This dissertation aims to seek new metal hydrides and further investigate their structural properties by means of high-pressure energy-dispersive X-ray diffraction and Raman spectroscopy. In this thesis, our studies are mainly divided to two parts. The first part focuses on high-pressure structural investigations of selected rare-earth metal hydrides. Our aim is to continue and try to complete the systematic high-pressure study on the remaining rare-earth (RE) metal hydrides. In the second part, we are devoted into seeking and synthesis of new transition metal (TM) hydrides by using high-pressure of hydrogen gas in diamond anvil cells (DACs).

This thesis is composed of four chapters. Chapter 1 gives a comprehensive introduction of the studies and provides related background knowledge of the high-pressure experimental techniques employed in this thesis: high-pressure energy-dispersive X-ray diffraction and high-pressure Raman spectroscopy.

Chapter 2 presents the structural investigations on rare-earth trihydride, specifically, trihydrides of dysprosium and lanthanide. Synchrotron X-ray and Raman scattering investigations have been performed on dysprosium trihydride at high pressure up to 40 GPa. As predicted by theoretical calculation and other studies, dysprosium trihydride

was observed underwent an hexagonal-to-cubic phase transformation similar to those of other heavy lanthanide trihydrides. These studies completed the overall picture of hexagonal to cubic phase transition for the whole $ReH_3$ compounds since dysprosium trihydride is the last one that has not been studied so far among the heavier lanthanide trihydrides family. $LaH_3$ and $LaD_3$ were chosen to be studied at high pressure due to the appearance of unknown rich peaks in our preliminary Raman measurements. The stoichiometric lanthanum trihydride and deuteride undergo pressure-induced phase transformation presumably of hydrogen ordering origin similar to that observed in the heat capacity measurements at low temperature.

Chapter 3 elucidates our recent achievements in the high-pressure investigations of the selected transition metals, molybdenum and tantalum, under high pressure of hydrogen in diamond anvil cell. The molybdenum-hydrogen system was studied in a diamond anvil cell at high hydrogen pressure up to 30 GPa at room temperature by X-ray diffraction. A phase transformation was observed of a bcc metal to a hydride with an hcp metal lattice and H/Mo≈1.1 at pressure around 4 GPa; the hydrogen content of the hydride increase with pressure increase in the pressure range of 4-15 GPa; eventually the hydrogen content reached saturation around 15 GPa with ratio H/Mo of 1.35(10) evaluated from the volumetric consideration. Although the theoretical calculation predicted the formation of dihydride we failed to obtain it. With respect to the tantalum-hydrogen system, we investigated it by x-ray diffraction in a diamond-anvil cell at room temperature in the pressure range up to 41 GPa. A substoichiometric tantalum monohydride with a distorted bcc structure was formed at 5 GPa and its hydrogen content reaches H/Ta = 0.92(5); a new hydrogen-rich phase of tantalum with an hcp metal lattice was found at higher pressure and its hydrogen content was independent of pressure. The single-phase hydrogen-rich phase was synthesized at a hydrogen pressure of 9 GPa in a toroid-type high-pressure apparatus and possess an hcp metal lattice with a = 3.224(3) and c = 5.140(5)A° at T = 85 K investigated by X-ray diffraction. The hydrogen content

determined by thermal desorption was H/Ta = 2.2(1). The tantalum dihydride was successfully synthesized and possesses hexagonal metal lattice, unlike niobium and vanadium dihydrides which based on a fluorite structure.

In Chapter 4, a brief overview of the whole studies and final conclusions is given.

# Chapter 1. **Introduction**

## 1.1 Hydrides

### 1.1.1 Category

Hydrides are defined as a set of compounds that hydrogen combines with another element in periodic table. Based on the nature of the hydrogen bonds, hydrides have been classified into three principal categories, namely covalent or volatile, saline or ionic, and metallic. Each category has its distinct properties. Saline hydrides are formed by the reaction of strongly electropositive alkali and alkaline-earth metals with hydrogen, which is strongly electronegative due to electron transfer. Covalent hydrides contain hydrides formed by the elements from Group 11 to 17 with hydrogen. Some complex hydrides are also assigned to this category. Metallic hydrides include most hydrides formed by the Transition Metals (TMs), expect the element Group 11 and 12. Although such classification is not always depictive, for example, the rare-earth (RE) hydrides are regarded as metallic hydrides, exhibiting some characteristics similar to those of saline hydrides. It is still helpful and useful to better understand the differences in hydrides. The categories are clearly presented in **Fig.** 1.1.

Saline hydrides consist of the monohydrides of the alkali metals and the dihydrides of the alkaline-earth metals with the exception of beryllium. Following the first publication[9] on the reaction between hydrogen and any of the alkali or alkaline-earth metals between 1808 and 1811, researchers tried to figure out the composition of these hydrides. Consequently, the alkali-metal hydrides were determined as monohydrides[10] and the alkaline-earth metal hydrides are dihydrides without evidence of the existence of subhydrides[11]. Although scientists put their effort into preparing of beryllium dihydride,

they failed to obtain a pure form of beryllium dihydride until 1951. It was obtained by treating dimethylberyllium $Be(CH_3)_2$ with lithium aluminum hydrides, $LiAlH_4$. Unlike the other alkaline-earth metal hydrides, it possesses covalent bonds, namely, three-center two-electron bond.

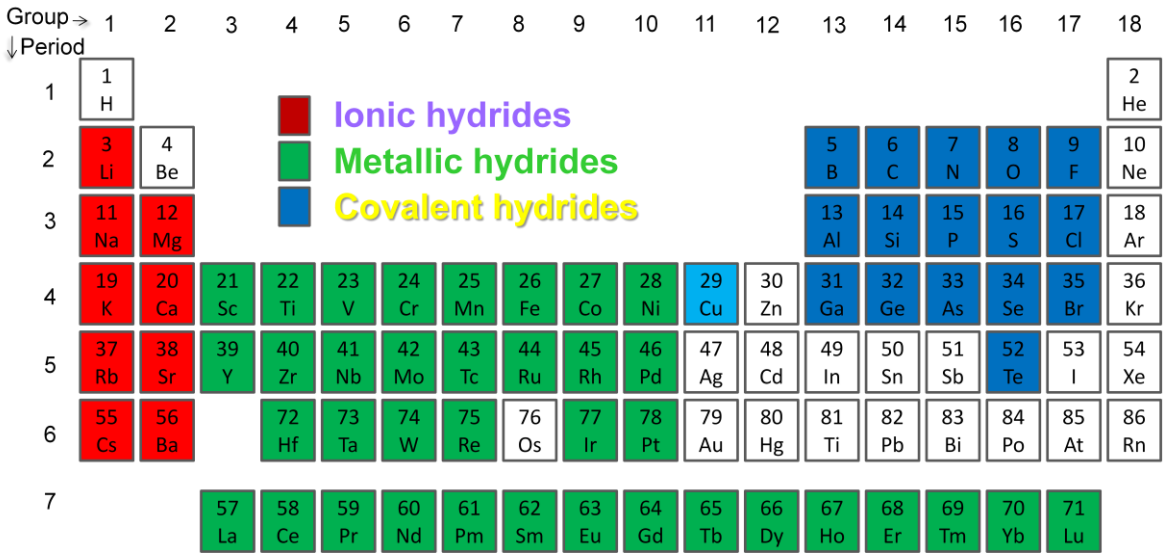


**Fig.** 1.1 The bonds properties of binary hydrides in periodic table.

Covalent hydrides contain hydrides formed by the elements from group 11 to group17. Only copper form covalent monohydride, none of the other metals from Group 11 to 12 form simple binary hydrides. The solubility of hydrogen in the other metals is considerably low, usually to the extent of $10^{-4}$. In the case of gold, hydrogen is not soluble to any measurable extent. The elements of Group 14 to 17 all form hydrides with normal covalent bonds in which the hydrogen is bounded by a single bond to the element. In contrast, the elements of Group 13 (as typified by boron) all exhibit a second type of covalent bond: the electron deficient hydrogen bridged bond. In this type of bond, the hydrogen nucleus is embedded in a molecular orbital that covers more than two atoms to create a multi-center two-electron bond. Aluminum hydride can be obtained from the direct reaction of aluminum and high-pressure hydrogen gas at room temperature.

The most interesting part is the TM hydrides. As shown most of the TM elements form metallic hydrides reacting with hydrogen. Only copper from Group 11 and 12 can form monohydride and, interestingly, it can form both covalent and metallic hydride[12]. The hydrides from group 3 to 10 will be discussed late in Chapter 3. The RE metal regarding as inner TMs, which contain lanthanide as well as scandium and yttrium, will be shown in details in Chapter 2.

### 1.1.2 The locations of hydrogen atoms in the hydrides

The positions or locations of hydrogen atoms in the hydrides are particularly important and intensively studied by both the theorists and experimentalists. For metal hydrides, the hydrogen atoms usually occupied interstitial sites in the metal lattice. The three typical structures of metal lattice of hydrides, namely face-centered cubic (fcc), close-packed hexagonal (hcp) and body-centered cubic (bcc) are shown in **Fig. 1.2**. When the hydrogen atoms are absorbed during formation of metal hydrides, the specific sites octahedral and tetrahedral sites are occupied by H atoms. In most hydrides, the H atoms locate at slightly distorted interstitial sites rather than ideal octahedron or tetrahedron sites. The metal lattices of hydrides are determined by X-ray diffraction in the experiments. In order to locate the position of H atoms, the neutron diffraction or inelastic neutron scattering are necessary to be performed. In most cases, neutron experiments were performed on deuterides instead of hydrides resulting from lager coherent cross section and smaller incoherent cross section in D than in H. While, the location of H and D in the corresponding hydrides and deuterides are not necessarily always the same. In the fcc lattice, a T and O site is surrounded by the nearest metal regular atoms located in octahedral and tetrahedral sites, respectively. As O sites in fcc lattice are fully occupied, the number of O intensities per metal atom is one. In the case of T sites, the number per metal atom is two. In hcp lattice, the polyhedron formed by the nearest metal atoms usually appear to be distorted due to the deviation of the axial ratio from the ideal value

of 1.633. The number of O and T sites per metal atom in hcp lattice is the same as that of O and T sites in fcc lattice. This is because the nearest neighbors for close-packed structure - both fcc and hcp - are the same. In the bcc lattice, the O sites and T sites are always surrounded by strongly distorted polyhedron formed by the metal atoms. hence, both o sites and T sites in bcc lattice can be further divided into three groups depending on the direction of their four-fold symmetry axis. The number of O sites per metal atom in bcc lattice is three and that of T sites per metal atom is six.

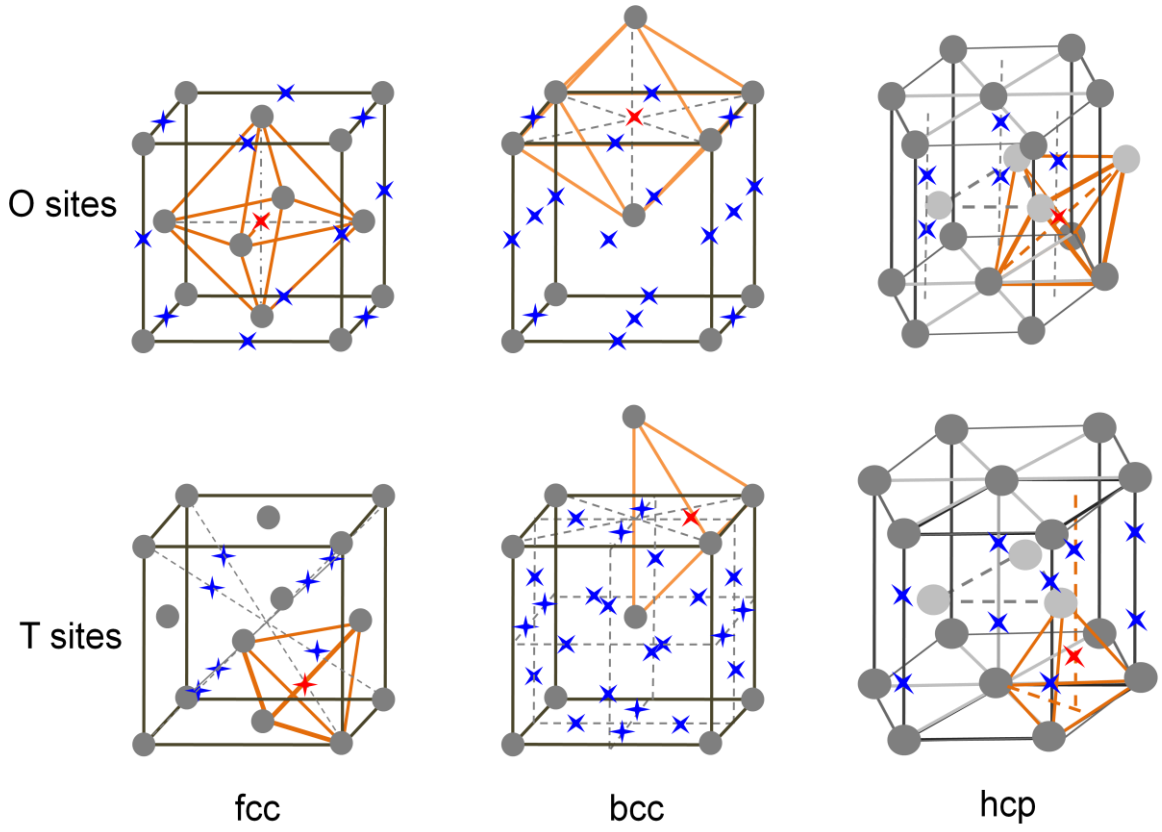


**Fig. 1.2** Interstitial sites in hcp, fcc and bcc lattices[13]. Octahedral (O) sites and Tetrahedral (T) sites.

### 1.1.3 Potential application

Hydrides have several potential applications. Firstly, as promising hydrogen storage materials, hydrides provides numbers of advantages over other conventional methods of either as compressed gas in highly pressurized tanks or as the liquid in cryogenic tanks. One of the advantages is that metal hydrides are capable of storing large amounts of

hydrogen, namely, high volumetric hydrogen storage densities. Additionally, metal hydrides as solid-state hydrogen storage container are inherently safer compared with the mechanical hydrogen storage methods due to the low pressure needed during the hydrogen absorption process. Hence, they are desirable to use as hydrogen carriers for the on-board vehicular application. Secondly, since hydrogen atoms in metallic or covalent hydrides provide the necessary high-frequency phonon modes as well as the strong electron-phonon coupling, in principle, the conditions for superconductivity based on Bardeen-Copper-Schrieffer theory are fulfilled. Recently, the sulfur hydride was observed to exhibit superconductivity with the highest Tc of 203 K[14] at high pressure. Afterwards, $LaH_{\sim 10}$ was reported to show superconductivity with a record Tc of 250 K at ~170 GPa[15]. Those retriggers scientists in search of room temperature superconductors among hydrides.

Since hydrides exhibit such prospective applications, the discovery of new hydrides and the investigations on physical properties of both new hydrides and existed hydrides appear to be of high significance. In this thesis, our studies are mainly divided into two parts. The first part focuses on high-pressure structural investigations of selected RE metal hydrides. Our aim is to continue and try to complete the systematic high-pressure study on the remaining RE metal hydrides. The details will be described in Chapter 2. In the second part, we are devoted into seeking and synthesis of new TM hydrides by using high-pressure of hydrogen gas. The experiments and results are depicted in Chapter 3.

# 1.2 Thermodynamics Under High Pressure

## 1.2.1 Fundamental of Thermodynamics[16]

In thermodynamics, hydrostatic pressure (P), volume (V), and temperature (T) are fundamental quantities. The first law of thermodynamics applies the conversation of total energy any infinitesimal process in a closed system:

$$dU = \delta Q + \delta W \tag{1.1}$$

where dU represents the infinitesimal change in internal energy, $\delta Q$ is the infinitesimal heat absorbed by the system and $\delta W$ is the work done on the system.

When a closed system undergoes a reversible process, the work done by the system is given by the work effected on the system $\delta W = -PdV$ and the heat absorbed by the system is given by $\delta Q = TdS$, thus the change in internal energy can be simply as

$$dU = TdS-PdV \tag{1.2}$$

where dU is expressed based on two independent variables: entropy and volume.

As the enthalpy H is defined as

$$H = U+PV \tag{1.3}$$

By combining the definition and Equation 1.2, the change in the enthalpy for a closed system during a reversible process is written as

$$dH = TdS + VdP \tag{1.4}$$

Likewise, the change in the Helmholtz free energy dF and in the Gibbs free energy dG are given as

$$dF = -SdT-PdV \tag{1.5}$$

$$dG = =-SdT+VdP \tag{1.6}$$

Moreover, a number of relations are derived from the above equations, such as

$$T = \left(\frac{\partial U}{\partial S}\right)_V, \quad P = -\left(\frac{\partial U}{\partial V}\right)_S \quad \text{(from U)} \tag{1.7}$$

$$T = \left(\frac{\partial H}{\partial S}\right)_P, \quad V = \left(\frac{\partial H}{\partial P}\right)_S \quad \text{(from H)} \tag{1.8}$$

$$S = \left(\frac{\partial F}{\partial T}\right)_V, \quad P = \left(\frac{\partial F}{\partial V}\right)_T \quad \text{(from F)} \tag{1.9}$$

$$S = -\left(\frac{\partial G}{\partial T}\right)_P, \quad S = \left(\frac{\partial G}{\partial P}\right)_T, \quad \text{(from G)} \tag{1.10}$$

By calculating the mixed second derivatives of the thermodynamic potentials, we obtain the Maxwell relations:

$$\left(\frac{\partial P}{\partial S}\right)_V = -\left(\frac{\partial T}{\partial V}\right)_S \quad \text{(from U)} \tag{1.11}$$

$$\left(\frac{\partial V}{\partial S}\right)_P = \left(\frac{\partial T}{\partial P}\right)_S, \quad \text{(from H)} \tag{1.12}$$

$$\left(\frac{\partial P}{\partial T}\right)_V = -\left(\frac{\partial S}{\partial V}\right)_T, \quad \text{(from F)} \tag{1.13}$$

$$\left(\frac{\partial V}{\partial T}\right)_P = \left(\frac{\partial S}{\partial P}\right)_T, \quad \text{(from G)} \tag{1.14}$$

The relations between thermodynamic potentials allow the variation experimentally accessible although it cannot be measured directly. Specifically, the equation of state,

which play an essential role in material science, can be obtained either from $P = \left(\frac{\partial F}{\partial V}\right)_T$ or $P = -\left(\frac{\partial U}{\partial V}\right)_S$. It will be described in detail in the following section.

The compressibility of materials is describing the corresponding volume change when the materials undergo pressure change. The isothermal compressibility ($k_T$) and adiabatic compressibility ($k_S$) are defined as with unites of pressure$^{-1}$:

$$k_T = -\frac{1}{V}\left(\frac{\partial V}{\partial P}\right)_T = -\frac{1}{V}\left(\frac{\partial^2 G}{\partial P^2}\right)_T \quad (1.15)$$

$$k_s = -\frac{1}{V}\left(\frac{\partial V}{\partial P}\right)_S = -\frac{1}{V}\left(\frac{\partial^2 H}{\partial P^2}\right)_S \quad (1.16)$$

The bulk modulus (B), defined as the inverse of the compressibility, is commonly used in material science. The relations between bulk moduli and thermodynamic potentials are given by:

$$B_T = -V\left(\frac{\partial P}{\partial V}\right)_T = -V\left(\frac{\partial^2 F}{\partial V^2}\right)_T \quad (1.17)$$

$$B_S = -V\left(\frac{\partial P}{\partial V}\right)_S = -V\left(\frac{\partial^2 U}{\partial V^2}\right)_S \quad (1.18)$$

The bulk modulus has unit of pressure and reveals the elastic response of solids to hydrostatic compression. The difference between $B_T$ and $B_S$ is negligible and thus they are often employed interchangeably.

Thermal Grüneisen parameter ($\gamma_{th}$), which reflects the change in the vibrational characteristics in response to the volume change, is given by

$$\gamma_{th} = \frac{V}{C_v}\left(\frac{\partial S}{\partial V}\right)_T = \frac{V}{C_P}\left(\frac{\partial P}{\partial T}\right)_V \quad (1.19)$$

where $C_v$ and $C_p$ are the heat capacity at constant volume and pressure, respectively.

### 1.2.2 Equation of State (EOS)

The Equation of State is functional relation of the state variables. As shown above, the isothermal EOS for a solid is defined as follow:

$$B = -V\left(\frac{\partial P}{\partial V}\right)_T$$

From equation 1.17, the pressure is related with volume and internal energy as $P(V) = \left(\frac{\partial U}{\partial V}\right)_S$. Thus, the bulk modulus can be rewritten as the second derivative with respect to the volume:

$$B(V) = V\left(\frac{\partial^2 U}{\partial V^2}\right)_{T,S} \tag{1.20}$$

Its first derivative with respect to the pressure at constant temperature is defined as:

$$B' = \left(\frac{\partial B}{\partial P}\right)_T \tag{1.21}$$

## A Murnaghan EOS

In 1944, by supposing that the bulk modulus is linearly change in response to the pressure change, Murnaghan[17] proposed his famous equation of state:

$$U(V) = U_0 + \frac{BV}{B'}\left[\left(\frac{V_0}{V}\right)^{B'} \frac{1}{B'-1} + 1\right] - \frac{BV_0}{B'-1} \tag{1.22}$$

where $V_0$ and $U_0$ are the equilibrium volume and energy, at zero pressure. By applying equation (1.20) to equation (1.22), Murnaghan's EOS is obtained as

$$P(V) = \frac{B}{B'}\left[\left(\frac{V_0}{V}\right)^{B'} - 1\right] \tag{1.23}$$

The Murnaghan's EOS can be rewritten in the form of the volume as a function of pressure:

$$V(P) = V_0 \left[1 + P(\frac{B'}{B})\right]^{-1/B'} \quad (1.24)$$

### B Birch-Murnaghan EOS

The third-order Birch-Murnaghan isothermal equation of state published in 1947[18] is given by:

$$U = U_0 + \frac{9V_0B}{16}\left\{[(\frac{V_0}{V})^{\frac{2}{3}} - 1]^3 B' + [(\frac{V_0}{V})^{\frac{2}{3}} - 1]^2 \left[6 - 4\left(\frac{V_0}{V}\right)^{\frac{2}{3}}\right]\right\} \quad (1.25)$$

Likewise, the third-order Birch-Murnaghan's EOS is presented as follow:

$$P(V) = \frac{3B}{2}[(\frac{V_0}{V})^{\frac{7}{3}} - (\frac{V_0}{V})^{\frac{5}{3}}]\left\{1 + \frac{3}{4}(B' - 4)[(\frac{V_0}{V})^{\frac{2}{3}} - 1]\right\} \quad (1.26)$$

The second-order Birch-Murnaghan's EOS is obtained by simplifying the third-order Birch-Murnaghan's EOS with B' at a fixed value of 4,

$$P(V) = \frac{3B}{2}[(\frac{V_0}{V})^{\frac{7}{3}} - (\frac{V_0}{V})^{\frac{5}{3}}] \quad (1.27)$$

## 1.3 High-pressure Technique

### 1.3.1 Overview

High-pressure research is an extremely attractive field both for its scientific interest and its industrial applications. When materials are subjected to high pressure, the fascinating changes in chemical and physical properties occur. However, high-pressure research is a field highly relying on instruments and techniques. At the beginning the developments in

high-pressure technique have been driven by the quest to obtain synthetic diamonds. Later on in 1935 [19],[20], the hydrogen was predicted to become a metal under high pressure in a publication[21]. Conversely, the managements of achieving estimate transition pressures stimulus the invention of high-pressure devices.

Roughly, the development of high-pressure technique is divided into three stages, the Bridgman era, post-Bridgman era, and diamond anvil cell (DAC) era. Percy Bridgman, as one of the pioneers in the high-pressure field, won Nobel Prize for his contribution in 1946[22]. From 1910 to 1950, the era was dominated by the so-called Bridgman anvil and the piston-cylinder device and named after Bridgman. In Bridgman era, the pressure up to 10 GPa is attainable. In the post-Bridgman era, the pressure range was extended to several tens GPa by Drickarner and his colleagues[23],[24], who developed the ultra-high-pressure anvil instruments supported for resistance, Mossbauer, x-ray diffraction, and optical absorption measurements. Meanwhile, the belt apparatus and multiple-anvils cells improved upon the piston-cylinder device[25] became the popular tools in the high-pressure field for materials synthesis and studies of phase transitions at high pressure and high temperature. The introduction of diamonds in high-pressure technique is a quite revolution in high-pressure research. Instead of steel anvils in Bridgman anvil, two opposed diamonds are employed in DAC. In DAC, the samples are placed in the flat paralleled faces of the two diamonds. When a force is applied between the two opposed diamonds, samples in DAC are subjected to the corresponding pressure. Since the original version of the NBS DAC invented in 1959 by NBS[26], the DAC device is modified by the introduction of the metal gaskets[27] for hydrostatic pressure generation, tiny ruby as the pressure sensor, and hydrostatic pressure transmitting media. The DAC fast become the most powerful and popular high-pressure device, accumulating a lot of new results in high-pressure filed. With the DAC, the pressure attainable are extended up to ~800 GPa, much higher than the evaluated pressure in the core of the earth (~360 GPa).

Modern high-pressure research can be investigated in two ways, experimentally and computationally. The theoretical calculations develop rapidly benefited from the high-performance computer. Although some predictions based on the theoretical calculations can direct the experimentalists, the experimental method is still more reliable in the high-pressure field. To some degree, the theoretical calculations are helpful mostly when the experiments are not feasible or difficult to explain.

High pressure is a very hot field. The high-pressure techniques have a wide range of applications, from the astrophysics and geophysics to materials physics and even the food industry. Since the existed textbook usually describes the chemistry rules that are applicable at zero-pressure, the behavior of materials subjected to extreme compression is rather poorly understood. The high-pressure research thus is more meaningful and interesting.

In this thesis, with the help of DAC, we studied the behaviors of some selected RE trihydrides at high pressure. Also, the TMs molybdenum and tantalum are investigated under high-pressure hydrogen gas.

### 1.3.2 Diamond Anvil Cells[25]

The DAC is the most powerful and popular tool to generate hydrostatic pressure. The essential part of the DAC is the two paralleled opposed diamonds as illustrated in **Fig.** 1.3. The basic working principle is very simple. Between the two diamonds, a foil of metal sheet is employed as a gasket. In the center of the gasket, a hole with a reasonable size is drilled as a sample chamber. When the force is applied on the diamonds, the pressure on the sample and gasket generated simultaneously. In general, the pressure inside the DAC is measured by the pressure sensor, e. g. ruby. The essential elements of the DACs, e.g. anvil diamonds, gasket, pressure sensor, and pressure transmitting media, are described in detail below.

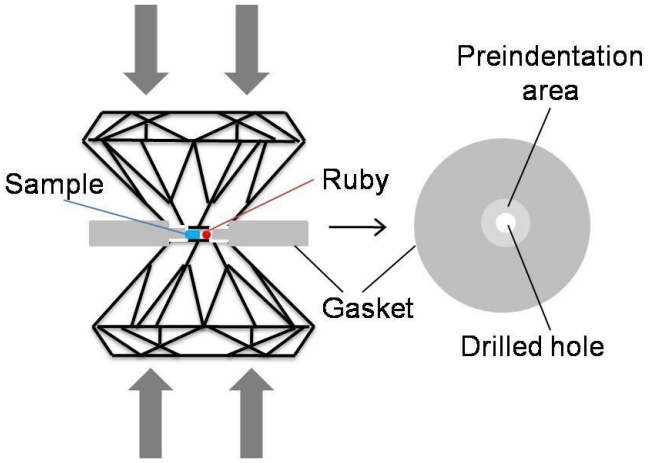


**Fig.** 1.3 The opposed diamonds anvils with a metal gasket; A hole was drilled at the center of the pre-indented gasket.

The brilliant-cut diamonds are usually used in the high-pressure tools. The typical size of the diamonds employed in DAC varies from 1/8 to 1/2 carat depending on the type of DAC and the purpose of the study. The culet size of two opposed diamonds are usually similar to each other and in a range of 0.3-0.7 mm. The type of diamonds used in DAC relies on the purpose of the investigation. Type II diamond was chosen in DAC for light scattering studies since it has very low luminescence. However, a luminescent diamond was selected to be used in DAC for X-ray investigation due to its good transparency to X-ray.

The introduction of the gasket into the DAC was pioneered by Van Valkenburg[27], who firstly used gasket for containment of hydrostatic transmitting media in the DAC. The DAC was widespread as a quantitative tool in the high-pressure field later on. Metal foils with an initial thickness from 0.25mm to 0.2mm are commonly employed as the gasket. Generally, the gasket metal foil is fixed on the lower diamond. A hole with the size varying from 0.2 mm to 0.1 mm was drilled served as a sample chamber. Besides providing containment of sample, the indented gasket also served as supporting material between two opposed diamonds as the force applied on the DACs.

Another big progress in the development of DACs is the introduction of ruby as the pressure calibration in the high-pressure measurements. Previously, the pressure is calibrated by force over the area or fixed point methods. In 1972, the shift of ruby R lines was found linearly depending on the pressure in the range of 1-22 kbar by using several known liquid freezing points and some solid-solid transition points[28]. Later on, further efforts were put into the studies of the relation between the ruby R lines and pressure[29]. Until 1978, Mao et al[30] concluded the pressure is related to the shift of ruby R lines by the equation shown below,

$$P(\text{Mbar}) = 3.808[(\Delta\lambda/6942+1)^5 - 1] ,$$

where $\Delta\lambda$ is the shift of ruby R2 line ($\lambda$ = 694.2 nm) and the pressure P estimated from the equation has the unit of Mbar. According to the equation, the pressure is well linearly dependent on the wavelength shift of ruby R2 line in the pressure range of 200 Kbar and positive correction is needed for the linear scale as pressure is higher than 200 Kbar. The equation is the only equation supported by the experimental data for the pressure calibration with the pressure higher than 300 Kbar (30GPa) and the uncertainty on P determined by the this equation is suugested to be around 2 GPa at 150 GPa by Dewaele[31]. Alternatively, the anvil diamond is also proposed to be employed as pressure scale due to its first-order Raman band shift with pressure and, specifically, it is recommended to use diamond scale up to 310 GPa[32] and even higher pressure.

The pressure transmitting media (PTM) are of significance since they may produce hydrostatic conditions for investigated samples under pressure. Non-hydrostatic conditions have misled the researchers to report the fake "new" or "anomalous" pressure effect. The good PTM should have the following properties: chemical inertness, zero shear stress, low cost and easy to load. In the 1970s, Piermarini et al[33] introduced the mixture of 4:1 methanol-ethanol as PTM, which stayed hydrostatic up to 10 GPa at room temperature. Since then, lots of PTM have been used and tested. The mixed fluids of 16:3:1 water-methanol-ethanol allowed to extend the hydrostatic conditions up to

14.5 GPa. The fluid silicone oils are also commonly used due to its easy loading property. It is worth mention that elemental gases (such as nitrogen, neon, and helium) remain hydrostatic even in their solid phases. Solid rare gases are well used in low-temperature high-pressure experiments with gas-loading techniques either cryogenically or under high-pressure corresponding gas. Lead and indium are alternative options in low-temperature measurements resulting from their low shear strengths rarely depend on pressure and temperature.

### 1.3.3 High-pressure EDXRD

X-ray diffraction is a significant tool for determining the structure of the specimen in material science. There are two different X-ray diffraction techniques, namely angle-dispersive X-ray diffraction (ADXRD) and energy-dispersive X-ray diffraction (EDXRD). Both are applicable in the high-pressure field. While the special design in DACs employed in ADXRD is necessary since the window of DAC limits the diffraction angle. EDXRD thus has its own advantage due to the fixed diffraction angle during the measurements. Almost all types of DACs are feasible for EDXRD. The solid-state detector of EDXRD enables a rapid record of diffraction data, suggesting the promising application in *in-situ* measurements.

#### A Theory of EDXRD

The fundamental of X-ray diffraction is constructive interference of monochromic X-ray. For EDXRD method, the Bragg's law $n\lambda=2d_{hkl}\sin 2\theta$ can be rewritten as

$$Ed_{hkl}\sin 2\theta = 6.1999,$$

where E (in KeV) represents the energy of X-ray phonons which is incident and diffracted at a fixed angle $\theta$ by the paralleled planes with the interplanar separation of $d_{hkl}$ (in Å). In the high-pressure in situ EDXRD measurements, the diffraction data are

collected by a solid-state detector at a defined angle 2θ. Thus the inverse relation of E and $d_{hkl}$ indicates that the higher energy of X-ray allows determining the smaller interplanar distance of $d_{hkl}$.

## B Setup of EDXRD

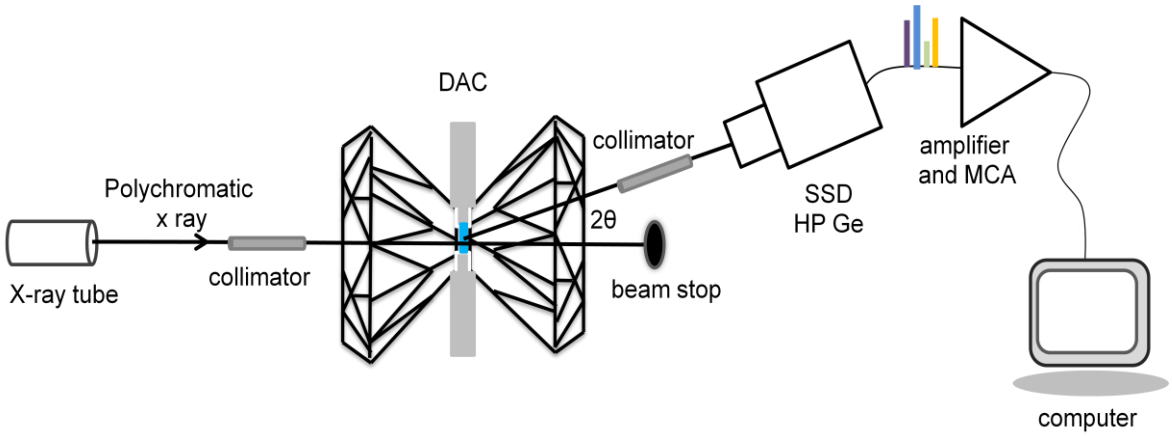


**Fig.** 1.4 Simplified scheme of the EDXRD setup used with DACs.

As shown in **Fig.** 1.4, the high-energy white X-ray beam is generated by an X-ray tube. Then the X-ray beam is collimated and incident on the sample. The diffraction X-rays are recorded by a solid-state detector (high purity germanium) at a fixed angle 2θ. The output of the detector is amplified and analyzed by the multichannel analyzer. The solid-state detector combined with multichannel analyzer allows the real-time detection, which provides online viewing during the data collection. This makes EDXRD a better device for the kinetic study of the specimen under high pressure.

### 1.3.4 High-pressure Raman Spectroscopy

## A Theory of Raman spectroscopy

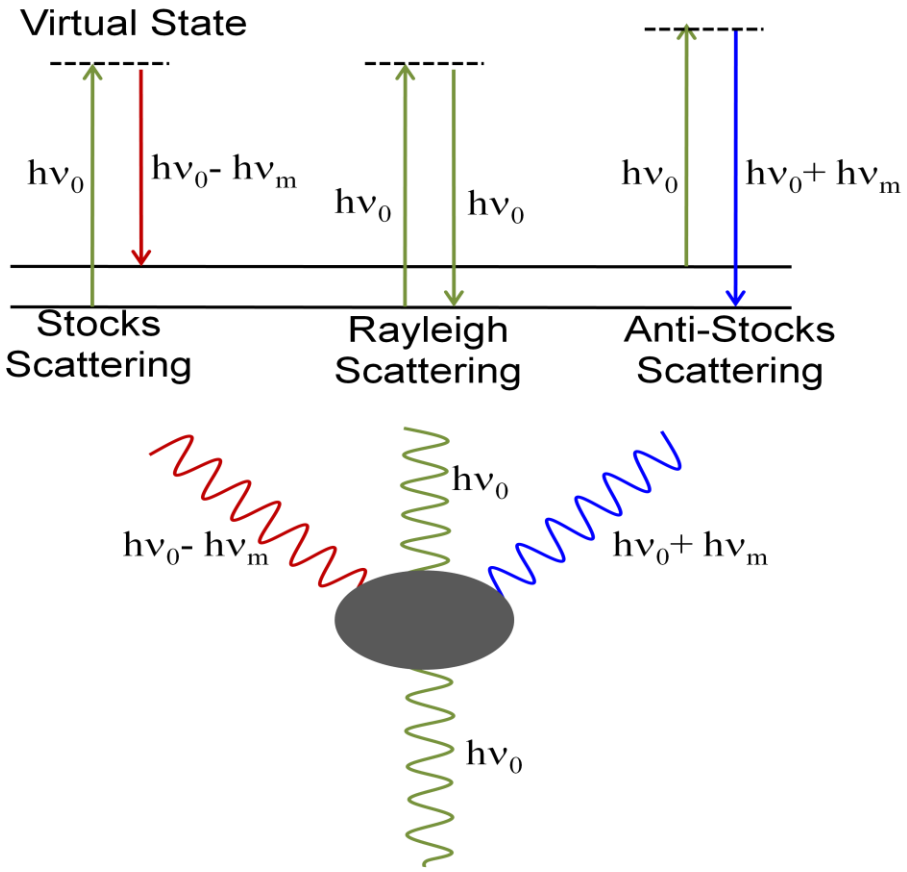


**Fig.** 1.5 The mechanism of Raman scattering. $\nu_0$ denotes initial frequency and $\nu_m$ represents the vibrational frequency of the excitations.

The Raman spectroscopy works based on inelastic scattering. In conventional Raman spectroscopy, a specimen can be excited to a virtual state by the laser beam with initial frequency $\nu_0$. The obtained scattered light is divided into two types: (1) Rayleigh scattering, also called as elastic scattering, dominates in the scattering light and has the same energy as the incident laser beam ($h\nu_0$); (2) Raman scattering, also called as inelastic scattering, is extremely weak and consists of Stokes scattering (with frequency

$\nu_0 - \nu_m$) and anti-Stokes scattering (with frequency $\nu_0 + \nu_m$). $\nu_m$ represents the vibrational frequency of the excitations, which can be vibrons in a molecule, phonons in an ordered crystal structure. The Raman spectroscopy records the vibrational frequency $\nu_m$, the shift from the incident beam frequency $\nu_0$.

As illustrated in **Fig.** 1.5, three different potential output can occur when a sample is irritated by the incident beam with frequency $\nu_0$. In general, the incident laser beam interacts with the electrons in the molecules and results in polarization in molecules. The molecules are excited to virtual states and then relax back to the vibrational states. For Rayleigh scattering, the excitations emit a photon possessing the same energy as the incident photon ($h\nu_0$). The Rayleigh scattering is super intense because most photons scatter this way. The excitations are excited by the incident photon ($h\nu_0$) to virtual state and then relax back to the high energy vibrational level accompanying with emitting photons with less energy ($h\nu_0$-$h\nu_w$) than the incident photons, this is called Stocks scattering. In contrast, the excitations are excited by the incident photon ($h\nu_0$) to virtual state and relax back to the lowest energy vibrational level with emitting photons with more energy ($h\nu_0$+$h\nu_w$) than the incident photons, this is called anti-Stocks scattering. Both Stocks and anti-Stocks scattering processes are defined as Raman scattering since there is energy loss or gain during scattering. In fact, Stokes scattering is usually more intense than anti-Stokes scattering since most of the molecules are found in the ground vibrational states. Consequently, it is customary to record only Stokes shift in Raman spectroscopy.

## B The setup of Raman Spectroscopy with DAC[34]

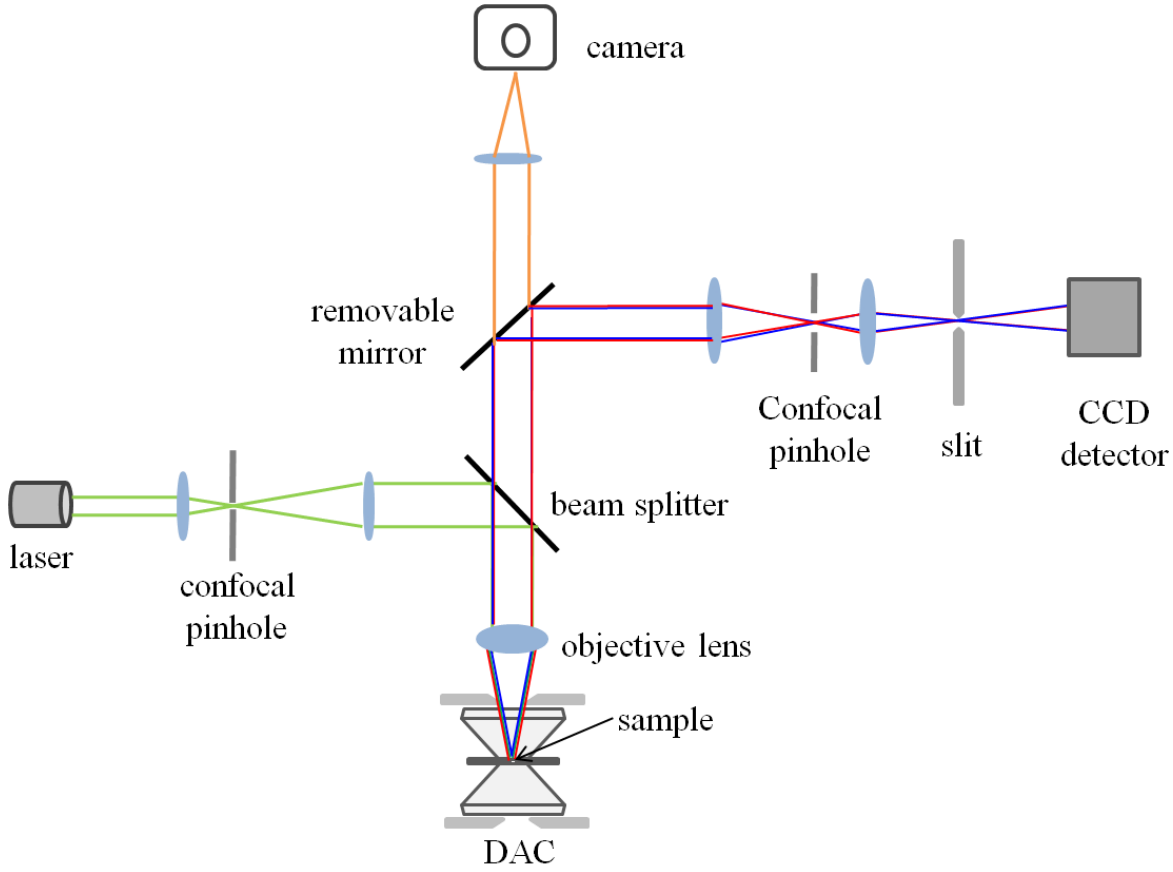


**Fig.** 1.6 Simplified scheme of the Raman scattering setup with DAC in backscattering geometry.

A typical Raman setup used in the high-pressure field is illustrated in **Fig.** 1.6. The fundamental components of the Raman scattering setup include the laser source, various optical lens and charged-coupled device (CCD) detector. In short, during Raman measurement, the sample is struck by the incident laser beam and then the Raman scattering is collected by the CCD detector. However, it is not easy to perform Raman measurements since the intensity of inelastic scattering (Stokes scattering and anti-Stokes scattering) is extremely weak compared with elastic scattering (Rayleigh scattering). Thus efficiently recording the Raman signal at high pressure is more challengeable.

The gas lasers in the range of UV-Vis-NIR are commonly chosen as the excitation light since a high intensity and highly monochromatic laser beam is preferred in order to get a signal-to-noise ratio in Raman measurements. The incident laser beam is monochromatized by bandpass filter and focused by confocal pinhole onto a notch filter (beam splitter). Then the light is reflected by notch filter at a right angle and redirected to the compressed sample inside a DAC. Plan objectives with large working distance are commonly employed in order to allow the monochromatic incident laser beam to focus onto the compressed sample inside a DAC. The light reflected by the diamond window and sample and the scattering light emitted by the sample is collected by the same objective in backscattering geometry. The notch filters are commonly used to block a narrow range of wavelength close to the incident beam and allow Raman signal to pass through. The Raman signals are guided by the removable mirror to pass through the confocal pinhole. It is worth mention that the application of the confocal pinhole highly improved resolution both in the axial direction and in the lateral plane. Finally, the Raman signal is collected by the CCD which works at low temperature and analyzed by computer with appropriate software.

# Chapter 2. **Rare-earth Trihydrides**

## 2.1 Literature Review

### 2.1.1 General Characteristics of the Rare-earth Metals

**Table** 2.1 Electronic Structure of the RE Elements [35]

| Element | Atomic Number | Neutral Atoms | | 3 Cation |
|---|---|---|---|---|
| | | Idealized | Probable | |
| Sc | 21 | $3d^1\ 4s^2$ | $3d^1\ 4s^2$ | $3s^2\ 3p^6$ |
| Y | 39 | $4d^1\ 5s^2$ | $4d^1\ 5s^2$ | $4s^2\ 4p^6$ |
| La | 57 | $5d^1\ 6s^2$ | $5d^1\ 6s^2$ | $5s^2\ 5p^6$ |
| Ce | 58 | $4f^1\ 5d^1\ 6s^2$ | $4f^2\ \ 6s^2$ | $4f^1\ 5s^2\ 5p^6$ |
| Pr | 59 | $4f^2\ 5d^1\ 6s^2$ | $4f^3\ \ 6s^2$ | $4f^2\ 5s^2\ 5p^6$ |
| Nd | 60 | $4f^3\ 5d^1\ 6s^2$ | $4f^4\ \ 6s^2$ | $4f^3\ 5s^2\ 5p^6$ |
| Pm | 61 | $4f^4\ 5d^1\ 6s^2$ | $4f^5\ \ 6s^2$ | $4f^4\ 5s^2\ 5p^6$ |
| Sm | 62 | $4f^5\ 5d^1\ 6s^2$ | $4f^6\ \ 6s^2$ | $4f^5\ 5s^2\ 5p^6$ |
| Eu | 63 | $4f^6\ 5d^1\ 6s^2$ | $4f^7\ \ 6s^2$ | $4f^6\ 5s^2\ 5p^6$ |
| Gd | 64 | $4f^7\ 5d^1\ 6s^2$ | $4f^7\ 5d^1\ 6s^2$ | $4f^7\ 5s^2\ 5p^6$ |
| Tb | 65 | $4f^8\ 5d^1\ 6s^2$ | $4f^9\ \ 6s^2$ | $4f^8\ 5s^2\ 5p^6$ |
| Dy | 66 | $4f^9\ 5d^1\ 6s^2$ | $4f^{10}\ \ 6s^2$ | $4f^9\ 5s^2\ 5p^6$ |
| Ho | 67 | $4f^{10}\ 5d^1\ 6s^2$ | $4f^{11}\ \ 6s^2$ | $4f^{10}5s^2\ 5p^6$ |
| Er | 68 | $4f^{11}\ 5d^1\ 6s^2$ | $4f^{12}\ \ 6s^2$ | $4f^{11}5s^2\ 5p^6$ |
| Tm | 69 | $4f^{12}\ 5d^1\ 6s^2$ | $4f^{13}\ \ 6s^2$ | $4f^{12}5s^2\ 5p^6$ |
| Yb | 70 | $4f^{13}\ 5d^1\ 6s^2$ | $4f^{14}\ \ 6s^2$ | $4f^{13}5s^2\ 5p^6$ |
| Lu | 71 | $4f^{14}\ 5d^1\ 6s^2$ | $4f^{14}5d^1\ 6s^2$ | $4f^{14}5s^2\ 5p^6$ |

The RE metals are one of a set of seventeen elements in the periodic table, specifically the fifteen lanthanides (from atomic number 57 to 71) together with scandium (atomic number 21) and yttrium ( atomic number 39)[36].

The electronic properties of the RE elements are shown in **Table 2.1**. Instead of the idealized arrangement $5d^16s^2$, the inner 4f shell is filled before the 5d shell since the energy difference between the two states is slight. In general, the RE elements possess the same electronic structure. The ready forms of trivalent ion are also listed in **Table 2.1**. There is an inclination to maintain the half-filled and full-filled subshells due to their unusual stabilities. Therefore, the divalent states in europium and ytterbium are much more stable than the other RE elements, leading to differences between the properties of the hydrides of two elements and those of the other RE hydrides.

The structural properties of the RE elements at ambient condition are presented in **Table 2.2** Crystal Structure of the RE Elements **Table 2.2**. Except for cerium, europium, and ytterbium, all the RE metals possess hexagonal structure. The heavy RE metals Gd, Tb, Dy, Ho, Er, Tm and Lu, as well as Sc and Y, have the close-packed hexagonal structure with a c/a ratio of around 1.58. Compared with the heavy RE metals, the light RE metals lanthanum, praseodymium, neodymium, promethium show a hexagonal structure with stacking sequence ABAC rather than ABAB of the close-packed hexagonal structure. The light RE metals are indexed to possessing double close-packed hexagonal (dhcp) with c/a ratio of ~3.22. Samarium is considered to possess a unique rhombohedral structure (the space group R3m. a = 8.996, $\alpha$= 23 °13') which can also be indexed in the hexagonal system with c/a ratio of 7.25[37].

**Table** 2.2 Crystal Structure of the RE Elements

| Element | Atomic | Crystal Structure | $a_0$ | $c_0$(Å) | $c_0/a_0$ | Ref |
|---|---|---|---|---|---|---|
| Sc | 21 | h.c.p. | 3.309 | 5.273 | 1.59 | [38] |
| Y | 39 | h.c.p. | 3.647 | 5.731 | 1.57 | [38] |
| La | 57 | h.c.p. | 3.772 | 12.144 | 3.22 | [39] |
| Ce (γ) | 58 | f.c.c. | 5.1610 | -- | -- | [39] |
| Ce (β) | | h.c.p | 3.681 | 11.857 | 3.22 | [39] |
| Pr | 59 | h.c.p. | 3.672 | 11.835 | 3.22 | [38] |
| Nd | 60 | h.c.p. | 3.658 | 11.799 | 3.23 | [40] |
| Pm | 61 | h.c.p. | 3.650 | 11.650 | 3.19 | [41] |
| Sm | 62 | rhom.(or h.c.p.) | 3.621 | 26.250 | 7.25 | [37] |
| Eu | 63 | b.c.c | 4.581 | -- | -- | [39] |
| Gd | 64 | h.c.p. | 3.636 | 5.783 | 1.59 | [38] |
| Tb | 65 | h.c.p. | 3.601 | 5.694 | 1.58 | [38] |
| Dy | 66 | h.c.p. | 3.596 | 5.642 | 1.57 | [42] |
| Ho | 67 | h.c.p. | 3.577 | 5.616 | 1.57 | [38] |
| Er | 68 | h.c.p. | 3.559 | 5.587 | 1.57 | [38] |
| Tm | 69 | h.c.p. | 3.538 | 5.555 | 1.57 | [38] |
| Yb | 70 | f.c.c. | 5.486 | -- | -- | [38] |
| Lu | 71 | h.c.p | 3.503 | 5.551 | 1.58 | [38] |

Cerium, unlike the other RE metals, has several allotropic forms. Although it is γ-phase (face-centered cubic, namely fcc) at room temperature ambient pressure, as it cooled below 273K it transforms to β-phase (double close-packed hexagonal, namely dhcp) with c/a ratio of 3.22[43], which is similar to the other light RE metals. It partially transforms to α phase (collapsed fcc) upon further cooling to around 100K[44]. The crystal structures of europium and ytterbium differ from those of the other RE metals resulting from their unusual stable $4f^7$ and $4f^{14}$ electronic structure as discussed above. Europium shows a body-centered cubic (bcc) structure and ytterbium possesses a face-centered cubic structure.

## 2.1.2 The Rare-earth Metal Hydrides

The RE hydrides are discovered accidentally by Winkler[45] in 1891. Cerium metal obtained through the reduction of ceric oxide in a hydrogen atmosphere was found containing considerable amounts of hydrogen. Later, the absorption of appreciable amounts of hydrogen by La, Pr, Nd, and Ce was observed by Matignon[46]. In the next few decades, Muthmann[47], Zhukov[48,49,50], Sieverts[51,52,53] et al made their efforts in observation of the uptake of hydrogen by light RE metals. The $LaH_3$ and $CeH_3$ were reported to be synthesized successfully. However, the similar property of RE metals made it very difficult to separate from one another. Most of the earlier works were done on misch metal, a mixture of the RE metal in varying amounts. The limited purities of the RE metal samples employed in their experiments led to unreliable results on RE-hydrogen systems. Therefore, the work published on supposedly pure RE metals should be examined carefully.

All of the RE metals react directly with hydrogen and form RE dihydride[54]. Additionally, by varying the temperature and hydrogen pressure most of the RE will form trihydrides if the corresponding amount of hydrogen is reachable. Usually, the nonstoichiometric hydrides with $2 \leqslant H/M \leqslant 3$ are formed before the trihydrides formation. In principle, the reaction will proceed at room temperature and low hydrogen pressure (< 1torr) if the metal surface is clean enough[55,56]. Actually, all the reaction can occur at proper temperatures (100-500$^{o}$C) and hydrogen pressure ($\leq$ 1atm ).

According to the crystal structures of the RE hydrides, the RE hydrides has been divided into three groups by Libowitz[57]. Both the dihydrides and trihydrides of the RE metals belonging to the first group possess a face-centered cubic lattice. The light RE metal hydrides, La, Ce, Pr, Nd, are assigned to the first group. The fluorite structure of dihydrides is based on a face-centered cubic lattice with four metal atoms per unit cell located at face-centered cubic positions (0 0 0), (0 1/2 1/2), (1/2 0 1/2), (0 1/2 1/2) and,

hydrogen located at the eight tetrahedral positions. The increase in hydrogen content above $MH_2$ causes the lattice contraction. Contraction has been observed to start at a composition of around $MH_{1.8}$, which indicates that some of the octahedral interstices beginning to be occupied while some of the tetrahedral interstices are still empty. The contraction is supposed to result from the bonding changing accompanied by the occupancies of the octahedral interstices by the extra hydrogen above $MH_2$. The stoichiometric trihydrides of the light RE metals are obtained as all the octahedral interstices are occupied by the hydrogen, exhibiting the $BiF_3$ type structure. The second-group members also have a fluorite-type dihydride structure, while their trihydrides show a hexagonal structure. The heavy RE elements, Gd, Tb, Dy, Ho, Er, Tm, Lu together with Y, Sc belong to this group. The hexagonal structure starts to form when the hydrogen content in hydrides above $MH_{\sim 2.7}$ even though the value may vary for different RE metals. Earlier X-ray diffraction studies on the trihydrides have clarified the trihydrides structure are on the basis of a simple hexagonal close-packed lattice[58]. The hydrogen positions in the hexagonal trihydrides have been identified by the neutron diffraction investigation of $HoD_3$ by Mansmann and Wallace[59] in 1964. In fact, $a_0$ parameter in the actual structure is $\sqrt{3}$ times that of the hcp cell determined by X-ray study. The deuterium atoms are located at tetrahedral and octahedral interstices with slight deviations from the ideal positions for offering enough space for the deuterium atoms. The other RE trihydrides in this group are assumed to possess isostructure as $HoD_3$ with slightly different structural parameters[59]. The third group contains only europium and ytterbium hydrides, whose dihydrides exhibit an orthorhombic structure resembling the alkaline earth hydrides. The trihydride of ytterbium is face-centered cubic with $BiF_3$ structure. While the trihydride of europium failed to form although lots of efforts have been made. The special properties of the two elements are attributed to the unusual stability of the fully-occupied 4f state in the case of ytterbium and exactly half-occupied 4f state in the case of europium. The crystal structures and metal lattice

parameters of the RE dihydrides and trihydrides at ambient condition are listed in **Table 2.3**.

**Table** 2.3 Crystal Structure of the RE Hydrides[60]

| Element | Dihydride | | Ref. | Trihydride | | Ref. |
|---|---|---|---|---|---|---|
| | Structure | Parameters(Å) | | Structure | Parameters(Å) | |
| Sc | f.c.c. | a =4.783 | [61] | f.c.c. | a=3.380, c=6.135 | [62] |
| Y | f.c.c. | a=5.205 | [58] | h.c.p. | a=3.672, c=6.659 | [58] |
| La | f.c.c. | a=5.663 | [63] | f.c.c. | a=5.604 | [63] |
| Ce | f.c.c. | a=5.580 | [64] | f.c.c. | a=5.539 | [61] |
| Pr | f.c.c. | a=5.515 | [64] | f.c.c. | a=5.486 | [64] |
| Nd | f.c.c. | a=5.469 | [64] | f.c.c. | a=5.42 | [64] |
| Sm | f.c.c. | a=5.363 | [65] | h.c.p. | a=3.782, c=6.799 | [58] |
| Eu | orthorhombic | a=6.254, b=3.806, c=7.212 | [65] | -- | | |
| Gd | f.c.c. | a=5.303 | [66] | h.c.p. | a=3.76, c=6.705 | [67] |
| Tb | f.c.c. | a =5.246 | [58] | h.c.p. | a=3.700, c=6.658 | [58] |
| Dy | f.c.c. | a =5.201 | [58] | h.c.p. | a=3.671, c=6.615 | [58] |
| Ho | f.c.c. | a =5.165 | [58] | h.c.p. | a=3.642, c=6.560 | [58] |
| Er | f.c.c. | a =5.123 | [58] | h.c.p. | a=3.621, c=6.526 | [58] |
| Tm | f.c.c. | a =5.090 | [58] | h.c.p. | a=3.599, c=6.489 | [58] |
| Yb | orthorhombic | a= 5.889, b= 3.576, c = 6.789 | [65] | f.c.c.($YbH_{2.55}$) | a=5.178 | [62] |
| | | | | $YbH_{2.96}$ | -- | [68] |
| Lu | f.c.c . | a =5.033 | [58] | h.c.p | a=3.558, c=6.443 | [58] |

Since the first observation of the "switching" of electrical and optical properties of REHx during the process of hydrogen adsorption and desorption in yttrium (Y) and Lanthanum (La)[69], many efforts have been made to investigate the reversible electrical and optical properties later on by physicians and chemists[70]. In their experiment, the thin films of hydrides show the spectacular changes from light reflecting to transmitting with the changes in hydrogen concentration in the hydrides. This "switchable mirrors" phenomenon caused by the reversible metal-insulator transition, is considered to have a

promising application in the electronics industry. The possibility of the structural and metal-to-insulator transitions induced by pressure was first reported by Russian researchers on samarium and gadolinium trihydrides about forty years ago[71]. This triggers many experimentalists to study their properties under high pressure. Some research has already been performed in that direction[72,73,33].

The interest in the high-pressure behaviors of RE trihydrides was renewed after the experimental observation of the hcp to fcc phase transition of $ErH_3$ under high pressure in 2004 [74]. Later on in the period from 2005 to 2007, Palasyuk and Tkacz[75,76,77,78,8,79,80] reported on the similar phase transitions from hexagonal to cubic in the series of lanthanide hydrides ($SmH_3$, $GdH_3$, $HoH_3$, $LuH_3$) and $YH_3$ under high pressure using the energy dispersive X-ray diffraction method in a DAC, and predicted the similar behaviors for $TbH_3$ and $DyH_3$. Recently X-ray, Raman and theoretical studies of terbium trihydrides under pressure have been published[7]. The $YH_3$ is investigated by synchrotron X-ray diffraction, Raman scattering and infrared spectroscopy by Kume et al[81]. They reported that $YH_3$ presented metal lattice change under high pressure from initial hcp to fcc phase through an intermediate phase. In Palasyuk's report, the intermediate phase was not observed due to the limited resolution of the EDXRD. While the phase transition under high pressure of the heavy $REH_3$ observed all are appeared to be sluggish. The pressure gap between two phases is always fairly obvious. It is worth noting that the hcp-to-fcc phase transition pressure of $REH_3$ mentioned later in this thesis are the pressure when the phase transition begins to occur, namely the transition pressure of initial hcp-to-intermediate phase. The transition pressures of $REH_3$ reveal a quite well linear dependence both on the atomic number of forming RE metals and on the molar volume of initial hcp phase at ambient condition. $ScH_3$ was studied by Raman scattering, infrared spectroscopy, and visible absorption spectroscopy[82] under high pressure. It is worth mentioning that the claimed phase transition pressure ~25 GPa contradicted the predicted value 19 GPa based on the linear dependence of transition pressure on molar volume of

initial hcp phase at ambient condition. However, there is no Raman spectrum collected between 20 GPa and 25 GPa. We can roughly conclude the new phase starts to form between 20 GPa and 25 GPa. To some degree, the predicted value of ~19 GPa was thought to be reasonable even the X-ray diffraction measurement is expected.

Unlike most trihydrides of heavy RE displaying a change in the metal lattice from hcp to fcc during compression at room temperature, the trihydrides of light RE (La, Ce, Pr, Nd, Pm) remain the fcc metal lattice under pressure up to ~30 GPa. Since europium trihydride does not exist and ytterbium trihydride possesses unknown structure even at ambient condition, there is no information of their phase transition under pressure. Hence, dysprosium trihydride is the last one in the line to wait for the investigation.

The value of transition pressure of $DyH_3$ was predicted around 7 GPa as shown in **Fig.** 2.1 and Fig.2.2. based on the linear dependence of transition pressure both on forming RE atomic number and the molar volume of initial hcp phase at ambient condition[8]. In order to verify the prediction, the $DyH_3$ was investigated carefully by synchrotron X-ray diffraction in DAC under pressure in the range up to 40 GPa. Additionally, the Raman scattering of both $DyH_3$ and $DyD_3$ were obtained for elaborative investigation of the intermediate phase and isotope effect.

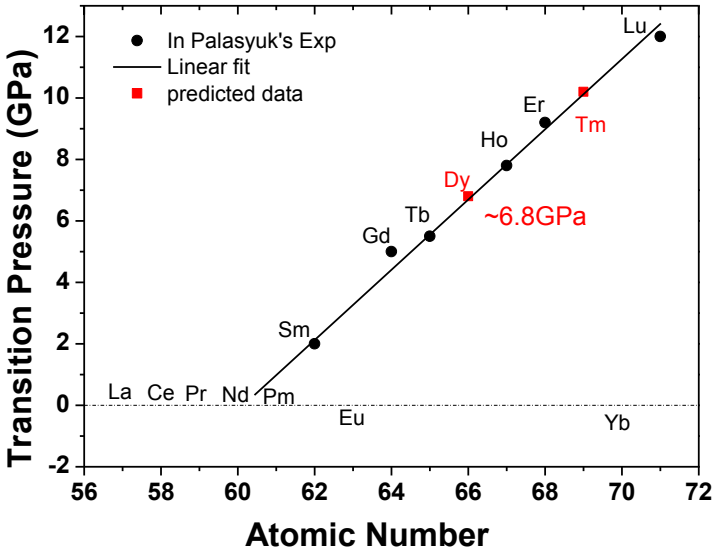


**Fig.** 2.1 The transition pressures of RE trihydrides varies with the forming RE atomic number. The experimental data for other $REH_3$ are cited from Palasyuk's publications[8,7].

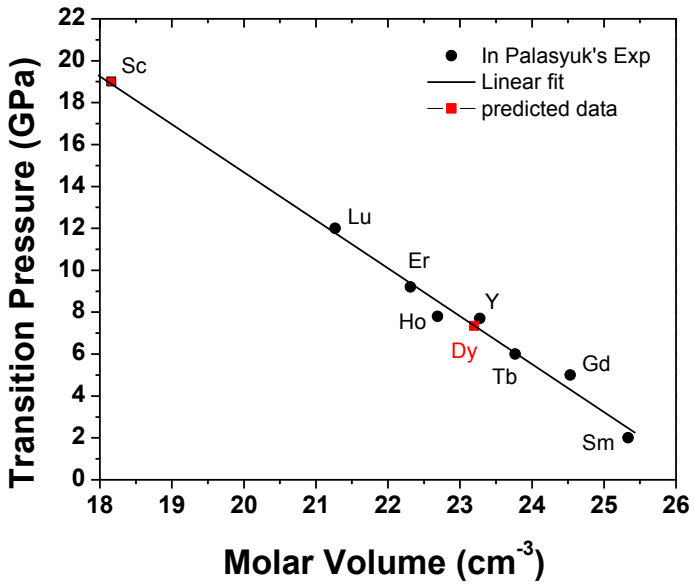


**Fig.** 2.2 The transition pressures of RE trihydrides varies with the molar volume of the initial hcp phase at ambient conditions. The experimental data for other $REH_3$ are cited from Palasyuk's publications[8,7].

# 2.2 Study on $DyH_3$ and $DyD_3$[83]

## 2.2.1 X-ray diffraction analysis of $DyH_3$ under pressure

Samples of dysprosium trihydride were obtained from nominally 99.9% pure dysprosium by direct absorption under the gaseous hydrogen and deuterium pressure of 15.0 MPa and 300 ℃ during four hours in a high-pressure Sievert apparatus as described earlier[74]. The purity and predicted structure of the samples used in high-pressure studies have been confirmed by powder X-ray diffraction and elemental analysis.

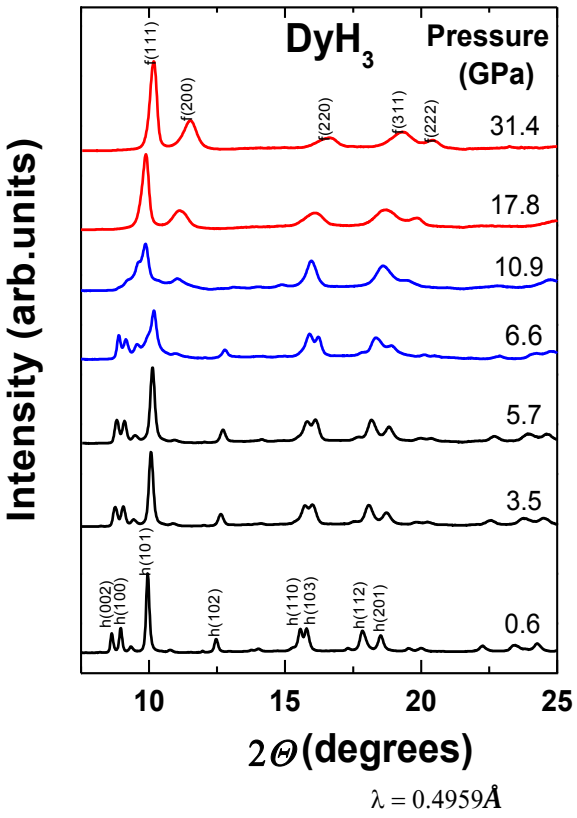


**Fig.** 2.3 X-ray spectra of $DyH_3$ for the selected pressures taken at room temperature.

Synchrotron radiation and diamond anvil cell have been used for the high-pressure X-ray diffraction structural study. The high-pressure X-ray diffraction studies were conducted at Cornell High Energy Synchrotron Source (CHESS) with the X-ray wavelength of 0.04959 nm. Mao-Bell type DAC[84] with diamond anvils of a culet size 400 μm were used for pressure generation. Samples were loaded into a 150 μm hole in the stainless steel gasket (TS302) pre-indented to a thickness of ~50 μm, along with a small ruby chip at the center of the sample. The pressures were then calculated using the ruby ($R_1$) fluorescence method. The pressure transmitting medium used in the experiment was silicone oil (Sigma–Aldrich) of viscosity 1000 cP. The 2D diffraction patterns obtained were integrated using Fit2D software[85].

**Fig.** 2.3 shows the selected spectra of dysprosium trihydride under pressure taken in diamond anvil cell. The initial spectrum taken at 0.6 GPa (black) is indexed as hexagonal phase and the highest spectrum indexed as cubic phase (red) was taken at pressure over 31 GPa. Spectra (blue) taken in the intermediate region between 5.7 and 17.8 GPa represent complex structure. Small peaks visible in the spectrum were identified as the admixture of $Dy_2O_3$ that apparently appeared during the loading procedure.

The molar volume of dysprosium trihydride determined from X-ray analysis for both hexagonal and cubic phase was used for determination of the corresponding equation of state. Similar as in the other trihydrides previously studied[7,8,74-79,81,82], dysprosium trihydride undergoes a structural phase transition from the initial hexagonal to a cubic structure. We estimated from the XRD patterns taken during pressure increase that at the pressure of about 7 GPa transformation starts and reflections from the initial hexagonal phase gradually disappear while the peaks corresponding to cubic phase are growing in intensity. The transition is completed at the pressure above 17 GPa. As the pressure decreased a large hysteresis was noticed and a significant amount of the cubic phase was observed after releasing the pressure to ambient conditions. Analyzing the X-ray spectra taken on dysprosium trihydride and previously obtained for another RE trihydrides we

have noticed that the cubic phase is to some extent distorted. This will be discussed in the next section devoted to Raman scattering measurements.

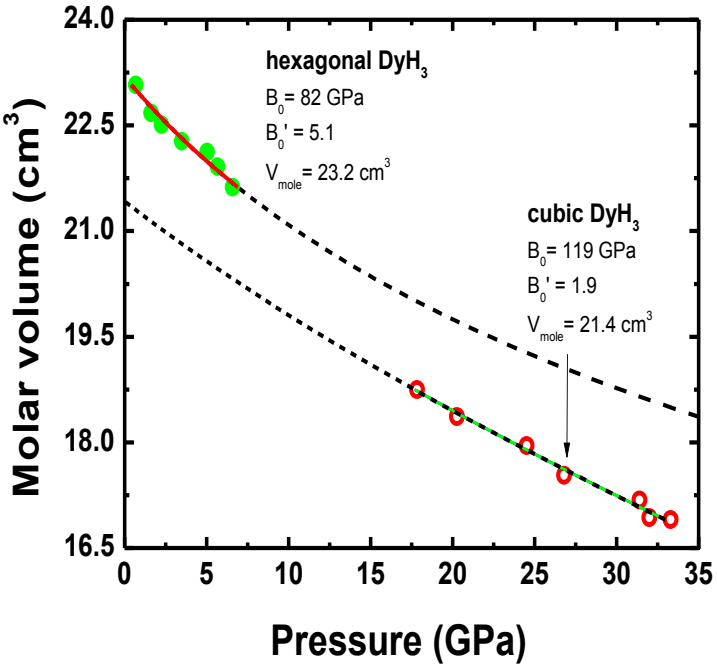


**Fig.** 2.4. Volumes of both phases of dysprosium trihydride as function of pressure together with the fit to Murnaghan equation of state. Solid lines correspond to region of experimental fit to the equation of states. Doted lines indicate the extrapolation of equation of states.

Compressibility parameters are evaluated by fitting the Murnaghan equation of state (1.23) shown below:

$$P(V) = \frac{B}{B'}\left[\left(\frac{V_0}{V}\right)^{B'} - 1\right] \qquad (1.23)$$

where B denotes bulk modulus, $B_0'$ represents the first derivative of B against pressure, $V_0$ and V signify initial and current volume respectively. The molar volumes as a function of pressure for both phases are presented in **Fig.** 2.4.

**Table** 2.4 Structural parameters and parameters of Equation of State (EOS) of the dysprosium metal and nearest neighbors in periodic table along with their trihydrides.

| **Sample** | | **Lattice parameters at amb. pressure** | | **Molar Volume $cm^3/mol$** | **hcp-fcc transition pressure (GPa)** | **EOS parameters** | | **References** |
|---|---|---|---|---|---|---|---|---|
| | | **a (Å)** | **c (Å)** | | | **B (GPa)** | **B'** | |
| Tb | hcp | 3.61 | 5.69 | 19.24 | | 40 | 3.2 | Ref. [86] |
| $TbH_3$ | hcp | 3.69 | 6.65 | 23.9 | 5.5(9.3)* | 81 | 4.0 | Ref. [7] |
| | fcc | 5.33 | | 22.9 | | 96 | 4.0 | |
| Dy | hcp | 3.59 | 5.64 | 19.97 | | 41 | 3,2 | Ref. [86] |
| **$DyH_3$** | **hcp** | **3.66** | **6.64** | **23.2** | **7.0(10.)*** | **82** | **5.1** | This work |
| | **fcc** | **5.23** | | **21.4** | | **119** | **1.9** | |
| Ho | hcp | 3.577 | 5.61 | 18.7 | | 42 | 2.9 | Ref. [86] |
| $HoH_3$ | hcp | 3.64 | 6.69 | 22.7 | 7.8(12)* | 87 | 4 | Ref. [75] |
| | fcc | 5.25 | | 21.8 | | 90 | fixed | |
| Er | hcp | 3.55 | 5.58 | 18.4 | | 44 | 2.9 | Ref. [86] |
| $ErH_3$ | hcp | 3.62 | 6.53 | 22.3 | 9.2 (14)* | 70 | 4 | Ref. [74] |
| | fcc | 5.23 | | 21.5 | | 81 | fixed | |

* [87]

The structural parameters of the dysprosium metal and its nearest neighbors in the periodic table along with their trihydrides are listed in **Table 2.4**. Theoretical transition pressures calculated by Bo et al.[87] significantly exceed that from experimental results, which is supposedly caused by their calculations correspond to 0 Kelvin temperature as always in this type of theoretical approaches rather than room temperature at which the experiments are done. Our experimental results from both Raman and X-ray measurements show a value less than that namely about 7.0 GPa for both hydride and deuteride.

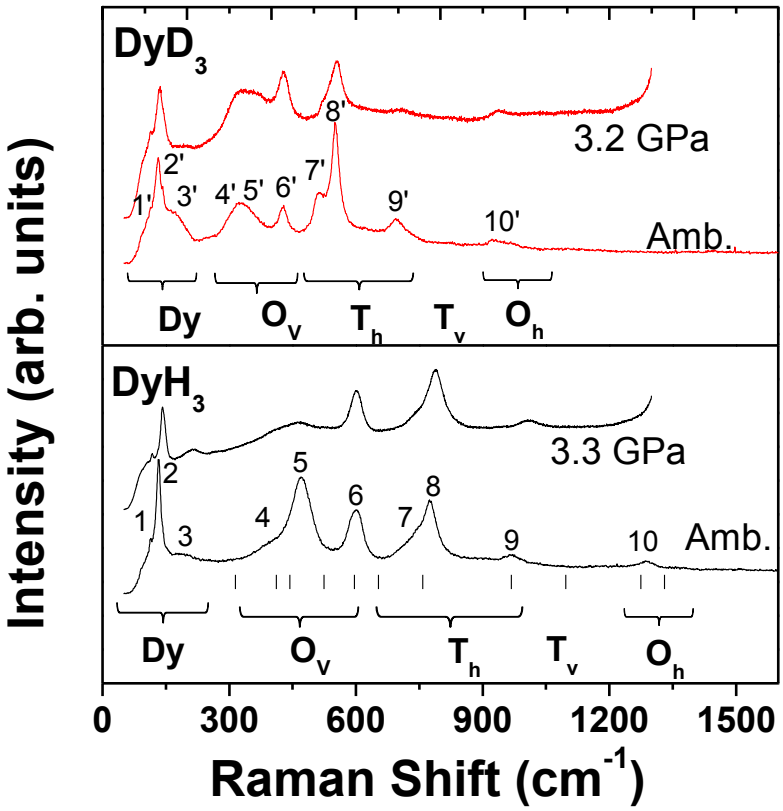


**Fig.** 2.5 Raman spectra of the sample $DyH_3$ and $DyD_3$. The top panel shows Raman spectra of $DyD_3$ at ambient condition and 3.3 GPa, respectively. The bottom panel shows Raman spectra of $DyH_3$ at ambient condition and 3.2 GPa, respectively. $O_v$ ($O_h$) indicates that H at the octahedron sites vibrates vertically (horizontally) to the c plane, and the $T_v$ ($T_h$) indicates that H at the tetrahedron sites vibrate vertically (horizontally) to the c plane.

## 2.2.2 Raman scattering of $DyH_3$ and $DyD_3$ under pressure

Raman spectra were collected in backscattered geometry using custom designed setup for micro-Raman measurements based on monochromator Jobin Yvon THR1000 equipped with a single grating (with 1200 grooves $mm^{-1}$) giving a resolution of ~1 $cm^{-1}$, notch filters (Keiser Optical Systems) and thermoelectrically cooled (-65 ℃) (Peltier effect) CCD (Horiba Synapse) detection. He-Ne laser (Melles-Griot) line 632.8 nm was used for sample excitation. An example of Raman spectra of both $DyH_3$ and $DyD_3$ recorded at ambient and

under high pressure are presented in **Fig.** 2.5. As always strong Raman signal of diamond at 1331 $cm^{-1}$ limits the region of data collection. Data at ambient pressure were recorded outside of DAC. The modes including acoustic and optical ones have been detected at ambient pressure for both hydride and deuteride samples as presented in **Fig.** 2.5.

The three peaks labeled 1-3 located lower than 250 $cm^{-1}$ have been assigned to metal dysprosium vibrations, resulting from the same locations in both the $DyH_3$ and $DyD_3$. The lines above 400 $cm^{-1}$ were assigned to hydrogen-related vibrations, arising from the isotope shift by approximately $\sqrt{2}$ when the hydrogen is replaced by deuterium. Additionally, the H-related modes were assigned by following the assignments for phonon density of state (PDOS) peaks measured by neutron inelastic scattering[88].

Evolutions of Raman spectra as a function of pressure for both acoustic and optical modes are presented in **Fig. 2.6** and **Fig. 2.7** for the trihydride and trideuteride of dysprosium, respectively. The appearance of the spectra dramatically changes as the pressure higher than 7 GPa, which indicates the initiation of the phase transition. At the pressure of ~25 GPa, the absences of the strongest Raman modes around 850 $cm^{-1}$ for $DyH_3$ and 600 $cm^{-1}$ for $DyD_3$ imply the completion of the hcp-to-fcc phase transition.

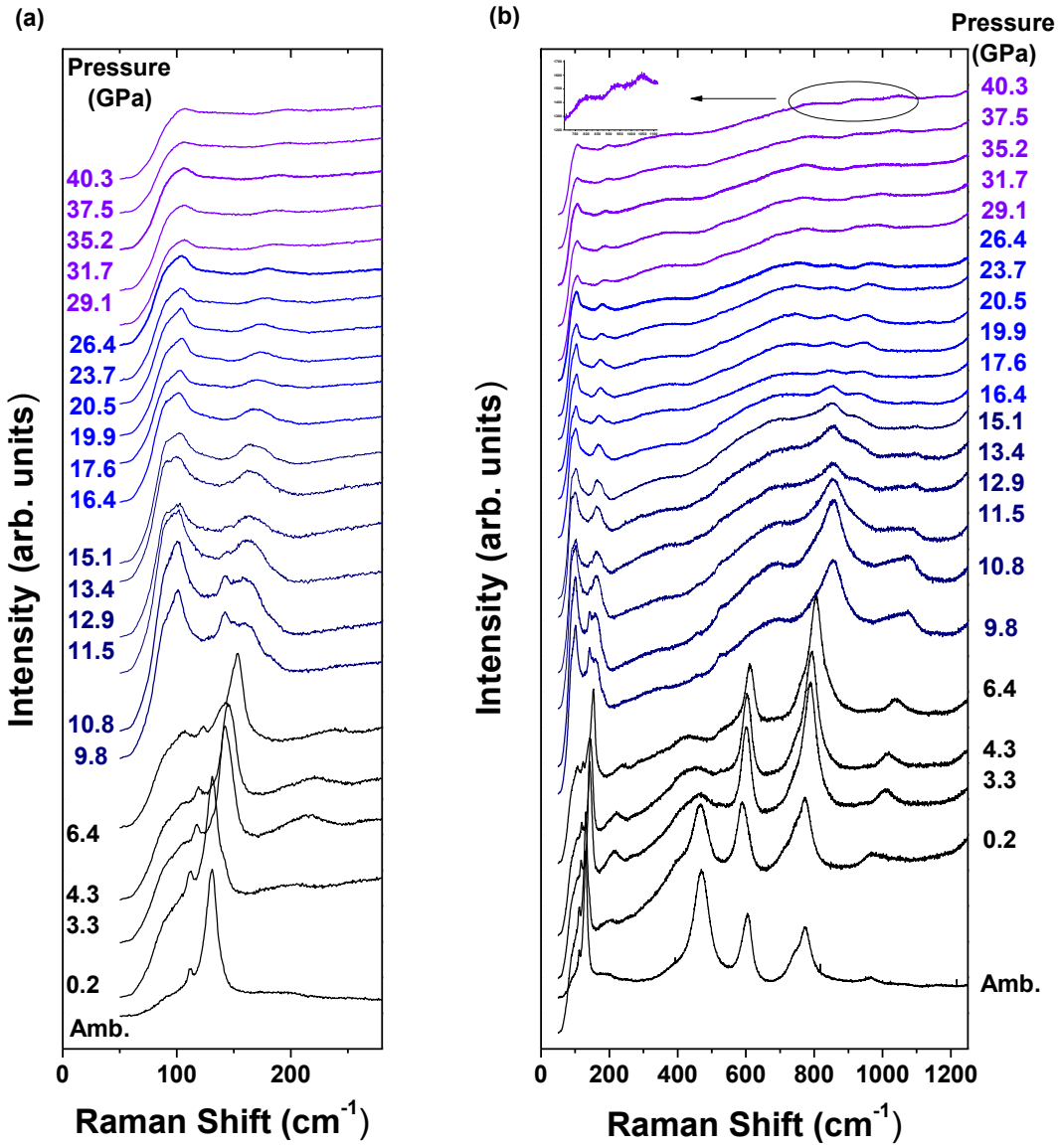


**Fig. 2.6** Raman spectra of $DyH_3$ during compression. (a) and (b) shows the low frequency region (0-280 $cm^{-1}$) and whole of spectra (0-1250 $cm^{-1}$), respectively.

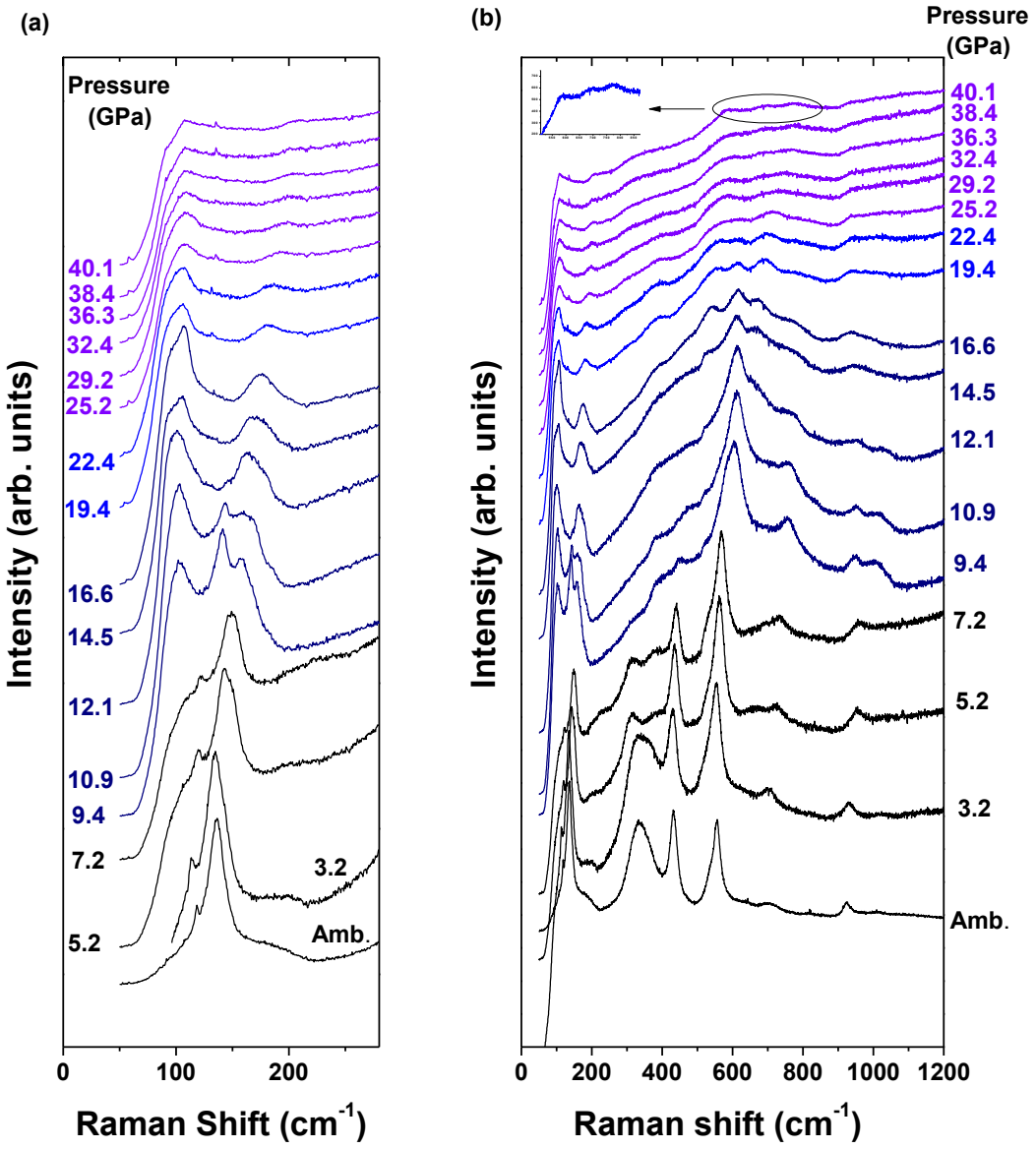


**Fig. 2.7** Raman spectra of $DyD_3$ during compression. (a) and (b) shows the low frequency region (0-280 $cm^{-1}$) and whole of spectra (0-1250 $cm^{-1}$), respectively.

General overall pictures of the pressure dependence of Raman modes for the dysprosium hydride and deuteride are quite similar to those of yttrium hydride and deuteride. It is not a surprise as both systems have the same crystal structure and they are only different in lattice parameters and energy gap. The same scheme of evolution of structural changes is observed for both hydride and deuteride with only difference in pressure values of the corresponding regions of coexistence of certain phases. Structural changes manifested by disappearance and formation of new modes were used for the constructing diagram of the

pressure induced phase transformation. These diagrams are presented in **Fig. 2.8** (a) and (b)

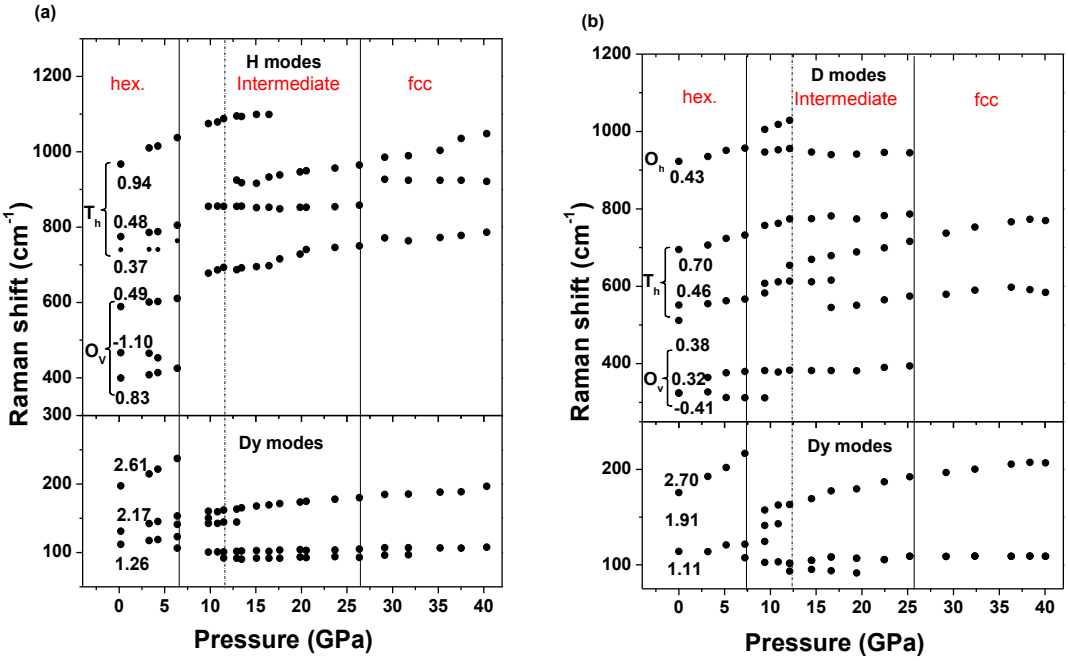


**Fig. 2.8** Pressure dependence of Raman frequencies of (a) $DyH_3$ and (b) $DyD_3$ during compression. For hexagonal phase, the Grüneisen parameters of different modes are labeled in the figure. $O_v$ ($O_h$) indicates that H at the octahedron sites vibrates vertically (horizontally) to the c plane, and the $T_v$ ($T_h$) indicates that H at the tetrahedron sites vibrate vertically (horizontally) to the c plane.

Although the factor group analysis predicts for the fcc phase only one mode we observed for both compounds under investigation evolution of three modes up to the highest pressure reached. It was postulated[82] that the local structure distortion can allow the mode being observed even though the mode is forbidden by the symmetry of the average crystal structure.

Substitution of hydrogen by deuterium is a common method to determine whether particular modes are connected with the hydrogen vibrations since such a replacement shifts peak position by a factor which is proportional to the square root of reduced mass. These modes are definitely related to the vibrations of hydrogen species in dysprosium lattice as all of them display characteristic isotope effect besides deviation from the harmonic value of $\sqrt{2}$.

From our X-ray diffraction studies performed on almost all RE trihydrides, distortion of the fcc phase seems to be evident. For the ideal fcc, phase one can expect the value of distance $d_{111}/d_{200}$ to be around 0.866. Instead, the value of 0.89 remains constant in the whole fcc stability region. Moreover, quite reliable measurements by Boroch[89] for $LaH_3$ (also similar fcc structure), have shown that powder diffraction pattern contains many more lines than it is expected for the cubic structure, in fact, nine extra lines (in addition to the cubic ones) were observed. If we assume that there is another phase then additional questions arise about the phase diagram of the system as the hydrogen-rich phase diagram cannot end with the two-phase region. It is possible that this second phase is a crystallographic modification of the known cubic phase, and it is stable under specific p, T conditions.

## A Mode Grüneisen parameters

Determination of the mode Grüneissen parameter provides a qualitative measure of anharmonicity in certain crystals and is crucial to a detailed understanding of different physical properties and character of interatomic forces.

Mode Grüneisen parameter is defined at constant T as

$$\gamma_i = \frac{B_0}{\nu_i}\left(\frac{\partial_{\nu_i}}{\partial P}\right)_T$$

where B – describes bulk modulus, $\nu_i$ - Raman frequencis of $i_{th}$ mode and P stands for pressure.

Assuming the same bulk modulus for the dysprosium deuteride as for hydride makes it possible to compare mode Gruneissen parameters for both compounds.

As can be seen in **Fig. 2.8** (a) and (b), mode Grüneisen parameters for the modes related to the tetrahedral occupations are bigger than that for the octahedral sites for both hydride and deuteride samples. This could indicate that the interactions of the species located in the

tetrahedral sites to the bigger extent alternate harmonicity of corresponding modes as compared to octahedral occupations.

## B Isotope effect

**Fig.** 2.5 shows the isotope shift of the vibrational energies for dysprosium hydride and deuteride at low pressure. The ratio between the energies of H and D vibrational peaks for the initial samples at normal pressure and at the region of stability of hexagonal phase is almost equal harmonic value i.e. around 1.41 for the all peaks including acoustic ones. It could indicate a rather small anharmonicity in the hydrogen potential independent on the symmetry of occupancy site in the hexagonal phase. However, the significant deviation from harmonic value is observed for the high-pressure cubic phase. This ratio reaches a value of about 1.35 which can indicate significant changes of anharmonicity of hydrogen potentials after structural rearrangements due to phase transformation.

**Table 2.5** presents the ratios of the hydrogen over deuterium modes in hexagonal and cubic phases of both compounds. Similar deviation (1.35) from harmonic value has been detected for cerium dihydride[90].

**Table** 2.5 Isotope effect in both the low-pressure hcp phase and high-pressure fcc phase

| | | **hcp phase** | | | **fcc phase** | |
|---|---|---|---|---|---|---|
| | **[1]Raman** | **Amb.** | **6.4 GPa** | **[2]Raman** | **29.2 GPa** | **40.0 GPa** |
| $(\omega_H/\omega_D)_{opt}$ | 466 | 1.40 | 1.35 | 770 | 1.33 | 1.35 |
| | 589 | 1.40 | 1.39 | 928 | 1.35 | 1.34 |
| | 775 | 1.40 | 1.41 | 985 | 1.34 | 1.36 |
| | 967 | 1.39 | 1.41 | | | |

1 The Raman modes are obtained at ambient pressure for hcp phase,

2 The Raman modes are collected at 29.2 GPa for fcc phase

## 2.3 Raman Investigation of $LaH_3$ and $LaD_3$[91]

Three weak and broad modes at the highest pressure reached for the high-pressure fcc phase of $DyH_3$ and $DyD_3$ were observed. This contracts with the factor group analysis prediction. $DyH_3$ and $DyD_3$, like the other heavy RE trihydrides, possess an fcc phase at high pressure. The high-pressure fcc phase for heavy RE trihydrides is supposed as the same as the low-pressure fcc phase for light RE trihydrides. Thus, the Raman scattering of light RE trihydrides at low pressure is suggested to be a solution to test whether the three weak and board modes actually originating from the fcc phase. In this work, lanthanum trihydride as the typical light RE trihydride is chosen for Raman investigation.

### 2.3.1 Sample and synthesis

Samples of trihydrides and lanthanum deuteride, gadolinium and erbium trhydides were obtained from nominally 99.9% pure metals by direct absorption under the gaseous hydrogen and deuterium pressure of 15.0 MPa and 300 ℃ during four hours in a high-pressure Sieverts apparatus as described earlier[74]. The purity and predicted structure of the samples used for high-pressure studies have been confirmed by powder X-ray diffraction and elemental analysis before loading in DAC.

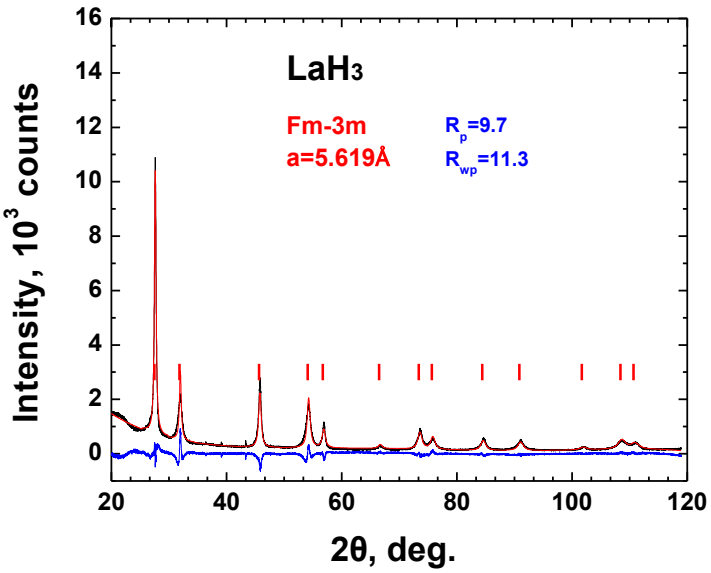


**Fig. 2.9** XRD pattern of the initial $LaH_3$ sample (black), its Rietveld fit (red) and fit residue (blue). Ambient conditions, CuKα radiation.

Initial sample has been analyzed using X-ray diffraction method while composition has been determined by weighting sample of about 1.5 g before and after charging it with hydrogen. Value of 3.00±0.03 in atomic ratio H/La has been obtained. X-ray diffractogram of lanthanum trihydride is shown in **Fig. 2.9**. Similar pattern was obtained for lanthanum deuteride. According to Klavins et al.[92] lattice parameter determined in our measurements as equal 5.619 Å corresponds to stoichiometric trihydride of lanthanum.

Measurements of lanthanum trihydride were done in paraffin oil which served both as a pressure medium and protection against oxidation. Lanthanum trihydride is most sensitive to oxygen and moisture among the RE trihydrides family.

## 2.3.2 Raman studies of $LaH_3$ and $LaD_3$ at ambient pressure

The modes including acoustic and optical ones have been detected at ambient pressure for hydride and deuteride samples and are presented in **Fig. 2.10**. Whether or not these additional modes are hydrogen related we performed substitution of hydrogen by deuterium. Such a replacement should result in the shift of corresponding modes by

quasi-harmonic factor of $\sqrt{2}$. All modes were identified as being hydrogen related as isotope effect shows value of 1.41 for optical part of spectrum as presented in **Table 2.6**.

Modes coming from possible surface contamination presumably by oxide layer should not display isotope effect. Data at ambient pressure were recorded outside of DAC.

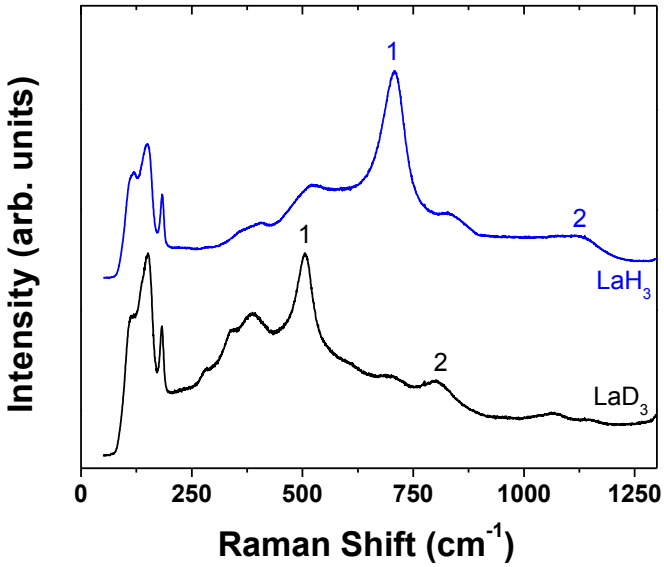


**Fig. 2.10** Raman Spectra of $LaH_3$ and $LaD_3$ at ambient condition.

**Table** 2.6 Isotope effect of $LaH_3$ and $LaD_3$ at ambient condition.

| | $\omega_{LaH3}$ | $\omega_{LaD3}$ | $\omega_{LaH3}/\omega_{LaD3}$ |
|---|---|---|---|
| Lattice modes | 183.2 | 182.0 | 1.00623 |
| | 111.5 | 111.3 | 1.0018 |
| | 150.1 | 150.4 | 1.00155 |
| H modes | 704.7 | 500.6 | 1.41 |
| | 1128.8 | 800 | 1.41 |

**Fig. 2.10** shows the spectra of $LaH_3$ and $LaD_3$ recorded at ambient condition. The modes below 250 $cm^{-1}$ were caused by the metal lattice vibrations due to the same locations in both hydride and deuteride. Specifically, the Raman modes which are labeled as 1 and 2 were attested to possessing the isotope shift by approximately $\sqrt{2}$. Since the Raman

modes above 250 $cm^{-1}$ of $LaH_3$ presents the similar shape to that of $LaD_3$ and two modes possess the isotope shifts, the lines above 250 $cm^{-1}$ were confirmed to originate from hydrogen related vibrations. It is worth noting that the $BiF_3$- type structure ought to possess only one active Raman mode predicted by the factor group analysis. In the cases of $LaH_3$ and $LaD_3$, many peaks are shown in the Raman spectra even though the peaks are considerably broadened due to the combination of several modes.

## 2.3.3 Raman studies of $LaH_3$ and $LaD_3$ at high pressure

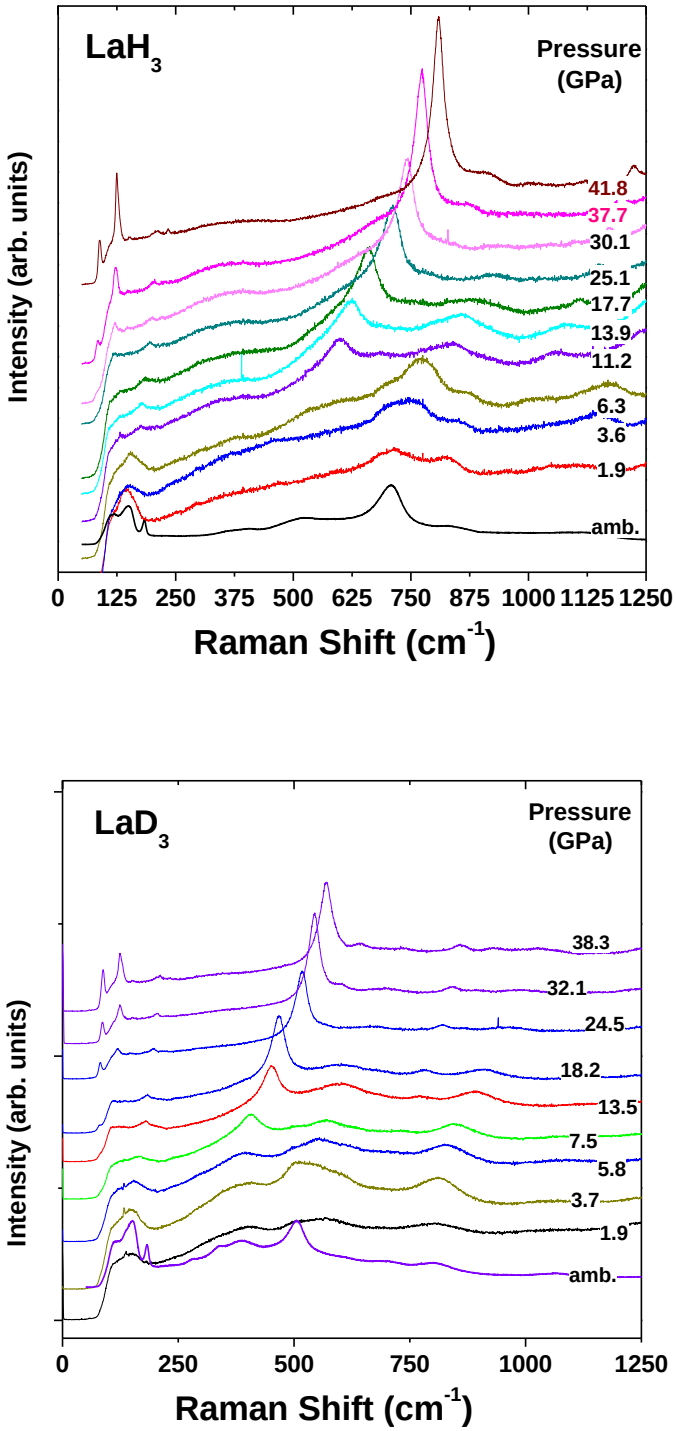


**Fig. 2.11** Raman Spectra of (a) $LaH_3$ and (b) $LaD_3$ at selected pressure during compression

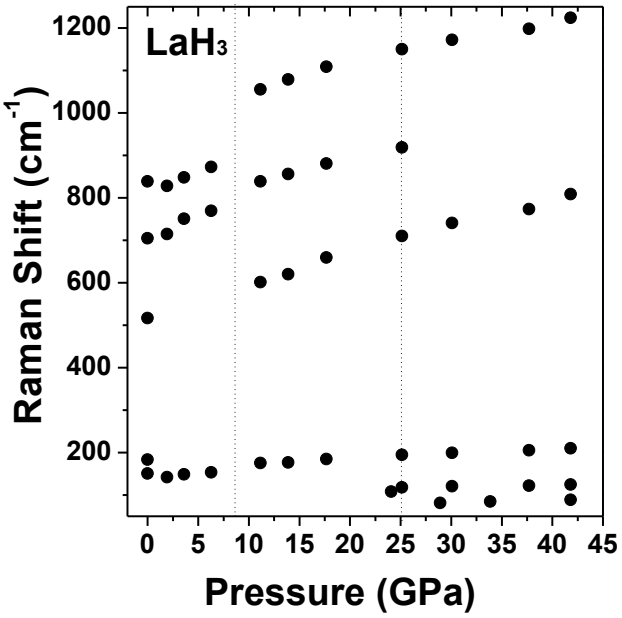


**Fig. 2.12** Pressure dependence of Raman frequencies of $LaH_3$ during compression.

Raman spectra of both $LaH_3$ and $LaD_3$ recorded under high pressure are presented in **Fig. 2.11**. As always strong Raman signal of diamond at 1331 $cm^{-1}$ limits the region of data collection. Phase transition connected with the hydrogen ordering similar to the low temperature phase transition reported in[93] is observed at pressure range from 6 to 11 GPa. This is clearly seen in Raman spectra evolution and from the shift of selected Raman modes as function of pressure as presented in **Fig. 2.11** and **Fig. 2.12**, respectively. It should be pointed out that the earlier high-pressure X-ray study on stoichiometric lanthanum trihydride[94] performed up to 25 GPa did not revealed any structural phase transition. Since the composition of both compounds have been determined as very close to stoichiometry the known tetragonal distortion notice at low temperature and high pressure should also be excluded as this transformation is restricted to the hydrogen concentration range from 2.65 to 2.90 in atomic ratio[92]. So the observed transition must originate from the hydrogen particles ordering rather than from the lattice rearrangement. High pressure Raman measurements on lanthanum trihydride and deuteride have shown pressure induced phase transition at pressure range from 6 to 11 GPa. This transition can be compared to the similar phase transition observed in low temperature region by heat capacity, neutron and

X-ray diffraction measurements performed on stoichiometric lanthanum trihydride and trideuteride. We suggest that this transition could be similar to that observed in the heat capacity measurements at low temperature [95]. The superstructure lines in the neutron diffraction pattern and X-ray measurements of stoichiometric $LaD_3$ has been reported also by Udovic et al. [96], [97] for stoichiometric lanthanum trideuteride at temperature about 260 K. These results suggest the appearance of a low temperature phase transformation presumably of the second type of order which was interpreted as due to an ordering of the D atoms on off-centre positions in the octahedral interstices of the metal atom network. It was also postulating that a long-range-ordered pattern of displacements of the La metal atoms from the ideal fcc symmetry was occurring in addition to long-range-ordered displacements within the D sublattices.

# Chapter 3. **Transition Metal Hydrides**

## 3.1 Literature Review

### 3.1.1 Transition Metals

TMs are defined as a set of elements whose atom has a partially filled d sub-shell, or which can give rise to cations with an incompleted sub-shell by the IUPAC[98]. In general, elements from groups 3 to 12 on the periodic table[99,100] are included in TMs. In actual practice, the f-block lanthanide and actinide series are also considered as TMs and are called "inner transition metals". In this thesis, the lanthanide together with scandium and yttrium is defined as RE metals and has been described in Chapter 2 in detail.

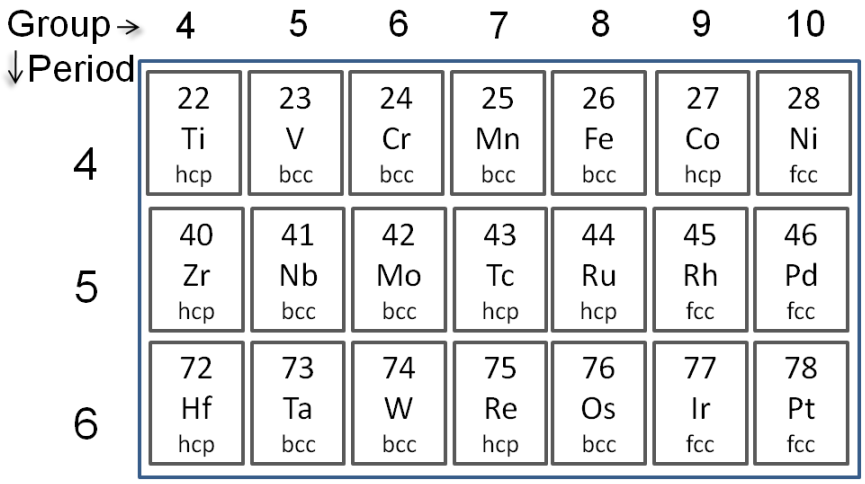


**Fig.** 3.1 Scheme of the crystal structures of TMs at ambient conditions

The crystal structure of TMs from Group 4 to 10 are listed as the same positions in the periodic table in **Fig.** 3.1. The crystal structure together with lattice parameters of TMs from Group 4 and 5 are listed in details in **Table 3.1**. The Ti, Zr and Hf elements from Group 4 possess close-packed hexagonal structure at ambient conditions. The V, Nb and

Ta elements exhibit body-centered cubic structure. The structural information of TMs from Group 6 to 10 are presented in **Table 3.2**. As seen in **Table 3.1** and **Table 3.2**, the TMs possess three kinds of structure, namely hcp, bcc, fcc. The c/a ratios of hcp structural TMs are located in the range of 1.58-1.62, which are close to the value of 1.58 for most heavy RE metals.

**Table** 3.1 Crystal structures of TMs from Group 4 and 5 at ambient condition

| Element | Atomic | Crystal Structure | $a_0$(Å) | $c_0$(Å) | $c_0/a_0$ | Ref |
|---|---|---|---|---|---|---|
| Ti | 22 | h.c.p. | 2.9508 | 4.6855 | 1.59 | [101] |
| Zr | 40 | h.c.p. | 3.232 | 5.147 | 1.59 | [102] |
| Hf | 72 | h.c.p. | 3.1964 | 5.0511 | 1.58 | [103] |
| V | 23 | b.c.c. | 3.03 | | | [104] |
| Nb | 41 | b.c.c. | 3.3004 | | | [105] |
| Ta | 73 | b.c.c. | 3.3013 | | | [106] |

**Table** 3.2 Crystal structures of TMs from Group 6 and 10 at ambient condition

| Element | Atomic | Crystal Structure | $a_0$(Å) | $c_0$(Å) | $c_0/a_0$ | Ref |
|---|---|---|---|---|---|---|
| Cr | 24 | b.c.c. | 2.91 | | | [107] |
| Mo | 42 | b.c.c. | 3.147 | | | [107] |
| W | 74 | b.c.c. | 3.1652 | | | [106] |
| Mn | 25 | b.c.c. | 8.9125 | | | [108] |
| Tc | 43 | h.c.p. | 2.735 | 4.388 | 1.60 | [109] |
| Re | 75 | h.c.p. | 2.761 | 4.456 | 1.61 | [110] |
| Fe | 26 | b.c.c. | 2.8665 | | | [111] |
| Ru | 44 | h.c.p. | 2.7059 | 4.2815 | 1.58 | [112] |
| Os | 76 | b.c.c. | 2.7344 | 4.3173 | 1.58 | [112] |
| Co | 27 | h.c.p. | 2.5071 | 4.0695 | 1.62 | [113] |
| Rh | 45 | f.c.c. | 3.8034 | | | [114] |
| Ir | 77 | f.c.c. | 3.839 | | | [114] |
| Ni | 28 | f.c.c. | 3.524 | | | [115] |
| Pd | 46 | f.c.c. | 3.8907 | | | [116] |
| Pt | 78 | f.c.c. | 3.9242 | | | [106] |

### 3.1.2 Transition Metal Hydrides

Since Thomas Graham found the absorption of large amounts of hydrogen by palladium in 1866[117], the TM hydrides have drawn the attention of physicists and material scientists for many years. While there still quite numbers of TMs remained incapable to form any hydrides resulting from extremely low solubility of hydrogen in these metals at ambient pressure. The development of high-pressure technique provides an efficient method of producing new hydrides since the dramatic increase in the chemical potential of hydrogen gas by compressing it within DAC. The chemical potential pressure dependence[118] is illustrated in **Fig. 3.2**.. The chemical potential of hydrogen gas increase distinctly at room temperature since the pressure reaches in the order of gigapascal. Particularly, the sharp increase in the chemical potential of hydrogen is clearly seen when the pressure is as high as several tens GPa.

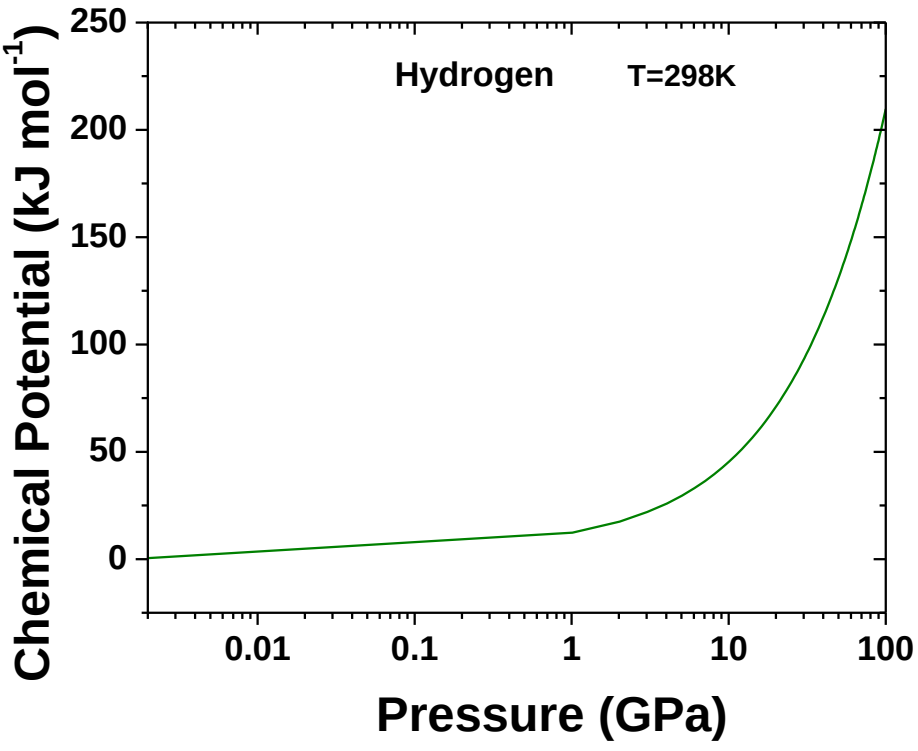


**Fig. 3.2** Chemical potential of hydrogen varies with its pressure

However, many experimental difficulties need to be overcome to obtain high-pressure gases even the inert gases. The upper limit of pressure for inert gases reachable with the available technique by the 1960s does not exceed 2-3 GPa. In order to get high-pressure hydrogen gas, more factors are necessary to be considered, such as its high compressibility, low viscosity, and chemical corrosiveness increasing greatly with temperature and pressure. By the middle of the 1960s, Polish scientists[119],[120] designed a beryllium bronze high pressure chamber to contain compressed hydrogen gas by the conventional compressor. This avoided the direct contact of hydrogen with steel chamber walls, allowing compressing hydrogen to 2.5-3 GPa at ambient temperature and to 1.5 GPa with the temperature below 450 ℃. The "Piston-cylinder" type cell in high-pressure gas technique made it success to synthesis $CrH_{1.0}$, $MnH_{0.96}$ and $NiH_{1.25}$[119]. By the middles of the 1970s, the remained twelve promising TMs from group 4 to 10 in the periodic table are Mo, W, Mn, Tc, Re, Fe, Ru, Os, Co, Rh, Ir, and Pt[121]. In fact, the solubility of hydrogen in these metals usually with the H/M atomic ratio less than $10^{-5}$ to $10^{-7}$, which comparable to the number of various defects in these metals. The Russian scientists[121] from the Institute of Solid State Physics of the USSR Academy of Sciences developed the high-pressure gas technique with their toroidal chambers, promoting the gas-pressure up to 9 GPa. This allowed the successful synthesis of a series of novel TM hydrides, such as $MnH_{0.96}$, $FeH_{0.8}$, $CoH_{1.0}$, $MoH_{1.3}$, $TcH_{0.83}$, $RuH_{0.03}$, $RhH_{1.0}$, $PdH_{1.0}$, $ReH_{0.22}$.

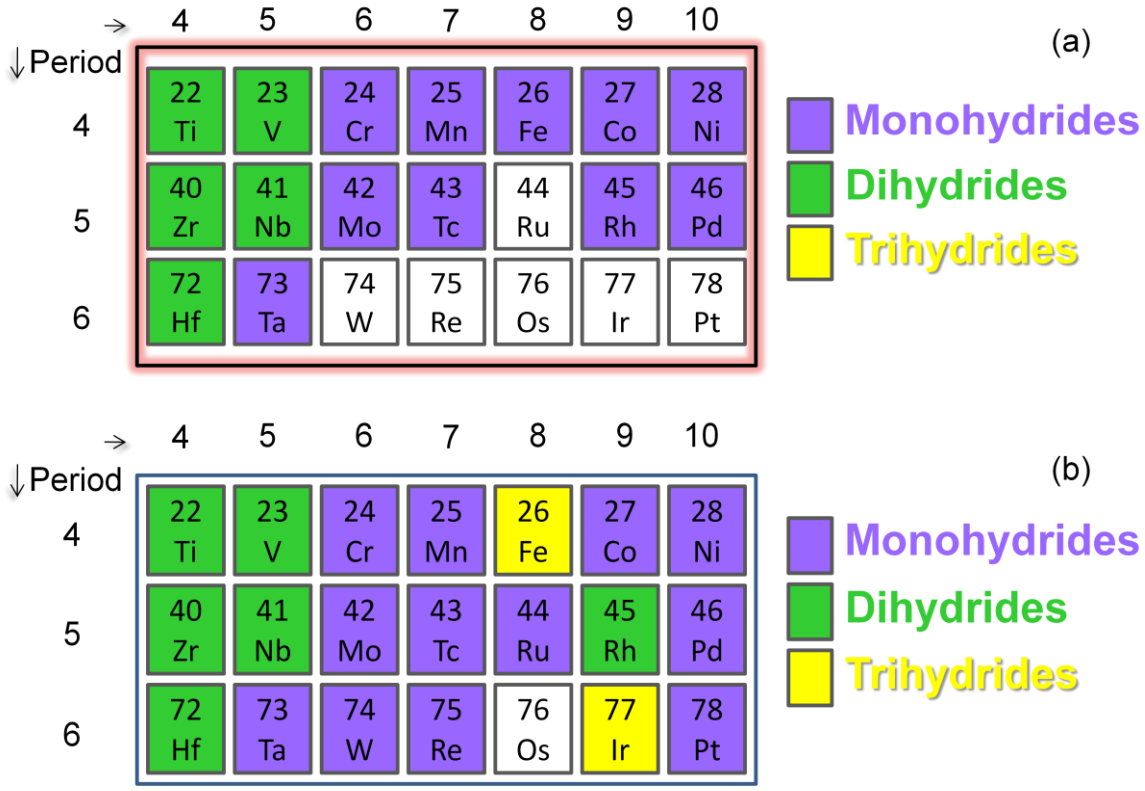


**Fig. 3.3** Binary hydrides formed by various elements in periodic table (a) before and (b) after introduction of DAC.

Recently, the introduction of DAC made it possible to boost compressed hydrogen up to several tens of GPa in most high-pressure labs, even to hundreds GPa in some labs. In this pressure region, the chemical potential of hydrogen gas increase dramatically as shown in **Fig. 3.2**. The binary hydrides formed by the TMs before and after the introduction of DAC are exhibited in **Fig. 3.3** (a) and (b), respectively. The formations of new hydrides, such as monohydrides $WH_{1.3}$[122], $ReH_{0.85}$[13], PtH[123], and RuH[13], and polyhydrides $RhH_2$[124], $IrH_3$[125], $FeH_3$[126] and $NbH_3$, are realized by the introduction of DAC. Osmium is the only one left which cannot form any hydrides.

**Table** 3.3 Crystal structure of hydrides formed by TMs from group 4 and 5 at ambient condition

| Element | Metal structure | Hydrides | Metal sublattice in hydride | Ref |
|---|---|---|---|---|
| Ti | h.c.p. | $TiH_2$ | f.c.c. | [13] |
| Zr | h.c.p. | $ZrH_2$ | f.c.c. | [13] |
| Hf | h.c.p. | $HfH_2$ | f.c.c. | [13] |
| V | b.c.c. | $V_2H$ | b.c.c. | [127] |
| | | $V_2H_3$ | b.c.c. | [127] |
| | | VH | b.c.c. | [127] |
| | | $VH_2$ | f.c.c. | [127] |
| Nb | b.c.c. | $Nb_2H$ | b.c.c. | [127] |
| | | NbH | b.c.c. | [35] |
| | | $NbH_2$ | f.c.c. | [127] |
| | | $NbH_3$ | b.c.c. | [128] |
| Ta | b.c.c. | $Ta_2H$ | b.c.t. | [127,129] |
| | | $TaH_{0.8}$ | b.c.c | [1] |

**Table** 3.4 Crystal structure of hydrides formed by TMs from group 6 and 10 at ambient condition

| Element | Metal | Hydrides | Metal sublattice in | Ref |
|---|---|---|---|---|
| Cr | b.c.c | CrH | f.c.c. or h.c.p. | [13] |
| Mo | b.c.c. | MoH | h.c.p. | [13] |
| W | b.c.c. | $WH_{1.3}$ | h.c.p. | [130, 122] |
| Mn | b.c.c. | MnH | f.c.c. or h.c.p. | [13] |
| Tc | h.c.p. | TcH | h.c.p. | [13] |
| Re | h.c.p. | $ReH_{0.85}$ | h.c.p. | [13] |
| Fe | b.c.c. | FeH | f.c.c. or h.c.p. | [13] |
| | | $FeH_2$ | Tetragonal | [126] |
| | | $FeH_3$ | simple cubic | [126] |
| Ru | h.c.p. | RuH | f.c.c. | [131] |
| Os | b.c.c | -- | -- | |
| Co | h.c.p. | CoH | f.c.c. or h.c.p. | [13] |
| Rh | f.c.c. | RhH | f.c.c. | [13] |
| | | $RhH_2$ | f.c.c. | [124] |
| Ir | f.c.c. | $IrH_3$ | Simple cubic | [125] |
| Ni | f.c.c. | NiH | f.c.c. | [132] |
| Pd | f.c.c. | PdH | f.c.c. | [13] |
| Pt | f.c.c. | PtH | hexagonal | [123] |

The crystal structures of TM hydrides are listed in **Table 3.3** and **Table 3.4**. It is worth mentioning that most of the monohydrides formed by the metals from Group 6 to 10 are based on one of the close-packed structure of metal atoms, namely either hcp (close-packed hexagonal) or fcc (face-centered cubic). Particularly, monohydride of platinum was shown as two phases, PtH-I and PtH-II. Both phases are determined based on the hexagonal metal lattice. In addition, the metal lattice of PtH-II is close-packed hexagonal structure. Therefore, the monohydrides formed by TMs from Group 6 to 10 all possess close-packed structure. Moreover, the dihydrides successfully synthesized by TMs from group 4-10 together with RE metals all have the face-centered cubic metal

lattice with the exception of $FeH_2$, which is based on the tetragonal metal lattice. Up to now, only elements Fe, Nb and Ir from TMs formed trihydrides under high-pressure hydrogen gas. Unlike most of RE metal trihydrides possessing close-packed metal lattice, $NbH_3$ is found based on distorted bcc metal lattice and both $FeH_3$ and $IrH_3$ are determined with simple cubic metal lattice.

Since recently, most of TMs in groups VI-X are investigated under high-pressure hydrogen gas in DAC with pressure up to several tens of gigapascal. Among them, only Fe, Rh and Ir stoichiometric hydrides with H/Me > 1. The question is open if any other TMs can form polyhydrides with the introduction of the high-pressure technique of DAC. In consideration of the upper limit (~40 GPa) of DAC employed in our lab, our colleague firstly studied the nearest neighbors of Rh element in the periodic table due to its relatively lower formation pressure (8GPa) of dihydride, namely Co[133], Pd[134], and Ru[131]. The high-pressure energy dispersive X-ray diffraction patterns of system Co-$H_2$ and Pd-$H_2$ were collected up to pressure ~20GPa, without observation of new hydride expect monohydrides. The monohydride RuH was obtained as Ru-$H_2$ system were compressed at a pressure of 14GPa. While further increase the pressure up to ~30 GPa, no dihydride was formed.

Mo and Ta were chosen to investigate in DAC under high-pressure hydrogen gas in our study since their neighbors formed dihydrides at room temperature and hydrogen pressure even less than $10^{-3}$ GPa. The details for Mo-$H_2$ and Ta-$H_2$ system are presented in section 3.2 and section 3.3, respectively.

## 3.2 Molybdenum Hydrogen System[135]

Prior to our study, the molybdenum hydrogen system has been thoroughly studied in the range of P< 6 GPa and T < 800$^{o}$C [136, 137]. At lower pressure, the hydrogen was dissolved into the bcc metal lattice with the solubility of H/Mo less than 0.07. With further pressure

increase, an hcp hydride with the composition of H/Mo=1.10(3)[137] was formed. In this hydride, hydrogen atoms were confirmed to locate in the octahedral interstitials in the hcp hydride forming NiAs-type structure. For additional over-stoichiometric hydrogen atoms in the crystal structure, it is reasonable to assume that they partially occupied the tetrahedral interstitials. Recently, the theorist[138] has investigated the crystal structures and stabilities of the polyhydrides formed by molybdenum using the first-principles calculation. Their calculation results show that MoH should be stable with the hydrogen pressure range up to 9 GPa and $MoH_2$ should be stable above 9 GPa. What's more, the crystal structures of $MoH_2$ were predicted to possess the same hcp metal lattice as that of MoH. The difference was found only in the nonzero fraction of tetrahedral interstitials occupied by hydrogen. In this study, our efforts are made to check whether the dihydride of molybdenum forms under high-pressure hydrogen gas up to ~30GPa at room temperature.

### 3.2.1 Experimental Section

DAC with flat culets of ~ 400 μm in diameter was employed in this experiment. Gasket made by rhenium was pre-indented under pressure up to~12 GPa. A hole 200 μm in diameter was drilled by laser and served as the sample chamber. Ruby was chosen as a pressure scale for quasi-hydrostatic condition[139]. In the experiment, the molybdenum powder of 99.96% purity was pressed to about 10 μm thickness. Hydrogen was loaded into the gasket hole at room temperature by the technique described elsewhere[140]. The initial pressure of the system was about 0.3 GPa. The excessive hydrogen was necessary since hydrogen served both as a reagent and as a PTM. The presence of hydrogen in the cell was monitored both visually and by Raman spectroscopy. The compression force was increased in steps by a lever mechanism after initial clamping of hydrogen in a DAC The pressure was measured before and after each X-ray diffraction measurement because of a pressure drift caused by gasket relaxation and hydrogen consumption by both the

sample and gasket. And the difference between these values was typically around 1 GPa at pressures above 10 GPa. The pressures labeled in the figure are the pressures measured after the X-ray measurements.

X-ray powder diffraction patterns were measured by the energy-dispersive method with a polychromatic radiation from a conventional tungsten target tube and a 100 μm homemade collimator. X-ray technique is described in more details elsewhere[141]. The cathode voltage of the tube was -40 kV, and the tube current was 20 mA. The scattering angle was calibrated using the diffraction pattern of hydrogen-free molybdenum and assuming its lattice parameter to be a=3.145 Å. Two runs were performed: run 1 for reaching maximal pressure and run 2 to better study the decomposition process. For both runs 2θ value was 21.5(1)º, corresponding to E*d=33.2 keV*Å. The energy scale was calibrated independently before and after each pattern was taken by measuring the positions of the CuKα and InKα X-ray fluorescence lines from separate standards, assuming linear dependence between the channel number of the multichannel analyzer and the photon energy. Additional control of energy calibration was provided by using MoKα and MoKβ fluorescence lines always present in the spectra as an internal standard. Accumulation time was different for each pattern, typically in the range from $2x10^4$–$10^5$ s. All experiments were conducted at room temperature.

### 3.2.2 EDXRD patterns

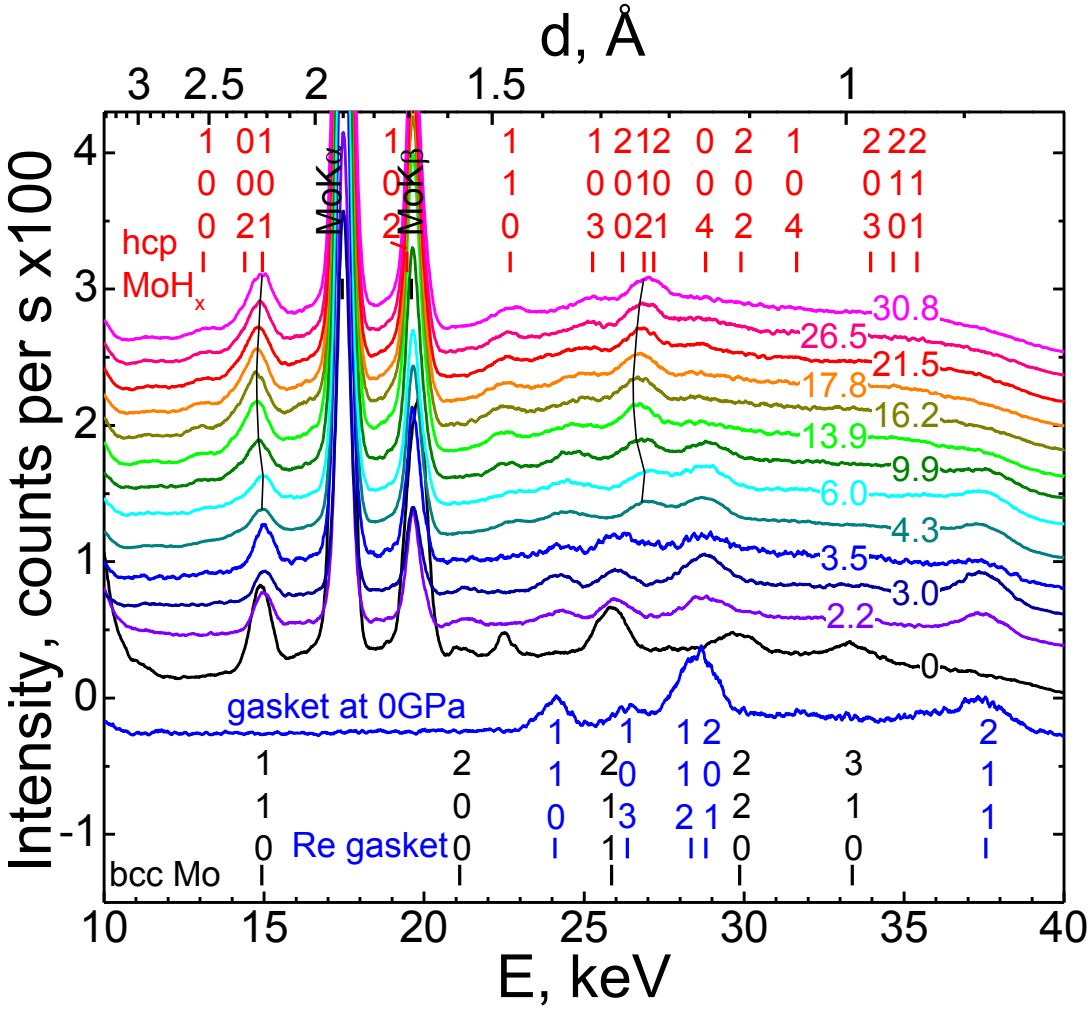


**Fig. 3.4** (color online). EDXRD patterns of Mo in a hydrogen atmosphere, taken during pressure increase in run 1. The thin black lines show pressure evolution of the (101) and (112) peaks of molybdenum hydride

As shown in **Fig. 3.4**, EDXRD patterns transferring from the bcc to the hcp metal lattice was first observed at a pressure of $P_{bcc \rightarrow hcp}$=4.2(1) GPa, which is corresponding to the hydride formation. This is in agreement with the previous report in Ref.[142]. In the pressure range of 6 to15 GPa, the diffraction peaks abnormally shifted with pressure to higher d values (see thin black lines in **Fig. 3.4**), suggesting a continuous increase in the H/Mo composition of the formed hydride. The peaks shifted as usual at higher pressures. No

two-phase mixtures were detected in any pattern, indicating a consequence of relatively fast kinetics. The decomposition of the hydride corresponding to the phase transformation in the metal lattice from hcp to bcc was observed around 1.0(1) GPa in the decompression measurements (see in **Fig.** 3.5). This implied that the phase transition during compression was reversible.

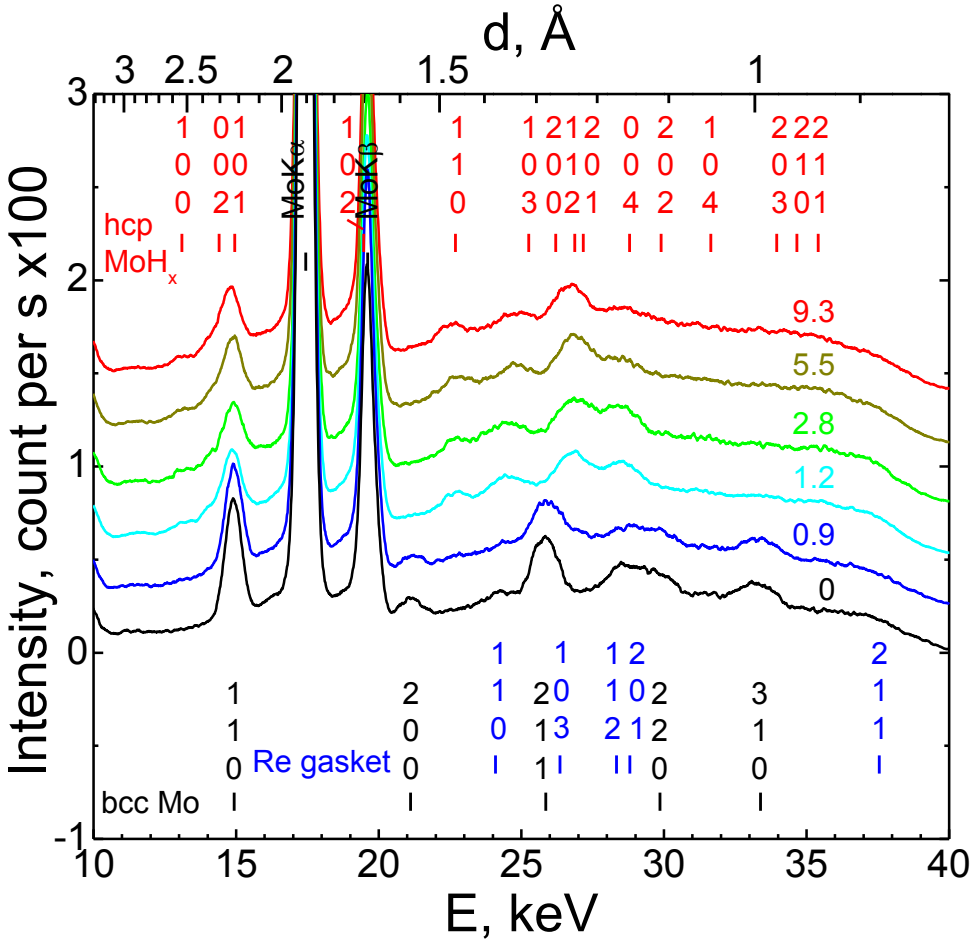


**Fig.** 3.5 (Color online). Energy-dispersive powder diffraction patterns of Mo in a hydrogen atmosphere, taken during pressure decrease in run 2.

### 3.2.3 Volume-pressure dependence

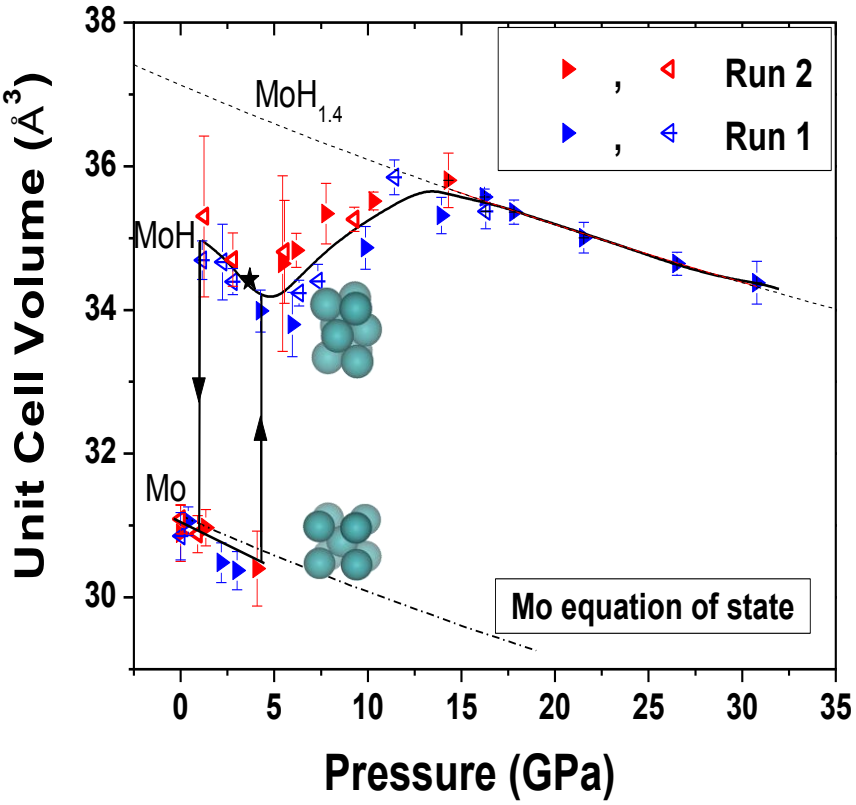


**Fig. 3.6** (Color online). Lattice volumes per metal atom varied with the hydrogen gas pressure.

Atomic volumes, calculated from the EDXRD patterns are plotted in **Fig. 3.6** as a function of hydrogen pressure. The diffraction peaks of the (100), (002), (101), (110), (200), (112) and (201) of hcp-$MoH_x$ were used to calculate its volume at various pressure. The solid and open triangles denote compression and decompression data respectively in **Fig. 3.6** The dashed line below is an equation of state for molybdenum in a neon atmosphere[143]. The arrows show formation and decomposition pressures for $MoH_x$, and the solid black lines are guides for the eye. The dashed line is a fit of the V(P) data at P>15 GPa (see the corresponding equation of state parameters in **Table 3.5**).

Volume-pressure dependence for bcc Mo at hydrogen pressure below 4.3 GPa does not differ from that for Mo in a neon atmosphere within data uncertainties. Volume

discontinuity at 4.3 GPa is $\Delta V_{bcc \rightarrow hcp}$=2.2(2) Å$^3$ per Mo atom, which agrees with previous estimates 2.1 Å$^3$ per Mo atom[136] and 2.08(2) Å$^3$ per Mo atom for a hydride with $MoH_{1.10(3)}$ composition[137]. It is worth note that the H/Mo content in the pressure range of 6-15 GPa increases continuously with pressure. This similar behavior was also observed in the metal-hydrogen systems with the hcp structure of primary hydrogen solution, such as Co-$H_2$[133], Ru-$H_2$[131], Tc-$H_2$[121], W-$H_2$[122] and Re-$H_2$[144] systems. The normal compression behavior was shown with pressure above 15 GPa and the V(P) dependence for MoHx can be fit by the third-order Birch-Murnaghan equation of state as shown below

$$P(V) = \frac{3B}{2}\left[\left(\frac{V_0}{V}\right)^{\frac{7}{3}} - \left(\frac{V_0}{V}\right)^{\frac{5}{3}}\right]\left\{1 + \frac{3}{4}(B' - 4)\left[\left(\frac{V_0}{V}\right)^{\frac{2}{3}} - 1\right]\right\} \quad (1.26)$$

where bulk modulus pressure derivative is fixed as $B_0' = 4$, namely, the second-order Birch-Murnaghan equation

$$P(V) = \frac{3B}{2}\left[\left(\frac{V_0}{V}\right)^{\frac{7}{3}} - \left(\frac{V_0}{V}\right)^{\frac{5}{3}}\right] \quad (1.27)$$

$V_0$ and B are volume at 0 GPa and bulk modulus, respectively. The fitting results are listed in **Table 3.5**. $V_0$ for pure Mo is obtained from our experiments, and B for Mo in a neon atmosphere is taken from the literature[143]. As seen in **Table 3.5**, the bulk modulus of MoHx is comparable to that of pure molybdenum, typical for the hydrides with a fixed composition[13]. Thus, the hydrogen composition H/Mo of the hydride saturates at ~15 GPa and can be considered constant at higher pressures.

**Table** 3.5 Comparison of the equation of state parameters for Mo and saturated $MoH_x$

| **Substance** | **$V_0$, Å$^3$ per Mo atom** | **B, GPa** |
|---|---|---|
| Bcc Mo | 15.55 | 273 |
| hcp MoHx above 15 GPa | 18.5 | 340 |

### 3.2.4 Evaluation of the composition of saturation molybdenum hydride

We estimated the composition of saturation molybdenum hydride by volumetric considerations. Since the volume expansion per Mo atom is measured directly by X-ray diffraction, a composition H/Mo of the saturated molybdenum hydride can be estimated by comparing volume expansion per Mo atom with the expected volume expansion caused by each H atom. In a close-packed lattice of TM atoms, each hydrogen atom located in an octahedral interstitial site expands the lattice by about 2.0-2.5 Å$^3$ per H atom, whereas in a tetrahedral site the volume expansion is 2.2-3.2 Å$^3$ caused by per H atom (see Ref.[13] for particular values for different metals). More accurate estimation can be made relying on the recent experimental[137] and theoretical[138] works.

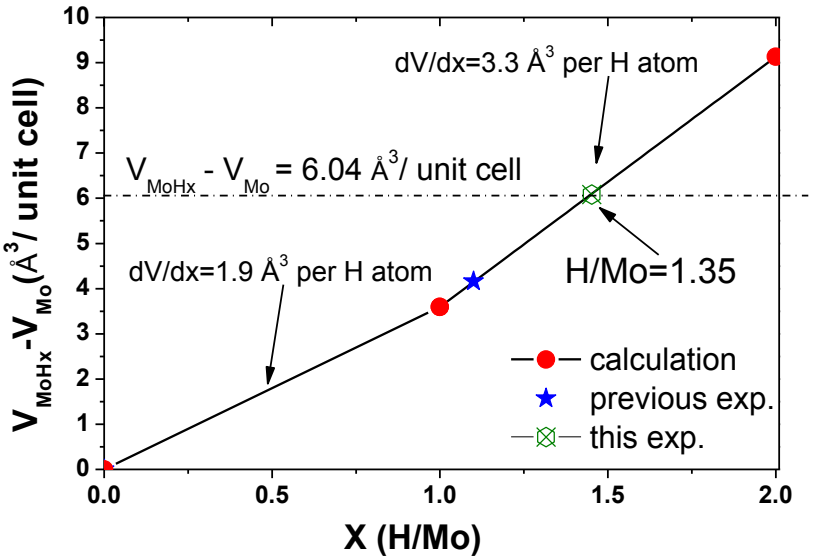


**Fig. 3.7** (Color online). Volume expansion of molybdenum hydrides, caused by hydrogen. The results of ab-initio calculations[138] are shown by the black filled circles, the experimental results of Ref. [137] are shown by the red squares, and the green open circle is present data.

The volume difference V($MoH_{1.10}$)-V(Mo)=2.08(2) Å$^3$ per Mo atom was accurately determined in Ref [137] and the corresponding volumes are shown by the red squares in **Fig. 3.7**. Theoretical calculations[138] results show the volume change

V(MoH)-V(Mo)=1.9 $Å^3$ per Mo atom in monohydride and V($MoH_2$)-V(Mo)=5.2 $Å^3$ per Mo atom for a hypothetical $MoH_2$ compound at 0 GPa. In this calculation, the hydrogen atoms are supposed occupied all octahedral and half of the tetrahedral interstitials in the hcp metal lattice of the hypothetical dihydride. Therefore, the occupation of the tetrahedral interstices results in the volume expansion of 3.3 $Å^3$ per H atom. All these data together with our estimate V($MoH_x$)-V(Mo)=6.0(4) $Å^3$ per unit cell are presented in **Fig. 3.7**. Assuming in a saturated molybdenum hydride above 15 GPa, octahedral interstices are fully occupied and the tetrahedral interstices partially occupied, then the composition x=H/Mo can be estimated as $x=1\,{}^1/_3$ , which is the same as that of tungsten hydride[122]. Moreover, the several saturation hydrides formed by TMs were found to be nonstoichiometric, such as $ReH_{0.85}$[144], $TcH_{0.8}$[145] and $WH_{1.3}$[122]. It is unclear why these metals do not form higher stoichiometric hydrides as the hydrogen pressure further increased.

### 3.2.5 Discussion and Conclusion

In this study, the crystal structure and the lattice parameters of molybdenum were investigated in the pressure range up to 30 GPa. Interestingly, the composition H/Mo of molybdenum hydride is shown to increase continuously with pressure increase rather than being constant. The composition H/Mo saturates at about 1.35 (10) around 15 GPa, and no further hydrogen absorption occur up to the maximal reached pressure, which is contrary to the ab-initio calculation.

The Mo-H system failed to form $MoH_2$ under high-pressure hydrogen gas can be explained by a blocking effect, as originally proposed by Switendick[146]. According to this rule, the hydrogen-hydrogen interatomic distance in all dihydrides should be bigger than 2.14 Å, which is a manifestation of a short-range H-H repulsion. There are very few metal hydrides which violate this empirical rule. According to the first principle calculations[138], the shortest H-H distance of 2.15 Å in the hypothetical $MoH_2$ is between

the octa and tetra sites. It should be noted that the GGA-PBE calculation method used in ref[138] typically overestimates interatomic distances by about ~0.5%, and $MoH_2$ should be close to the violation of the shortest H-H distance criterion. This is supposed the reason of failure of formation of $MoH_2$ for the Mo-H system.

The shortest H-H interatomic distance in our saturated compound is hardly estimated because the X-ray diffraction studies done in our work are not sensitive to the hydrogen positions. The lattice parameters of $MoH_{1.35}$ obtained from our study are found smaller than these of the hypothetical $MoH_2$. While hydrogen atoms can displace from the ideal positions of their sites to relax the H-H repulsion. Thus, further theoretical and experimental work is needed to understand why the saturation composition of hydrogen in molybdenum is non-stoichiometric.

## 3.3 Tantalum Hydrogen System[147]

The TMs from group 4 and 5 all were known to form dihydrides under hydrogen pressure less than $10^{-3}$ GPa at room temperature[13], with the exception of tantalum in which the maximal hydrogen solubility ever observed was 0.86 at 1.6 GPa and 400 K[3]. Owing to the development in high-pressure technique, Nb were even found to form $NbH_{2.5}$ and $NbH_3$[128] by means of compressing hydrogen molecules in DAC to pressures of tens gigapascals. Quite recently the tantalum dihydride were predicted to be capable to be formed and stable in the hydrogen pressure range of 0-50 GPa by the ab-initio calculation[148]. This triggers us to explore the tantalum hydrogen system under high pressure. The hydrogen-rich phase at high pressure is expected to form.

### 3.3.1 DAC experiments

Tantalum foils with a purity of 99.9% were served as samples in this work. Tantalum with a thickness of 10 was employed in the DAC. The oxidized surface layer of the

sample was removed by scratching with a sharp scalpel before the high-pressure experiment. This performance dramatically improved the kinetics of hydrogenation.

The DAC experiments were carried out at room temperature with pressures up to 41 GPa. The DAC cell, the gas loading system and the in situ energy-dispersive XRD setup was the same as in our previous experiments for Mo-H system. Hydrogen was always in excess, serving both as a reagent and as the pressure transmitting medium. Its presence was monitored both visually and by Raman spectroscopy. In the experiments, a tiny piece of ruby was used as a pressure sensor. The quasi-hydrostatic pressure scale proposed by Mao et al.[149] allowed the determination of pressure with an accuracy of ±0.3 GPa.

## A EDXRD patterns

X-ray powder diffraction was collected by using polychromatic radiation which is generated by a conventional tungsten target tube and collimated down to about 100 μm by a homemade a collimator. Prior to each EDXRD measurement, the X-ray beam was positioned at the center of the gasket hole with an accuracy of 10 μm using an intensity monitor of unscattered radiation. The size of the hole in the gasket was no less than 120 μm at the highest pressure of 41 GPa, this procedure, therefore, ensured the collected signals were purely from the sample without contamination from the gasket at any measured pressure. The X-ray scattering angle $2\theta$ was set at about 18° and calibrated at the beginning of each experiment using a diffraction pattern of the hydrogen-free initial bcc Ta foil at ambient pressure. The resolution of the setup was $\Delta d/d \approx 5\%$. Accumulating a diffraction pattern at any given pressure required about one day. The lattice parameters of the synthesized Ta-H phases were obtained by the le Bail refinement of experimental energy-dispersive XRD patterns normalized to a constant background level. At pressures above 10 GPa, the XRD measurements were typically accompanied by a pressure drift of about 1 GPa. These final pressure values labeled in the figure served as the measuring pressures of the DAC experiments.

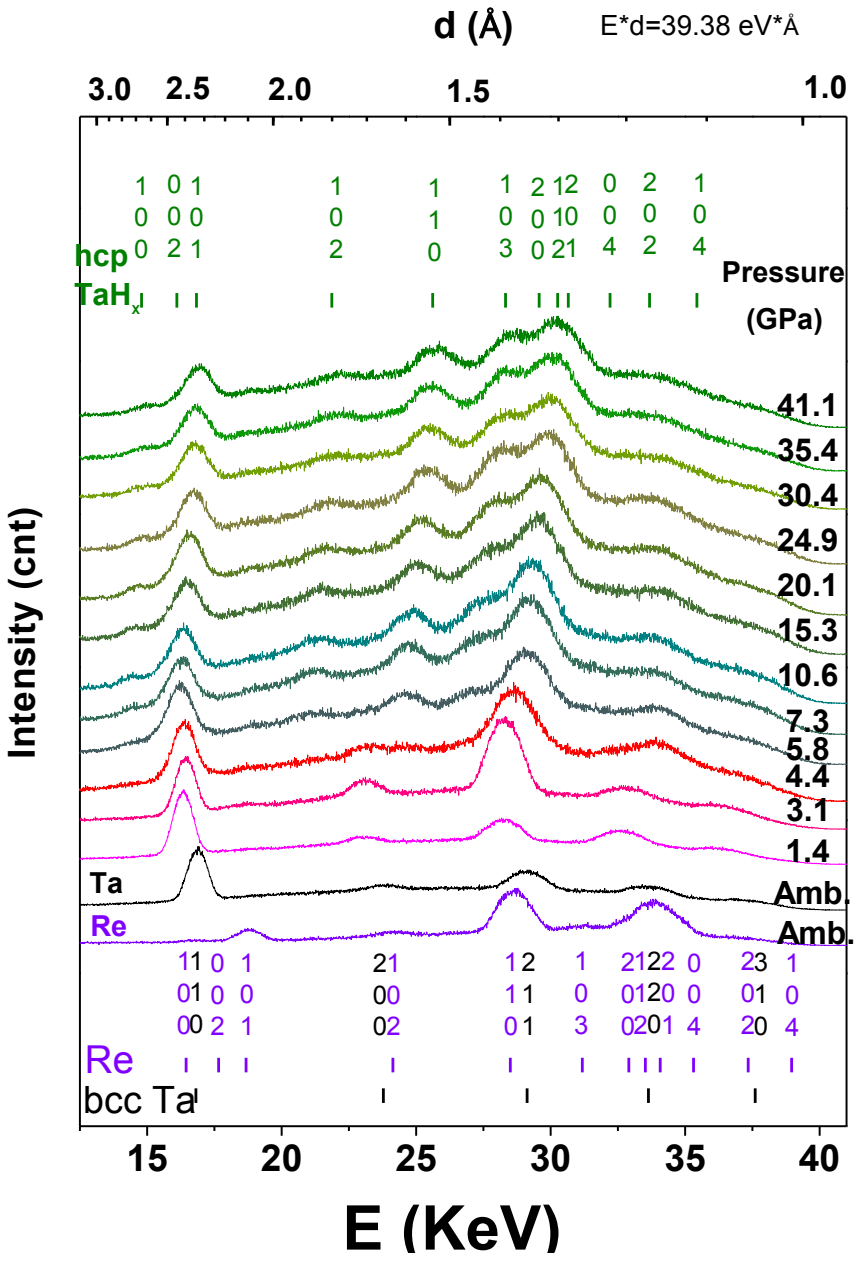


**Fig. 3.8** Energy-dispersive X-ray diffraction patterns of tantalum in a hydrogen atmosphere measured in the course of a step-wise pressure increase in a DAC.

The EDXRD of Ta-H system under high-pressure during compression and decompression are shown in **Fig. 3.8** and **Fig. 3.9**, respectively. The sample was equilibrated for approx. one hour when the pressure was changed and the diffraction pattern was accumulated about 24 hours. The maximal pressure in the first run was ~41 GPa. The diffraction patterns are shifted vertically for clarity. The pressures are marked in the right of each diffraction pattern.

The peaks with energy $E$ lower than 12 keV are the L fluorescence emission lines of tantalum; other peaks are of a diffraction origin. The blue ticks at the bottom indicate calculated positions of the strongest diffraction peaks from the hydrogen solution in hcp rhenium with $a$ = 2.79 Å and $c$ = 4.41 Å at P = 5 GPa[150]. As seen in **Fig. 3.8**, no obvious contamination of gasket in any diffraction pattern was observed. The black ticks at the bottom of the figure show calculated peak positions for bcc Ta with $a$ = 3.30 Å at ambient pressure. The first diffraction pattern of Ta-H system was accumulated at 1.4 GPa since the DAC was loading with high-pressure hydrogen gas. It is worth noting that the broad diffraction peaks of bcc tantalum shift to higher $d$-values considerably. At this pressure, the non-stoichiometric monohydride $TaH_{1-x,}$ which is known to form at this pressure, possesses the face-centered orthorhombic metal lattice with space group *Fmmm*, $a = 4.83\text{Å}$, $b = 4.79\text{Å} \approx a$, $c = 3.46\text{Å} \approx a/\sqrt{2}$ [151]. This crystal structure of metal lattice of the non-stoichiometric monohydride $TaH_{1-x}$, can be considered as a distorted bcc lattice. No splitting of individual peaks arising from the lattice distortions was observed in our energy-dispersive XRD measurements due to its low resolution.

Additionally, the qualitative changes occurred at $P$ = 5.5 GPa as seen in **Fig. 3.8**, indicating the formation of a new phase with an hcp metal lattice of Ta-H system. Further increase in pressure up to 41 GPa, the peaks shifted to lower d-values as usual with pressure, suggesting the stability of the new phase. This new hydrogen-rich phase was presumed as dihydride from the volume evaluation. Its composition was accurately determined in ex situ experiments (see the description in the following part). The olive ticks at the top label positions of the strongest peaks of tantalum dihydride at $P$ = 41.1 GPa based on the hcp metal lattice with $a$ = 3.08 Å and $c$ = 4.88 Å. No two-phase mixtures were detected in any pattern, indicating a consequence of relatively fast kinetics.

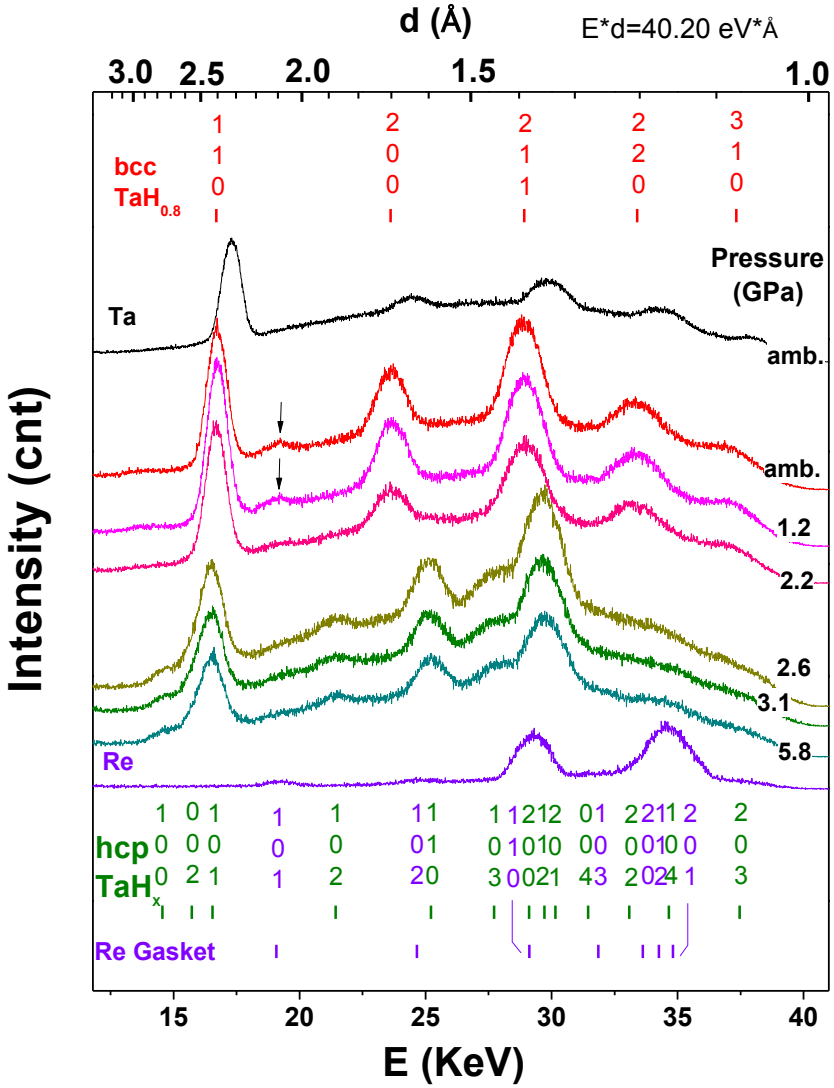


**Fig. 3.9** Energy-dispersive X-ray diffraction patterns of tantalum (shifted vertically for clarity) in a hydrogen atmosphere collected in the course of a step-wise pressure decrease in the second series of measurements with the maximal pressure of 9 GPa.

The EDXRD during a step-wise pressure releasing process were shown in **Fig. 3.9**. The bottom olive ticks show positions of the strongest peaks for the hcp tantalum dihydride at $P$ = 9 GPa with $a$ = 3.19 Å and $c$ = 5.07 Å. The blue curve labeled "Re" shows a diffraction pattern from the strongly textured rhenium gasket measured after decompressing the cell to ambient pressure. The top red ticks show the calculated positions of the strongest peaks for monohydride possessing bcc metal lattice with $a$ = 3.40 Å. Other commentaries are the same as in the caption for **Fig. 3.8**. The dihydride

could not, however, be recovered to ambient pressure at room temperature. It decomposed into monohydride around P=2.2 GPa since the qualitative changes were observed from pattern labeled "P=2.6 GPa" to pattern labeled "P=2.2 GPa". The equilibrium pressure for the ternary "hydrogen gas"+"lower hydride"+"higher hydride" equilibria is likely to be much closer to the decomposition pressure of the higher hydride than to the midpoint between the pressures of its formation and decomposition[152]. Therefore, determining the decomposition pressure is crucial for the thermodynamics of the Ta-H system. Hence, the decomposition pressure $P$ = 2.2(4) GPa was determined more accurately in the second series of measurements within a smaller pressure range up to 9 GPa.

## B The pressure-volume dependencies

The atomic volumes of per metal atom of Ta-H system as a function of pressure were presented in **Fig. 3.10**. The atomic volumes of the orthorhombic monohydride presented as a function of pressure were estimated from the mean lattice parameter of its pseudo-bcc unit cell. In the top panel, the vertical black lines with arrows indicate the pressures of phase transitions. By comparing the steps at 5.5 and 1.4 GPa in the $V(P)$ dependence composed by the solid symbols in the figure, we found that this new phase formed around $P$ = 5.5 GPa from tantalum monohydride was accompanied by approximately the same volume expansion as the formation of monohydride from pure tantalum. Therefore, the new high-pressure phase was likely to be a tantalum dihydride. At $P$ > 5.5 GPa, the atomic volume $V(P)$ of the dihydride monotonically decreased with increasing pressure, while the axial ratio of its hcp unit cell stayed virtually unchanged and equal to $c/a$ = 1.59(1), which is somewhat less than the ideal value of $c/a = \sqrt{8/3} \approx 1.633$. The $V(P)$ values of the tantalum dihydride measured during compression (open symbols in **Fig. 3.10**) well agree with the $V(P)$ dependence constructed during decompression.

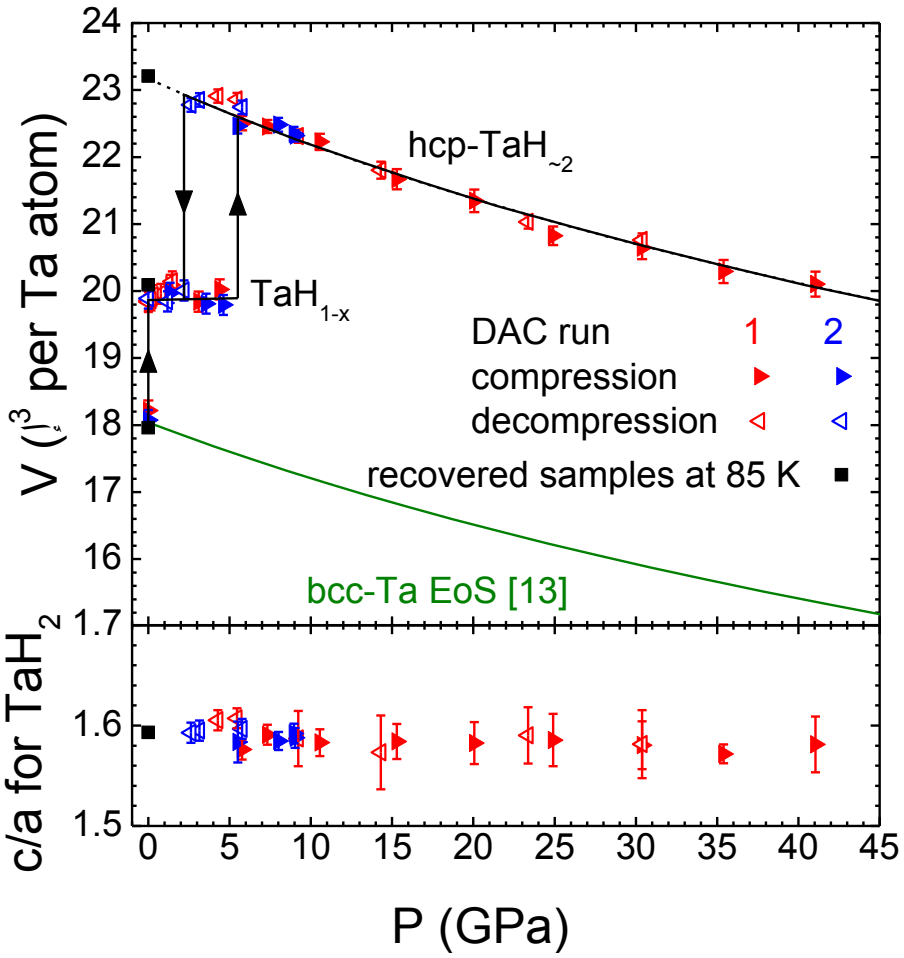


**Fig. 3.10** Top panel: The pressure-volume dependencies for Ta under high hydrogen pressure. Bottom panel: The c/a ratios for the hcp-$TaH_{\sim 2}$. The black squares show $V_0$ and c/a for the recovered $TaH_{\sim 2}$ and $TaH_{1-x}$ samples and initial Ta measured at 85 K and ambient pressure, see Section "Ex situ studies of recovered Ta-H samples".

The pressure-volume data for the hcp tantalum dihydride were fitted to the Murnaghan equation of state

$$V(P) = V_0 \left[1 + P\left(\frac{B'}{B}\right)\right]^{-1/B'} \tag{1.24}$$

and to the second-order Birch-Murnaghan equation

$$P(V) = \frac{3B}{2}\left[\left(\frac{V_0}{V}\right)^{\frac{7}{3}} - \left(\frac{V_0}{V}\right)^{\frac{5}{3}}\right] \tag{1.27}$$

The fitting using these equations resulted in virtually the same values of the fitting parameters $V_0$ and $B$, which are indicated in **Table 3.6**. The EOS of $TaH_{\sim 2}$ thus obtained is shown by the solid black curve in **Fig. 3.10**.

As seen from **Fig. 3.10** and **Table 3.6**, the value of $V_0$ = 23.2(2) Å$^3$ per Ta atom obtained from fitting the V(P) high-pressure data keeps consistent with the atomic volume 23.14(4) Å$^3$ per Ta atom of tantalum dihydride synthesized in a toroid-type high-pressure chamber and examined by X-ray diffraction at ambient pressure and T = 85 K (this ex situ experiment is described in the next Section of the paper). The agreement of the experimental V(P) dependence to the Murnaghan equation indicates that the hydrogen content of the tantalum dihydride should be nearly independent of pressure in the studied pressure range up to 41 GPa, since varying the hydrogen content would result in strong deviations from that equation (see, e.g., publications for the hcp-structured hydrides with varying compositions in the Mo-H [135] and W-H [122] systems).

**Table** 3.6 Atomic volume $V_0$, bulk modulus $B$ and its pressure derivative $B'$ at ambient pressure obtained for $TaH_{\sim 2}$ and Ta as fitting parameters of the equation of state and by the ex situ measurements.

| Equation of state fits at 300 K | | | | Recovered samples at |
|---|---|---|---|---|
| Substance | $V_0$, Å$^3$ per Ta | $B$, GPa | $B'$ | $V_0$, Å$^3$ per Ta atom |
| bcc-Ta in Ar[153] | 18.04 | 195(5) | 3.4(1) | 17.96(3) |
| hcp-$TaH_{\sim 2}$ in $H_2$ | 23.2(2) | 210(20) | 4 (fixed) | 23.14(4) |

## 3.3.2 *Ex situ* studies of recovered Ta-H samples

## A Synthesis of Sample

Tantalum with a thickness of 160 μm was employed in toroid experiments. The samples of tantalum dihydride for ex situ measurements were obtained at 9 GPa in a toroid-type high-pressure chamber[154] with $NH_3BH_3$ as an internal hydrogen source. The method of hydrogenation is described elsewhere[155]. The temperature was determined by

Chromel-Alumel thermocouple within an accuracy of ±10 °C. The pressure was measured within an accurate to ±0.5 GPa by a preliminary calibration of the high-pressure apparatus against the ram load. Only orthorhombic tantalum monohydride was obtained after exposure of the Ta sample to a hydrogen pressure of 9 GPa at room temperature for a day; this was supposed to be caused by the low kinetic of formation of dihydride from the thick layer. A one-day exposure to the hydrogen with the same pressure and 250 °C also produced the monohydride, presumably, resulting from the increase in the formation pressure of the dihydride with temperature increase. by exposing the Ta foil for one day to 150 °C, samples we obtained were composed mainly of the dihydride and a few percent of the monohydride. Pure samples of the hcp tantalum dihydride were steadily synthesized by holding the sample for 1 day at 150 °C and for another one day at 100 °C at a hydrogen pressure of 9 GPa. When the hydrogenation was completed, the sample together with the chamber was put into the liquid $N_2$ to cool down. The pressure was released gradually and the chamber was disassembled in liquid nitrogen. The sample was preserved in liquid nitrogen to avoid the losses of hydrogen.

## B XRD of sample for *Ex situ* studies

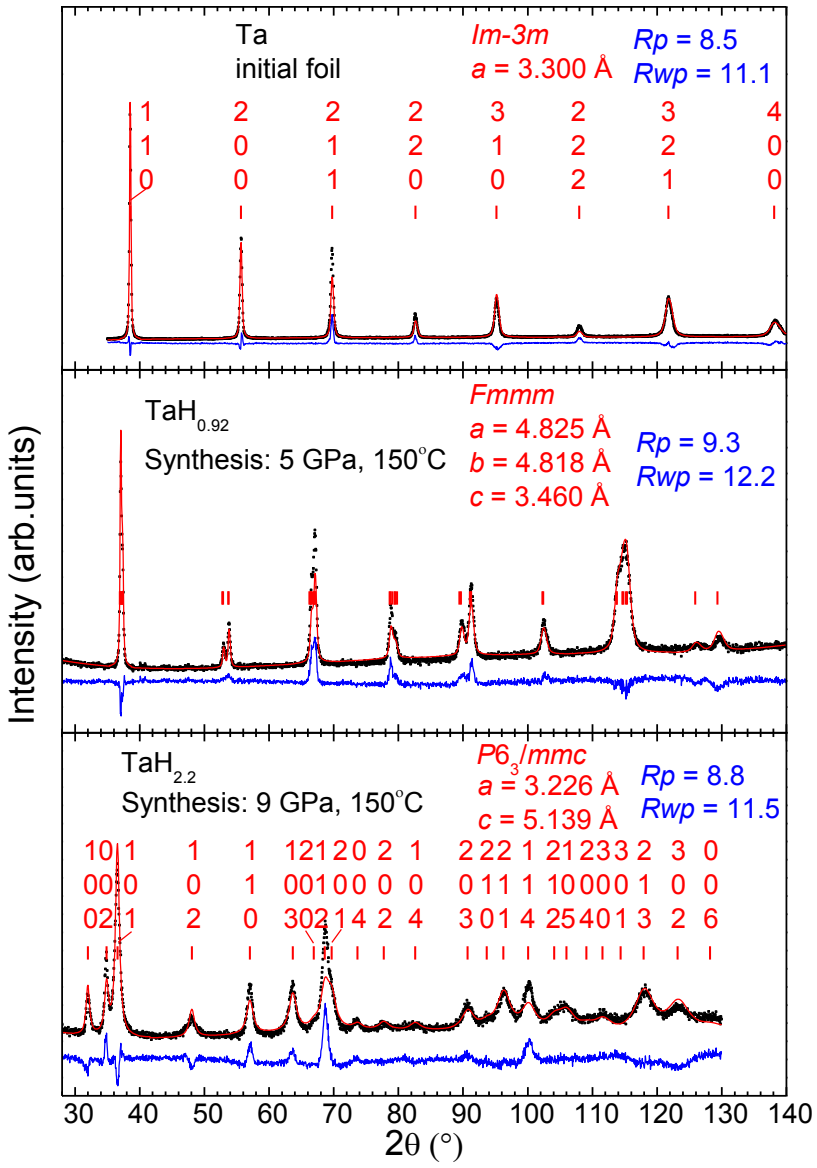


**Fig. 3.11** XRD patterns of the initial Ta foil (top) and Ta samples hydrogenated at 5 GPa (middle) and 9 GPa (bottom) at 150 °C. Ambient pressure, $T$ = 85 K, Cu Kα radiation.

The samples synthesized by toroid-type chamber were tested by XRD with a powder Siemens D500 diffractometer at 85 K. The diffractometer equipped with a homemade nitrogen cryostat allowed loading the samples directly from the liquid $N_2$ bath preventing intermediate warming. The Rietveld profile refinements method was used to analyze the obtained diffraction patterns.

An XRD pattern of one of the single-phase samples of tantalum dihydride measured at 85K is present at the bottom of **Fig. 3.11**. In contrast, diffraction patterns of pure Ta (top panel) and tantalum monohydride prepared at 5 GPa and 150 °C (middle panel) were also shown in **Fig. 3.11**. The samples of the mono- and dihydride were very brittle. In order to diminish the texture effect, the samples were powdered under liquid $N_2$ before the X-ray examination. For the same reason, pure Ta from the powder of monohydride degassed by annealing in vacuum at 650 °C was employed in the X-ray measurement. In the figure, the black points stand for the experimental data, the red curves show the Rietveld fits, and the blue curves are the fit residuals. The rather large residual R-factors are mostly due to the large grain size and strong texture of the samples.

## C Determination of the hydrogen content in high-pressure hydride

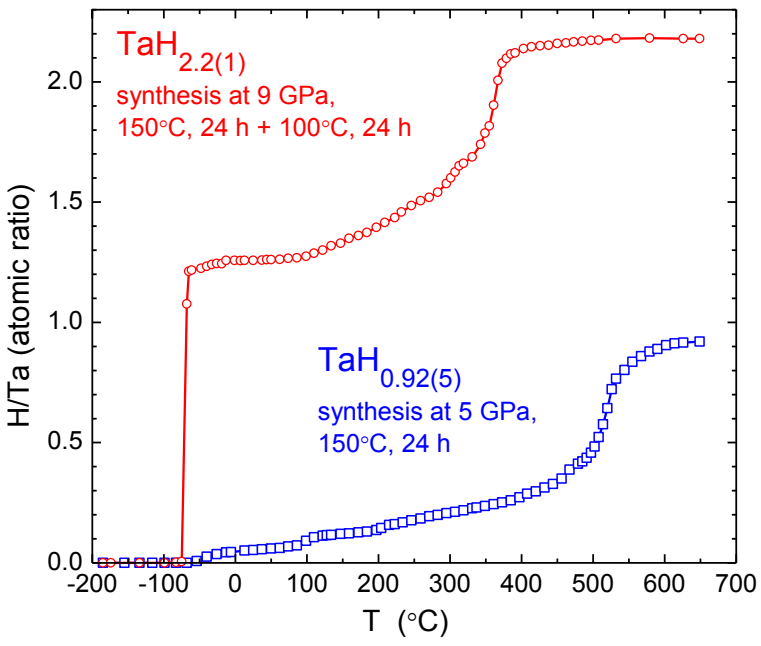


**Fig. 3.12** Hydrogen release from the recovered $TaH_{2.2}$ and $TaH_{0.92}$ samples heated in vacuum at a rate of 10 °C/min.

The mean H-to-metal atomic ratio of the obtained samples was determined by thermodesorption of hydrogen into a pre-evacuated measuring system in the regime of heating the sample from −186 to 650 °C at a rate of 10 °C $min^{-1}$ [156]. The accuracy in determining the atomic ratio $x$ = H/Ta was $\delta x/x$ = 5% since the accuracy in determining the mass by the analyzed probe is a few milligrams.

Thermodesorption curves for the recovered single-phase samples of tantalum mono- and dihydride synthesized in toroid-type apparatus were presented in **Fig. 3.12**. As shown in **Fig. 3.12**, the decomposition of dihydride is an obvious two-stage process. Firstly, more than half of the hydrogen content ($\Delta$(H/Ta) ≈ 1.3) of the dihydride samples was suddenly released in a considerably narrow temperature interval near T = –75 °C, indicating the transformation from dihydride to monohydride. Then further desorption of hydrogen from monohydride started at ~100 °C and continued up to ~400 °C with an amount of $\Delta$(H/Ta) ≈ 0.9. Therefore, the hydrogen content of the new hcp tantalum dihydride was determined to be H/Ta = 2.2(1) and thus noticeably exceeded the stoichiometric ratio H/Ta = 2. The sample of monohydride synthesized at 5 GPa demonstrated a somewhat higher thermal stability and fully decomposed after heating up to about 550 °C instead of ~400 °C. The decreased thermal stability of the monohydride formed from the decomposed dihydride is typical for metal hydrides when they subjected to hydrogenation/dehydrogenation cycling[157]. The directly synthesized monohydride samples often have a surface covered by the oxide layer, which limits the rate of dehydrogenation to some degree. In contrast, the monohydride formed from the decomposed dihydride usually possesses fresh, non-contaminated surfaces because its large expansion and contraction lead to the cracking of the sample during the hydrogenation/dehydrogenation cycle.

## D Lattice expansion of Ta upon hydrogenation

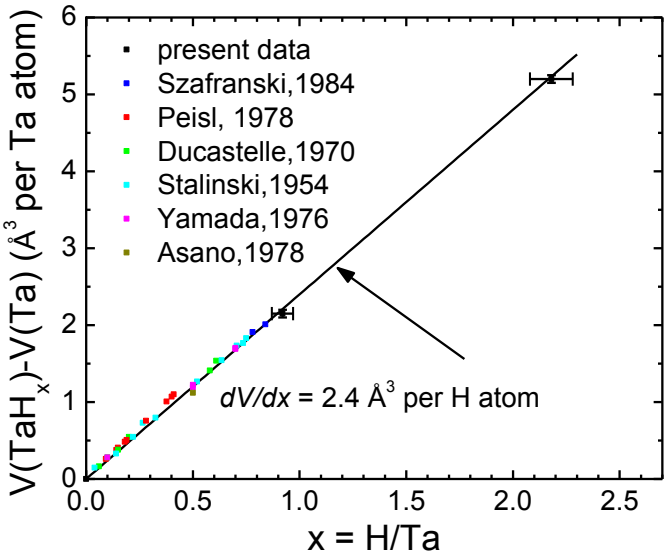


**Fig.** 3.13 Lattice expansion of Ta upon hydrogenation. The black symbols stand for the present data; other colors are for the literature data[1, 134, 2-5, 6,7]. The uncertainty in *V* is smaller than the symbol size.

As reported in literature [1,3,118,5,6,148], the orthorhombic solid solutions of hydrogen in tantalum formed accompanied by linear volume expansion with a slope of about 2.4 Å$^3$ per H atom at H/Ta ≤ 0.86. As shown in **Fig.** 3.13, the hydrogen-induced volume increase of the orthorhombic monohydride $TaH_{0.92}$ and hcp dihydride $TaH_{2.2}$ synthesized in the toroid-type apparatus well obey such a linear dependence. The Vegard law is thus applicable to the Ta-H system in the whole studied composition range of 0 ≤ H/Ta ≤ 2.2.

### 3.3.3 Discussion and conclusion

Up to now, all the TM dihydrides possess fcc metal lattice with the exception of $NbH_2$, which was based on an hcp metal lattice above 40 GPa[128]. The hcp crystal structure is typical of alkali-earth metal dihydrides under sufficiently high pressures. Even for the RE

metal dihydrides, the fcc crystal structure is more common. Actually, the hcp structure was only found in two RE metal dihydrides, $EuH_2$[158] and $YbH_2$[159]. Although vanadium[160], molybdenum[138], and tungsten[122] were predicted to form hcp-based dihydrides by theoretical calculation, experiments, however, showed that the hcp hydrides of these metals were essentially non-stoichiometric with their maximal hydrogen content less than H/Me = 3/2 [122,135].

It is worth mention that a few new non- and over-stoichiometric hydrides were synthesized recently in the Nb-H system under high-pressure: fcc-$NbH_{2.5–3}$, hcp-$NbH_{2.5}$, dhcp-$NbH_{2.5}$, and distorted bcc-$NbH_3$[128]. Since none of them was observed in a single-phase state, it is not clear which of these phases are stable. Additionally, different experimental runs gave different sequences of phase transformations, making the analysis is further complicated. In the work, no phases with $x \geq 2.5$ in the Ta-H system was observed. Since Ab initio calculations by Zhuang et al.[148] underestimated the equilibrium formation pressure of $TaH_2$, 0 GPa instead of our experimental estimate of 2.2 GPa, therefore the formation pressure of higher hydrides can be expected also considerably exceed 50 GPa proposed for $TaH_4$ in their work[148]. Presumably, phases with $x \geq 2.5$ in the Ta-H system could be formed at higher pressures.

As shown in **Fig. 3.11**, tantalum dihydride possesses an hcp metal lattice with the lattice parameter of *a = 3.226* Å and *c* = 5.139 Å. The shortest interstice of *c*/4 = 1.28 Å is that between the tetrahedral sites. According to the well established Switendick rule, the minimal distance between hydrogen atoms should not be much less than 2 Å in any TM. Consequently, the mutual blocking between hydrogen atoms leads to no more than half of the tetra positions in the hcp-$TaH_{\sim 2}$ could be occupied. The maximal number of H atoms accommodated at the tetra-sites is equal to the number of metal atoms in the hcp lattice. The same number of H atoms can be located at the octa-sites. Thus the total hydrogen content of the hcp tantalum dihydride should not more than H/Ta = 2 if the Switendick

rule is applicable. The arrangement of the extra H atoms in the crystal structure of our samples of $TaH_{2.2}$ remains an open problem.

Further neutron diffraction investigation is believed to be feasible. For example, a possible solution is the occurrence of a formation of a large number of stacking faults in the hcp metal lattice of $TaH_{2.2}$. It is worth note that in the double hcp lattice formed by alternating hcp and fcc layers of metal atoms, H-to-metal atomic ratios of up to $x = 2.5$ is possible as the shortest H-H distance is realized between the tetra- and octa-sites (this type structure has recently been proposed for the dhcp-$NbH_{2.5}$ [128]).

# Chapter 4. **Summary and Conclusions**

## 4.1 Rare-earth metal trihydrides

**Table** 4.1 Lattice parameters and molar volume of hexagonal and cubic phases of different RE trihydrides

| Trihydrides | Atomic Number of Forming RE elments | Initial Structure hcp | | | Transition Pressure (GPa) | High-pressure fcc* | |
|---|---|---|---|---|---|---|---|
| | | Lattice parameter (Å) | | Molar Volume ($cm^3$) | | Lattice Parameter (Å) | Molar Volume ($cm^3$) |
| | | a | c | | | | |
| $ScH_3$ | 21 | | | | ~20 | | |
| $YH_3$ | 39 | 3.67 | 6.62 | 23.3 | 7.7 | 5.28 | 22.2 |
| $SmH_3$ | 62 | 3.78 | 6.80 | 25.3 | 2.0 | 5.37 | 23.3 |
| $GdH_3$ | 64 | 3.75 | 6.69 | 24.5 | 5.0 | 5.36 | 23.2 |
| $TbH_3$ | 65 | 3.70 | 6.66 | 23.8 | 6.0 | 5.34 | 22.9 |
| $DyH_3$ | 66 | 3.67 | 6.62 | 23.2 | 7.0 | 5.23 | 21.4 |
| $HoH_3$ | 67 | 3.64 | 6.56 | 22.7 | 7.8 | 5.25 | 21.8 |
| $ErH_3$ | 68 | 3.62 | 6.53 | 22.3 | 9.2 | 5.23 | 21.5 |
| $LuH_3$ | 71 | 3.56 | 6.44 | 21.3 | 12.0 | 5.12 | 20.2 |

* Lattice parameter of cubic trihydrides extrapolated to ambient pressure

The lattice parameters and molar volume of hexagonal and cubic phases of different RE trihydrides are collected in **Table 4.1.** The transition pressures of RE trihydrides as a function of the molar volume of the initial hcp phase at ambient conditions. As shown in **Fig. 4.1** and **Fig. 4.2**, our results of $DyH_3$ are well agreed with the liner fittings of transition pressure against both the molar volume of the initial hcp phase at ambient conditions and the atomic number of the forming RE metals.

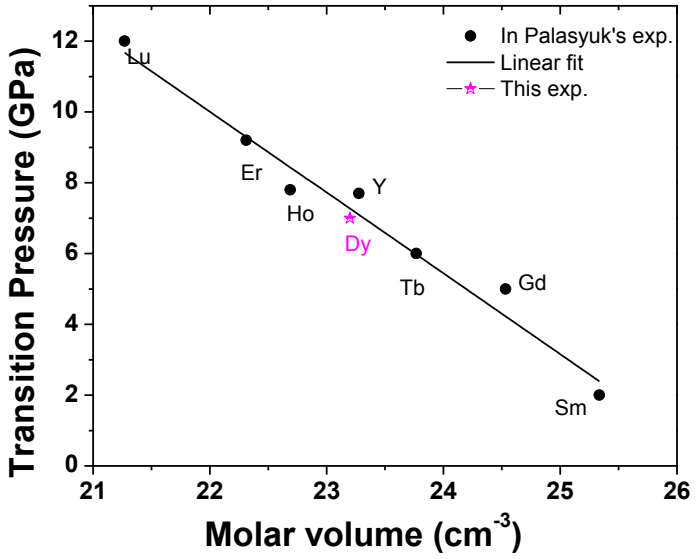


**Fig. 4.1** The transition pressures of RE trihydrides as a function of the molar volume of the initial hcp phase at ambient conditions. The experimental data for other $REH_3$ are cited from Palasyuk's publications[7,8].

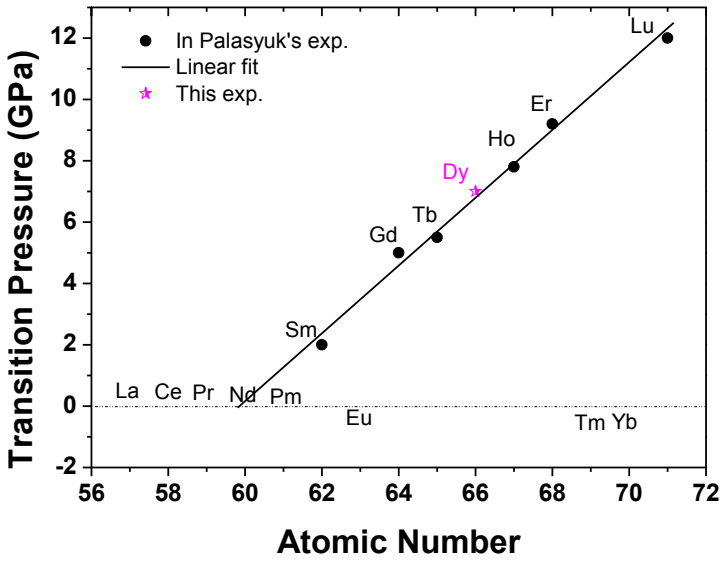


**Fig. 4.2** The transition pressures of RE trihydrides as a function of the atomic number of the forming RE metals. The experimental data for other $REH_3$ are cited from Palasyuk's publications[7,8].

## 4.2 Transition Metal hydrides

To summarize, we have studied the crystal structure and the lattice parameters of molybdenum and tantalum under high hydrogen pressure. For Mo-H system, the composition H/Mo of molybdenum hydride is shown to increase continuously with pressure increase, instead of being constant or undergo discontinuities. At pressure around 4 GPa, a phase transformation was observed of a bcc metal to a hydride with an hcp metal lattice and H/Mo≈1.1. Further hydrogen pressure increase resulted in a continuous increase of the hydrogen content of the hydride. At about 15 GPa the hydrogen content reached saturation, and no further hydrogen absorption occurred up to the maximal reached pressure. The saturation composition H/Mo=1.35(10) was estimated from volumetric considerations. Our results show the importance of high-pressure technique as an instrument for the synthesis of new compounds with unexpected stoichiometries, and, particularly, for new hydrogen-rich materials.

Compared to other d-metals of the IV group (vanadium and niobium), tantalum forms dihydride at a much higher hydrogen pressure and this dihydride has an hcp metal lattice instead of the fcc one. The new tantalum dihydride has an overstoichiometric composition of H/Ta = 2.2(1), as measured by thermodesorption. In contrast to the Nb-H phases[128,113], the atomic volumes of both the orthorhombic monohydrides and hcp dihydride of tantalum well obey the Vegard law.

Luckily, single-phase samples of tantalum dihydride can be recovered to ambient pressure if cooled to the liquid $N_2$ temperature. This allows an accurate investigation of many properties of the dihydride by conventional techniques including the determination of its full crystal structure by neutron diffraction. The work is in progress.

Taking into account of our contribution, the hydrides formed by TMs from group 4 to 10 are renewed and listed in **Fig. 4.3**. The overall pictures of binary hydrides formed by various elements in periodic table are shown in **Fig. 4.4**.

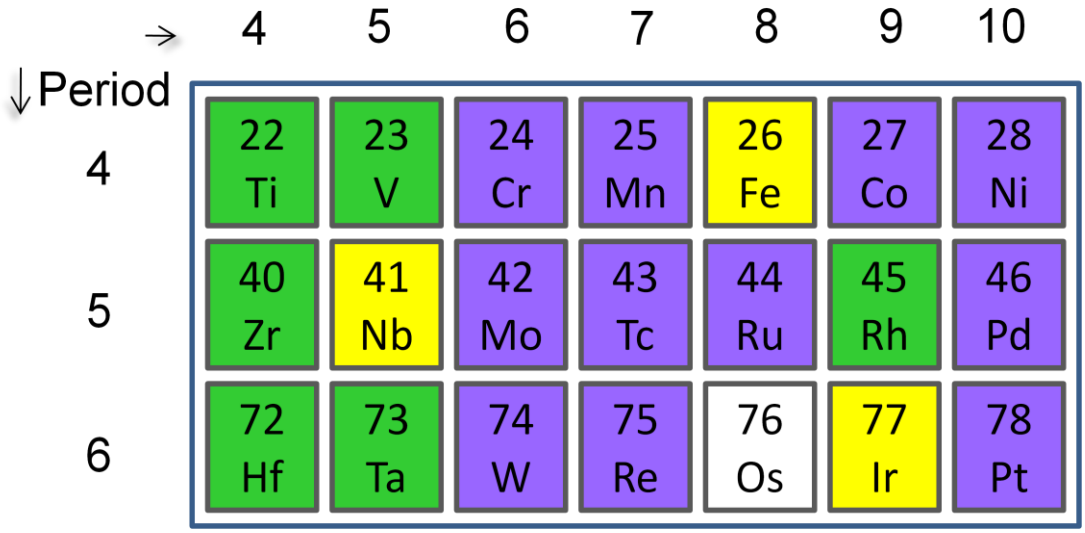


**Fig. 4.3** Binary hydrides formed by TMs from group 4 to 10 in periodic table

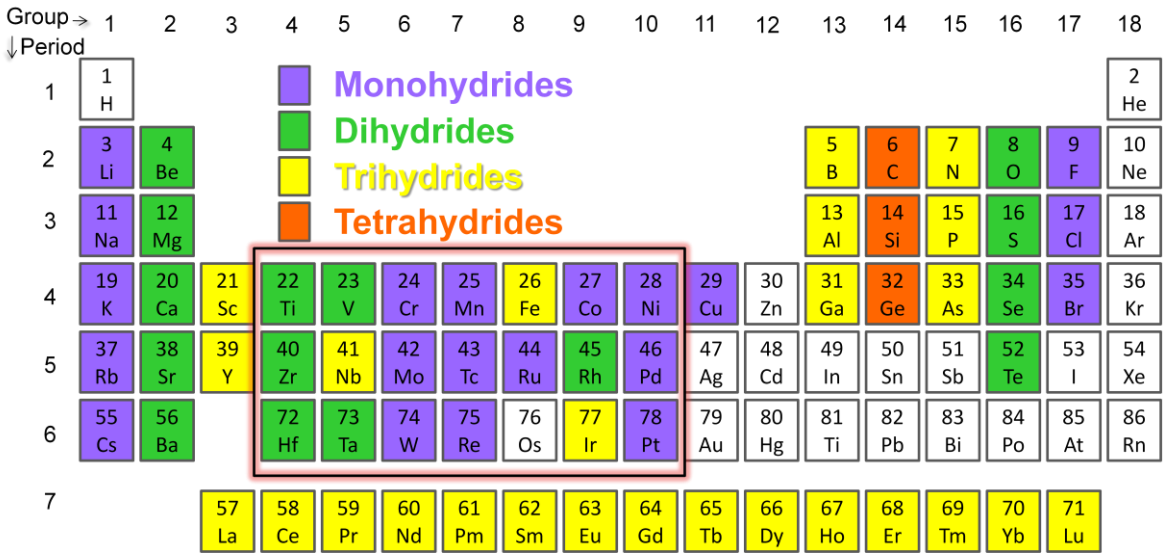


**Fig. 4.4** Binary hydrides formed by various elements in periodic table

# References

(1) Ducastelle, F.; Caudron, R.; Costa, P. *Journal of Physics and Chemistry of Solids* **1970**, *31*, 1247.

(2) Peisl, H. In *Hydrogen in metals I*; Springer: 1978, p 53.

(3) Szafrański, A. W.; Tkacz, M.; Majchrzak, S.; Züchner, H. *Journal of the Less Common Metals* **1984**, *101*, 523.

(4) Staliński, B. *Bull. Acad. Pol. Sci. Cl. 3* **1954**, *2*, 245.

(5) Asano, H.; Ishikawa, Y.; Hirabayashi, M. *Journal of Applied Crystallography* **1978**, *11*, 681.

(6) Yamada, R.; Watanabe, N.; Sato, K.; Asano, H.; Hirabayashi, M. *Journal of the Physical Society of Japan* **1976**, *41*, 85.

(7) Palasyuk, T.; Saxena, S.; Zaleski-Ejgierd, P.; Tkacz, M. *J Alloy Compd* **2014**, *597*, 58.

(8) Palasyuk, T.; Tkacz, M. *Solid State Commun* **2007**, *141*, 354.

(9) Mellor, J. W. *A comprehensive treatise on inorganic and theoretical chemistry*; Longmans, Green, 1922; Vol. 2.

(10) Hautefeuille, P.; Troost, L. *Ann. Chim. Phys* **1874**, *2*, 273.

(11) Johnson, W. C.; Stubbs, M. F.; Sidwell, A. E.; Pechukas, A. *J Am Chem Soc* **1939**, *61*, 318.

(12) Burtovyy, R.; Tkacz, M. *Solid State Commun* **2004**, *131*, 169.

(13) Fukai, Y. *The metal-hydrogen system: basic bulk properties*; Springer Science & Business Media, 2006; Vol. 21.

(14) Drozdov, A.; Eremets, M.; Troyan, I.; Ksenofontov, V.; Shylin, S. *Nature* **2015**, *525*, 73.

(15) Drozdov, A.; Kong, P.; Minkov, V.; Besedin, S.; Kuzovnikov, M.; Mozaffari, S.; Balicas, L.; Balakirev, F.; Graf, D.; Prakapenka, V. *arXiv preprint arXiv:1812.01561* **2018**.

(16) Atkins, P. W.; De Paula, J. *Atkins' Physical chemistry*, 2014.

(17) Murnaghan, F. D. *Proceedings of the National Academy of Sciences* **1944**, *30*, 244.

(18) Birch, F. *Physical Review* **1947**, *71*, 809.

(19) Hazen, R. M. *The diamond makers*; Cambridge University Press, 1999.

(20) Wigner, E.; Huntington, H. á. *The Journal of Chemical Physics* **1935**, *3*, 764.

(21) Bonev, S. A.; Schwegler, E.; Ogitsu, T.; Galli, G. *Nature* **2004**, *431*, 669.

(22) Bridgman, https://www.nobelprize.org/prizes/physics/1946/bridgman/speech/.

(23) Drickamer, H. G. In *Solid State Physics*; Elsevier: 1965; Vol. 17, p 1.

(24) Drickamer, H.; Lynch, R.; Clendenen, R.; Perez-Albueene, E. In *Solid State Physics*; Elsevier: 1967; Vol. 19, p 135.

(25) Jayaraman, A. *Reviews of Modern Physics* **1983**, *55*, 65.

(26) Block, S.; Weir, C.; Piermarini, G. *Science* **1965**, *148*, 947.

(27) Van Valkenburg, A. *LeCreusot, Saone-et-Loire, France* **1965**.

(28) Forman, R. A.; Piermarini, G. J.; Barnett, J. D.; Block, S. *Science* **1972**, *176*, 284.

(29) Barnett, J.; Block, S.; Piermarini, G. *Review of scientific instruments* **1973**, *44*, 1.

(30) Mao, H.; Bell, P.; Shaner, J. t.; Steinberg, D. *J Appl Phys* **1978**, *49*, 3276.

(31) Dewaele, A.; Torrent, M.; Loubeyre, P.; Mezouar, M. *Phys Rev B* **2008**, *78*, 104102.

(32) Akahama, Y.; Kawamura, H. *J Appl Phys* **2006**, *100*, 043516.

(33) Piermarini, G.; Block, S.; Barnett, J. *J Appl Phys* **1973**, *44*, 5377.

(34) Recio, J. M.; Menendez, J. M.; De la Roza, A. O. *An introduction to high-pressure science and technology*; CRC Press, 2016.

(35) Mueller, W. M., James P. Blackledge, George G. Libowitz **1968**, 385.

(36) *Nomenclature of Inorganic Chemistry: IUPAC Recommendations 2005*; Damhus, N. G. C. a. T., Ed.; RSC: Canbridge, 2005.

(37) Daane, A. H.; Rundle, R. E.; Smith, H. G.; Spedding, F. H. *Acta Crystallogr* **1954**, *7*, 532.

(38) Spedding, F. H.; Daane, A. H.; Herrmann, K. W. *Acta Crystallogr* **1956**, *9*, 559.

(39) Beaudry, B. J.; Palmer, P. E. *J Less-Common Met* **1974**, *34*, 225.

(40) Spedding, F. H.; Daane, A. H.; Herrmann, K. W. *T Am I Min Met Eng* **1957**, *209*, 895.

(41) Pallmer, P. G.; Chikalla, T. D. *J Less-Common Met* **1971**, *24*, 233.

(42) Harris, I.; Raynor, G. *SOME OBSERVATIONS ON THE CRYSTAL STRUCTURES OF THE RARE EARTH METALS AND ALLOYS*, Univ. of Birmingham, Eng., 1969.

(43) Gschneidner, K. A.; Eyring, L. *Handbook on the physics and chemistry of rare earths*; North-Holland ;sole distributors for the U.S.A. and Canada, Elsevier North-Holland: New York, NY, USA, 1978; Vol. 1.

(44) Adams, L. H.; Davis, B. L. *P Natl Acad Sci USA* **1962**, *48*, 982.

(45) Winkler, C. *European Journal of Inorganic Chemistry* **1891**, *24*, 873.

(46) Matignon, C. *Compt. Rend.* **1900**, *131*, 891.

(47) Muthmann, W.; Kraft, K. *Justus Liebigs Annalen der Chemie* **1902**, *325*, 261.

(48) I. I. Zhukov *J. Russ. Phys. Chem. Soc.* **1913**, *45*, 2073.

(49) Zhukov, I. I. *Ann. Inst. Anal. Phys. Chem.* **1926**, *3*, 461.

(50) Zhukov, I. I. *Ann. Inst. Anal. Phys. Chem.* **1927**, *3*, 600.

(51) Sieverts, A.; Müller - Goldegg, G. *Zeitschrift für anorganische und allgemeine Chemie* **1923**, *131*, 65.

(52) Sieverts, A.; Roell, E. *Z. Anorg. Allg. Chem* **1925**, *146*, 149.

(53) Sieverts, A.; Gotta, A. *Zeitschrift für anorganische und allgemeine Chemie* **1928**, *172*, 1.

(54) Libowitz, G.; Maeland, A. *Handbook on the physics and chemistry of rare earths* **1979**, *3*, 299.

(55) Guthrie, J. W.; Beavis, L. C.; Begeal, D. R.; Perkins, W. G. *J Nucl Mater* **1974**, *53*, 313.

(56) Curzon, A.; Singh, O. *Journal of Physics D: Applied Physics* **1975**, *8*, 1703.

(57) Libowitz, G. G. *Berich Bunsen Gesell* **1972**, *76*, 837.

(58) Pebler, A.; Wallace, W. E. *J Phys Chem-Us* **1962**, *66*, 148.

(59) Mansmann, M.; Wallace, W. E. *Solid State Commun* **1964**, *2*, 25.

(60) Mueller, W. M., James P. Blackledge, George G. Libowitz **1968**, 389.

(61) Hardcastle, K. I.; Warf, J. C. *Inorg Chem* **1966**, *5*, 1728.

(62) Bashkin, I. O.; Ponyatovskii, E. G.; Kost, M. E. *Phys Status Solidi B* **1978**, *87*, 369.

(63) Goon, E. J. *J Phys Chem-Us* **1959**, *63*, 2018.

(64) Korst, W. L.; Warf, J. C. *Inorg Chem* **1966**, *5*, 1719.

(65) Haschke, J. M.; Clark, M. R. *High Temp Sci* **1975**, *7*, 152.

(66) Sturdy, G. E.; Mulford, R. N. R. *J Am Chem Soc* **1956**, *78*, 1083.

(67) Zogal, O. J. *J Less-Common Met* **1987**, *130*, 187.

(68) Wakamori, K.; Nakamura, T.; Sawaoka, A. *J Mater Sci* **1986**, *21*, 849.

(69) Huiberts, J. N.; Griessen, R.; Rector, J. H.; Wijnaarden, R. J.; Dekker, J. P.; deGroot, D. G.; Koeman, N. J. *Nature* **1996**, *380*, 231.

(70) B.Staliński *Bull. Acad. Pol. Sci. Class III* **1957**, *5*, 1001.

(71) I.O. Bashkin, I. T. B., M.E. Kost, E.G. Ponaytovsky, *Nieorganiczeskije Materialy* **1978**, *14*, 1617.

(72) Armitage, R.; Rubin, M.; Richardson, T.; O'Brien, N.; Chen, Y. *Appl Phys Lett* **1999**, *75*, 1863.

(73) Kerssemakers, J. W. J.; van der Molen, S. J.; Koeman, N. J.; Gunther, R.; Griessen, R. *Nature* **2000**, *406*, 489.

(74) Palasyuk, T.; Tkacz, M. *Solid State Commun* **2004**, *130*, 219.

(75) Palasyuk, T.; Tkacz, M. *Solid State Commun* **2005**, *133*, 481.

(76) Palasyuk, T.; Tkacz, M. *Solid State Commun* **2005**, *133*, 477.

(77) Palasyuk, T.; Tkacz, M.; Vajda, P. *Solid State Commun* **2005**, *135*, 226.

(78) Palasyuk, T.; Tkacz, M. *Solid State Commun* **2007**, *141*, 302.

(79) Palasyuk, T.; Tkacz, M.; Dubrovinsky, L. *Solid State Commun* **2007**, *142*, 337.

(80) Tkacz, M.; Palasyuk, T. *J Alloy Compd* **2007**, *446*, 593.

(81) Kume, T.; Ohura, H.; Sasaki, S.; Shimizu, H.; Ohmura, A.; Machida, A.; Watanuki, T.; Aoki, K.; Takemura, K. *Phys Rev B* **2007**, *76*.

(82) Kume, T.; Ohura, H.; Takeichi, T.; Ohmura, A.; Machida, A.; Watanuki, T.; Aoki, K.; Sasaki, S.; Shimizu, H.; Takemura, K. *Phys Rev B* **2011**, *84*.

(83) Meng, H.; Palasyuk, T.; Drozd, V.; Tkacz, M. *J Alloy Compd* **2017**, *722*, 946.

(84) Mao, H. K.; Xu, J.; Bell, P. M. *J Geophys Res-Solid* **1986**, *91*, 4673.

(85) Hammersley, A. P.; Svensson, S. O.; Hanfland, M.; Fitch, A. N.; Hausermann, D. *High Pressure Res* **1996**, *14*, 235.

(86) Grosshans, W. A.; Holzapfel, W. B. *Phys Rev B* **1992**, *45*, 5171.

(87) Kong, B.; Zhang, L.; Chen, X. R.; Zeng, T. X.; Cai, L. C. *Physica B* **2012**, *407*, 2050.

(88) Udovic, T. J.; Huang, Q.; Lynn, J. W.; Erwin, R. W.; Rush, J. J. *Phys Rev B* **1999**, *59*, 11852.

(89) Boroch, E.; Conder, K.; Ruxiu, C.; Kaldis, E. *J Less-Common Met* **1989**, *156*, 259.

(90) Vorderwisch, P.; Hautecler, S.; Wegener, W. *J Less-Common Met* **1980**, *74*, 117.

(91) Meng, H.; Kuzovnikov, M. A.; Tkacz, M. *Int J Hydrogen Energ* **2017**, *42*, 29344.

(92) Klavins, P.; Shelton, R. N.; Barnes, R. G.; Beaudry, B. J. *Phys Rev B* **1984**, *29*, 5349.

(93) Bayarjargal, L.; Wiehl, L.; Winkler, B. *High Pressure Res* **2013**, *33*, 642.

(94) Palasyuk, T.; Tkacz, M. *J Alloy Compd* **2009**, *468*, 191.

(95) Ito, T.; Beaudry, B.; Gschneidner Jr, K.; Takeshita, T. *Phys Rev B* **1983**, *27*, 2830.

(96) Udovic, T. J.; Huang, Q.; Karmonik, C.; Rush, J. J. *J Alloy Compd* **1999**, *293-295*, 113.

(97) Didisheim, J. J.; Yvon, K.; Fischer, P.; Hälg, W.; Schlapbach, L. *Phys Lett A* **1980**, *78*, 111.

(98) McNaught, A. D. *Compendium of chemical terminology*; Blackwell Science Oxford, 1997; Vol. 1669.

(99) R. H. Petrucci, W. S. H., F.G. Herring *General Chemistry*; 8th ed. ed.; Prentice-Hall, 2002.

(100) Housecroft, C. E.; Sharpe, A. G. *Inorganic chemistry*; 2nd ed.; Pearson Prentice Hall: Upper Saddle River, N.J., 2005.

(101) Pawar, R. R.; Deshpande, V. *Acta Crystallographica Section A: Crystal Physics, Diffraction, Theoretical and General Crystallography* **1968**, *24*, 316.

(102) Jamieson, J. *High Temperatures-High Pressures* **1973**, *5*, 123.

(103) Russell, R. *J Appl Phys* **1953**, *24*, 232.

(104) Vasyutinskiy, B.; Kartmazov, G.; Smirnov, Y. M.; Finkel, V. *PHYS METALS METALLOGR, 1966, 21,--4--, 134-135* **1966**.

(105) Straumanis, M.; Zyszczynski, S. *Journal of Applied Crystallography* **1970**, *3*, 1.

(106) Waseda, Y.; Hirata, K.; Ohtani, M. *High Temperatures-High Pressures* **1975**, *7*, 221.

(107) Ross, R.; Hume-Rothery, W. *Journal of the Less Common Metals* **1963**, *5*, 258.

(108) Gazzara, C. P.; Middleton, R. M.; Weiss, R.; Hall, E. *Acta Crystallogr* **1967**, *22*, 859.

(109) Mooney, R. *Acta Crystallogr* **1948**, *1*, 161.

(110) Liu, L.-G.; Takahashi, T.; Bassett, W. A. *Journal of Physics and Chemistry of Solids* **1970**, *31*, 1345.

(111) Kohlhaas, R.; Dunner, P.; N, S. *Zeitschrift fur Angewandte Physik* **1967**, *23*, 245.

(112) Finkel, V. *Phys. Met. Metallogr.* **1971**, *32*, 231.

(113) Vincent, F.; Figlarz, M. *COMPT REND ACAD SCI* **1967**, *264*, 1270.

(114) Singh, H. *Acta Crystallographica Section A: Crystal Physics, Diffraction, Theoretical and General Crystallography* **1968**, *24*, 469.

(115) Taylor, A. *Journal of the Institute of Metals* **1950**, *77*, 585.

(116) Rao, C. N.; Rao, K. K. *Canadian Journal of Physics* **1964**, *42*, 1336.

(117) Graham, T. *Philosophical transactions of the Royal Society of London* **1866**, *156*, 399.

(118) Tkacz, M.; Litwiniuk, A. *J Alloy Compd* **2002**, *330-332*, 89.

(119) Baranowski, B.; Wisniewski, R. *B Acad Pol Sci-Chim* **1966**, *14*, 273.

(120) Baranowski, B. In *Hydrogen in Metals II*; Springer: 1978, p 157.

(121) Prokhorov, A. M.; Prokhorov, A. *Problems in solid-state physics*; Mir Publishers, 1984.

(122) Scheler, T.; Peng, F.; Guillaume, C. L.; Howie, R. T.; Ma, Y.; Gregoryanz, E. *Phys Rev B* **2013**, *87*, 184117.

(123) Scheler, T.; Degtyareva, O.; Marqués, M.; Guillaume, C. L.; Proctor, J. E.; Evans, S.; Gregoryanz, E. *Phys Rev B* **2011**, *83*, 214106.

(124) Li, B.; Ding, Y.; Kim, D. Y.; Ahuja, R.; Zou, G.; Mao, H.-K. *Proceedings of the National Academy of Sciences* **2011**, *108*, 18618.

(125) Scheler, T.; Marqués, M.; Konôpková, Z.; Guillaume, C. L.; Howie, R. T.; Gregoryanz, E. *Phys Rev Lett* **2013**, *111*, 215503.

(126) Pépin, C. M.; Dewaele, A.; Geneste, G.; Loubeyre, P.; Mezouar, M. *Phys Rev Lett* **2014**, *113*, 265504.

(127) Schober, T.; Wenzl, H. In *Hydrogen in Metals II*; Springer: 1978, p 11.

(128) Liu, G.; Besedin, S.; Irodova, A.; Liu, H.; Gao, G.; Eremets, M.; Wang, X.; Ma, Y. *Phys Rev B* **2017**, *95*, 104110.

(129) Waite, T.; Wallace, W.; Craig, R. *The Journal of Chemical Physics* **1956**, *24*, 634.

(130) Kawamura, H.; Moriwaki, T.; Akahama, Y.; Takemura, K. *Int. Conf. High Press. Sci. Technol.* **2005**, 277.

(131) Kuzovnikov, M.; Tkacz, M. *Phys Rev B* **2016**, *93*, 064103.

(132) Krukowski, M.; Baranowski, B. *Journal of the Less Common Metals* **1976**, *49*, 385.

(133) Kuzovnikov, M.; Tkacz, M. *J Alloy Compd* **2015**, *650*, 884.

(134) Kuzovnikov, M.; Tkacz, M. *Int J Hydrogen Energ* **2017**, *42*, 340.

(135) Kuzovnikov, M.; Meng, H.; Tkacz, M. *J Alloy Compd* **2017**, *694*, 51.

(136) Fukai, Y.; Mizutani, M. *Materials Transactions* **2003**, *44*, 1359.

(137) Abramov, S.; Antonov, V.; Bulychev, B.; Fedotov, V.; Kulakov, V.; Matveev, D.; Sholin, I.; Tkacz, M. *J Alloy Compd* **2016**, *672*, 623.

(138) Feng, X.; Zhang, J.; Liu, H.; Iitaka, T.; Yin, K.; Wang, H. *Solid State Commun* **2016**, *239*, 14.

(139) *Journal of Geophysical Research: Solid Earth* **1986**, *91*, 4673.

(140) Tkacz, M. *Pol J Chem* **1995**, *69*, 1205.

(141) Tkacz, M.; Majchrzak, S.; Baranowski, B. *Zeitschrift für Physikalische Chemie* **1989**, *163*, 467.

(142) Tkacz, M. *Proc. Of Joint XV AIRAPT & XXXIII EHPRG International Conference, Warsaw, Poland* **1995**, 543.

(143) Huang, X.; Li, F.; Zhou, Q.; Meng, Y.; Litasov, K. D.; Wang, X.; Liu, B.; Cui, T. *Sci Rep-Uk* **2016**, *6*, 19923.

(144) Scheler, T.; Degtyareva, O.; Gregoryanz, E. *The Journal of Chemical Physics* **2011**, *135*, 214501.

(145) Bashkin, I.; Antonov, V.; Ponyatovsky, E. **2003**.

(146) SWITENDICK, A. C.; ACS Publications: 1978; Vol. 167, p 264.

(147) Kuzovnikov, M. A.; Tkacz, M.; Meng, H. J.; Kapustin, D. I.; Kulakov, V. I. *Phys Rev B* **2017**, *96*.

(148) Zhuang, Q.; Jin, X.; Cui, T.; Ma, Y.; Lv, Q.; Li, Y.; Zhang, H.; Meng, X.; Bao, K. *Inorg Chem* **2017**, *56*, 3901.

(149) Mao, H. K.; Xu, J.; Bell, P. M. *Journal of Geophysical Research: Solid Earth* **1986**, *91*, 4673.

(150) Atou, T.; Badding, J. V. *J Solid State Chem* **1995**, *118*, 299.

(151) Szafranski, A. W.; Tkacz, M.; Majchrzak, S.; Zuchner, H. *J Less-Common Met* **1984**, *101*, 523.

(152) Antonov, V. E.; Latynin, A. I.; Tkacz, M. *J Phys-Condens Mat* **2004**, *16*, 8387.

(153) Cynn, H.; Yoo, C.-S. *Phys Rev B* **1999**, *59*, 8526.

(154) Slesarev, V. N.; Brazhkin, V. V. *High Pressure Res* **2004**, *24*, 371.

(155) Antonov, V. E.; Bulychev, B. M.; Fedotov, V. K.; Kapustin, D. I.; Kulakov, V. I.; Sholin, I. A. *Int J Hydrogen Energ* **2017**, *42*, 22454.

(156) Bashkin, I. O.; Antonov, V. E.; Bazhenov, A. V.; Bdikin, I. K.; Borisenko, D. N.; Krinichnaya, E. P.; Moravsky, A. P.; Harkunov, A. I.; Shul'ga, Y. M.; Ossipyan, Y. A.; Ponyatovsky, E. G. *Journal of Experimental and Theoretical Physics Letters* **2004**, *79*, 226.

(157) Andreasen, A.; Vegge, T.; Pedersen, A. S. *The Journal of Physical Chemistry B* **2005**, *109*, 3340.

(158) Matsuoka, T.; Fujihisa, H.; Hirao, N.; Ohishi, Y.; Mitsui, T.; Masuda, R.; Seto, M.; Yoda, Y.; Shimizu, K.; Machida, A.; Aoki, K. *Phys Rev Lett* **2011**, *107*, 025501.

(159) Olsen, J. S.; Buras, B.; Gerward, L.; Johansson, B.; Lebech, B.; Skriver, H. L.; Steenstrup, S. *Phys Scripta* **1984**, *29*, 503.

(160) Chen, C. B.; Tian, F. B.; Duan, D. F.; Bao, K.; Jin, X. L.; Liu, B. B.; Cui, T. *J Chem Phys* **2014**, *140*.